

# Improving real-time ship motion predictions by fusing measurements and hydro-dynamical modeling

J.J.C. Bresser

Technische Universiteit Delft





# Improving real-time ship motion predictions by fusing measurements and hydro-dynamical modeling

by

**J.J.C. Bresser**

in partial fulfillment of the requirements for the degree of

**Master of Science**  
in Marine Technology

at the Delft University of Technology,  
to be defended publicly on Tuesday October 16, 2018 at 14:00 AM.

Supervisor: Dr. ir. P. Naaijen, TU Delft

Thesis committee: Prof. dr. ir. A.P. van't Veer TU Delft  
Dr. C. Smith TU Delft

*This thesis is confidential and cannot be made public until October 16, 2024.*

An electronic version of this thesis is available at <http://repository.tudelft.nl/>.



# Abstract

Real-time ship motion predictions contributes to safer operations at sea and increases workability. Nowadays, a handful of people and companies are actively working on this subject. Most approaches use the ship's navigational radar to first predict the wavefield surrounding the vessel and then calculate the motion response. One of the methods used to calculate the ship's motions is a linear ship motion model based on a frequency-domain approach. The downside of this approach is that the accuracy of the motion predictions is affected by (for example) uncertainties in the Response Amplitude Operators. In this thesis, it is shown that estimating transfer-functions from measured motions and a so-called "now-cast" prediction of the forces will counteract for such uncertainties. For the estimation of these transfer-functions, different methods and smoothing techniques are evaluated. Based on sea-trial data, it is shown that the accuracy of the motion predictions increases with  $\sim 1-10\%$  when estimated transfer-functions are used, compared to the solutions obtained by pre-calculated transfer-functions.



# Preface & acknowledgements

I find it truly fascinating that combining a ship its navigational radar, which already exists for almost a hundred years, and a simple desktop computer results in accurate motion predictions up-till 60 seconds ahead. Of course one hundred years ago desktops/computers were unavailable and the motion-theory used in this research dates back to 1960-1980. However, the point which I would like to address here is that not only new state-of-the art techniques will generate stunning results but also the combination of (old) exciting techniques and other fields of expertise. When I started this project, I have never heard of system identification and soon discovered that the possibilities are endless. I am convinced that my research will contribute to an increased accuracy of real-time ship motion predictions and that -better- alternatives will follow.

There are a few people who I would like to thank for their cooperation and support during my Msc Thesis. I would like to start with a special warm thanks to my parents, brothers, girlfriend, and friends, in particular whom always have believed in my knowledge and supported me during my years in college. Second, I would like to thank Peter Naaijen for supervising me through my Msc. Thesis. Third, I would like to thank Jan-Willem van Wingerden for his support and time for questions related to system identification. Fourth, I would like to thank the other members of the committee for taking the time and effort reading and discussing my report. Fifth, I would like to thank those who reviewed my work. And finally, I would like to thank Next Ocean and Damen Shipyards for sharing sea trial data and pictures of the SPA-4207.

*J.J.C. Bresser*  
*Delft, October 2018*



# Contents

<b>Abstract</b>	<b>iii</b>
<b>Preface &amp; acknowledgements</b>	<b>v</b>
<b>Abbreviations</b>	<b>ix</b>
<b>List of symbols</b>	<b>xi</b>
<b>1 Introduction</b>	<b>1</b>
1.1 Main objective & literature review. . . . .	1
1.1.1 Historical background and research objective . . . . .	1
1.1.2 Literature review. . . . .	2
1.2 Sub-objective and research questions. . . . .	4
1.3 Notations & Definitions. . . . .	5
1.3.1 Axis system . . . . .	5
1.3.2 Transfer function estimates . . . . .	6
1.4 Document structure . . . . .	6
<b>2 Ship motions prediction</b>	<b>7</b>
2.1 Wave-field prediction . . . . .	7
2.2 Separation of the directional dependent wave-forces . . . . .	8
2.2.1 Linear Ship motion theory: a brief recap . . . . .	8
2.2.2 Forces and moments as input signals for transfer-function estimations . . . . .	9
2.3 Numerical models . . . . .	11
<b>3 Transfer Function Estimation</b>	<b>19</b>
3.1 Transfer function estimation methods . . . . .	19
3.1.1 Empirical Transfer Function Estimation . . . . .	21
3.1.2 Cross-Spectral method. . . . .	23
3.1.3 Summary estimation methods. . . . .	24
3.2 Spectral density functions, coherence function & variance . . . . .	25
3.3 Window-functions & Welch-averaging . . . . .	26
3.3.1 Window function . . . . .	26
3.3.2 Welch averaging method. . . . .	29
3.4 Transfer function evaluation . . . . .	30
3.4.1 Effect of noise . . . . .	30
3.4.2 Signal & window length . . . . .	33
3.4.3 Window functions . . . . .	35
3.4.4 Summary and discussion . . . . .	35
<b>4 Results</b>	<b>37</b>
4.1 Assessment criteria . . . . .	37
4.2 Synthetic results . . . . .	39
4.3 Sea-trial results . . . . .	46
4.3.1 Now-cast predictions for all runs. . . . .	46
4.3.2 Case studies . . . . .	53
4.3.3 Summary and conclusions sea trial analysis . . . . .	58
4.4 Discussion . . . . .	58
4.4.1 A coupled system . . . . .	58
4.4.2 An alternative method for averaging the ETFE. . . . .	61

---

<b>5</b>	<b>Conclusions and recommendations</b>	<b>63</b>
5.1	Conclusions. . . . .	63
5.2	Recommendations . . . . .	64
	<b>Bibliography</b>	<b>67</b>
<b>A</b>	<b>(Discrete) Fourier Transform</b>	<b>69</b>
<b>B</b>	<b>Synthetization of oceanic waves</b>	<b>71</b>
<b>C</b>	<b>Response Amplitude Operators</b>	<b>75</b>
<b>D</b>	<b>Sea trial results</b>	<b>77</b>

# Abbreviations

$\overline{CSM}$	Averaged Cross Spectrum Method
$\overline{ETFE}$	Averaged Emperical Transfer Function Estimation method
BEM	Boundary Element Method
COG	Center Of Gravity
CSM	Cross Spectrum Method
DFT	Discrete Fourier Transform
DOF	Degree Of Freedom
ETFE	Emperical Transfer Function Estimation method
FA	Fourier Analysis
FFT	Fast Fourier Transform
FRF	Frequency Response Function
IFFT	Inverse Fast Fourier Transform
MISO	Multiple Input Single Output
RAO	Response Amplitude Operator
SISO	Singe Input Single Output
SNR	Signal to Noise Ratio
TF	Transfer Function



# List of symbols

$\hat{\phantom{x}}$	Complex number
$\check{\phantom{x}}$	Estimated function
$*$	Complex conjugate
$*$	Convolution
$ \phantom{x} $	Absolute value
$\angle$	Phase angle
$\Re[\dots]$	Real part of a function
$\beta$	Scaling factor
$\eta$	Surface elevation
$\hat{\eta}_a$	Complex wave amplitude
$\hat{\theta}$	Wave-direction in earth bound axis system
$\gamma^2$	Coherence function
$\bar{\gamma}^2$	Mean coherence over the domain $\Omega_{p98\%}$
$\bar{\epsilon}, \epsilon$	(mean) total error
$\mu, \bar{\mu}$	(mean) wave direction relative to the vessel
$\xi$	Calculated motion
$\xi_a$	Motion amplitude
$\xi_m$	Measured motion
$\rho_\xi$	Cross-correlation coefficient
$\sigma_d$	Ratio of standard deviations of the measured and calculated motions
$\sigma_{\check{G}}$	Estimated standard deviation of TF
$\tau$	Prediction-time constant
$\tau'$	Time constant
$\Phi_{xx}$	Auto-spectral density function of the forces
$\Phi_{yy}$	Auto-spectral density function of the motions or motion response-spectra
$\Phi_{xy}, \Phi_{yx}$	Cross-spectral density function
$\Phi_{vv}$	Auto-spectral density function of noise
$\Psi$	Vessels heading
$\omega$	Wave frequency
$\omega_e$	Encounter Wave frequency
$\Omega_t$	Data set for training the TF's
$\Omega_{p98\%}$	Frequency domain which contains 98% of the energy of the motion response-spectra
$A_\infty$	Added mass at $\omega = \infty$
$A, B, C, I$	Hydro-static added mass, damping, spring-coefficient and mass matrices
$b$	Bias error
$b_{vis}$	Viscous damping
$D$	Directional spreading function

$f_s$	Sampling frequency
$F, F_w$	Wave induced force or moment
$F_{FK}$	Froude Krilov force
$F_d$	Diffraction force
$g_0$	Unit impulse function
$\check{G}$	Estimated force to motion transfer-function
$G_0$	Pre-calculated force to motion transfer-function
$H_0$	Pre-calculated wave to motion transfer-function or RAO
$H'_0$	Pre-calculated wave to force transfer-function
$H_{1/3}$	Significant wave height
$i$	Index notation for DOF
$j$	Imaginary number
$k_x, k_y,$	Wave number
$K$	Retardation function
$l_w$	Window length
$M$	Number of blocks
$N_s$	Number of samples
$N$	Number of resolved wave-components
$N_x, N_y, n_x, n_y$	Noise contributions
$O$	Ship bound origin
$O'$	Spatio-temporal origin
$S_\eta$	Wave-spectrum
$t$	(UTC) time variable
$T_G$	Spectral leakage
$U$	Ship forward velocity
$v$	Noise
$var$	Variance
$w$	Window function
$x, y, z$	Coordinates in earth bound axis system
$x_0, y_0, z_0$	Coordinates in ship bound axis system
$x_0(t), y_0(t)$	Undisturbed signals
$X_0$	Undisturbed frequency domain description of the force
$X$	DFT of the force
$Y$	DFT of the motions
$X_0$	Undisturbed frequency domain description of the motions

# Introduction

In this thesis, it will be shown that accuracy of real-time wave-induced ship motions predictions can be refined with the use of estimated force-to-motion transfer-functions, derived from measured motions and a so called "now-cast" prediction of the forces. The before mentioned forces are calculated by a prediction of the wave-field in combination with wave-to-force transfer-functions, while the motions are measured with a motion sensor. The prediction of the wave-field, and eventually motions and forces, will be explained in more detail in Chapter 2. For the estimation of the transfer-functions different methods can be used which will extensively be discussed in Chapter 3. Eventually in Chapter 4, it will be proven that the use of estimated transfer-functions will increase the accuracy of real-time motion predictions.

Before discussing transfer-function estimation techniques and to prove that these transfer-functions will increase the accuracy of real-time motion predictions, this chapter will give a formal description of the problem and the main objective. Afterwards, a literature review will be held as a general introduction of real-time motion prediction and to highlight some of the difficulties of real-time motion predictions. Based on the main objective and literature review, in Section 1.2 the hypothesis, sub-objectives, and research questions will be given. The remaining sections in this chapter are dedicated to definitions used throughout this document, a description of the structure of this document, and a summary.

## 1.1. Main objective & literature review

### 1.1.1. Historical background and research objective

Real-time prediction of wave-induced ship motions contributes to safer operations and enlarges the weather window at which operations can be performed [13]. Nowadays there are a handful of people and companies [13][1][5] actively working on this subject. The common denominator between of those parties is that they all use the ship its navigational radar to first predict the wave-field and then use that information to calculate the induced ship motions.

One of the used methods to predict wave-induced ship motions is via a frequency-domain approach based on linear ship motion theory [13]. In this approach the ship motions are calculated by superposing the ship its responses to individual wave components, using Response Amplitude Operators (RAO's).

The downside of linear ship motion theory is that (a) it does not include viscous effects like non-linear roll damping [3][1] and (b) the RAO's are depending on the geometric properties, like the mass-moment of inertia, which in practice are uncertain [1][14]. An addition to (a); to incorporate some of the non-linear effects, like non-linear roll damping, linear equivalent terms, obtained from empirical formulas [10], are usually added to the equation of motion from which the RAO's are determined.

However, the uncertainties as described above are related to the forces which results from the motion of the vessel itself, i.e. the inertia- and radiation forces, and not due to the wave-forces acting on the vessel, the Froude-Krylov and diffraction forces. By assuming that the predicted wave-forces can accurately be deter-

mined (See Section 2.2.2 for more details) and the fact that motions can be measured, it might be possible to estimate more accurate transfer-functions (TF's) from measurements, via a Frequency-Analysis (FA), compared to those pre-calculated. These estimated TF's give the relation between the wave-forces and motions, for every Degree-Of-Freedom separately, which after determination can be used for future motion predictions. By estimating TF's from measured data it might resolve (b) and give a better estimation for (a). With the above said the objective of this research will be defined as:

*“The objective of this research is to improve the accuracy of wave induced ship motion prediction by combining a transfer-function estimated from measurements and a linear ship motion model based on a frequency-domain approach”*

This objective has been shared with NextOcean, a company which is specialized in motion predictions, who was willing to cooperate in this project by providing sea-trial data for analysis.

### 1.1.2. Literature review

In this section a small literature review will be held about: different methods to calculate/predict wave-induced ship motions, the main working principles behind real-time wave-field predictions, methods studied in the past to increase the accuracy of motion-predictions, techniques to estimate transfer-functions based on measured data, and the challenges of the aforementioned topics. These topics are discussed in order to give a general introduction into real-time ship motion prediction as well as an introduction to the next section where the sub-objective and research questions will be formulated.

#### Wave-field prediction

As already mentioned in Section 1.1.1, the wave-field is predicted using the ships its navigational radar. Every revolution of the radar provides a 2-D image of the wave-field surrounding the vessel in a 1-5 km range, depending on the kind of radar used[1]. Via a 3-D Fast Fourier Transform (FFT) and a dispersion filter, the complex-wave amplitudes  $\hat{\eta}_{a,n}$ , wave-numbers  $\vec{k}_n$ , and wave-frequencies  $\omega_n$  [12], are extracted. In Section 2.1 this procedure will be discussed in more detail. With the components known, the wave field can be predicted by:

$$\eta(x, y, t, \tau) = \Re \left[ \sum_{n=1}^N \hat{\eta}_{a,n} \cdot e^{-j(\omega_n \cdot (t+\tau) - k_{x,n} \cdot x - k_{y,n} \cdot y)} \right] \quad (1.1)$$

where  $\tau$  is a time-constant which tells how far in the future the wave-field is predicted, i.e.  $\tau = 1$  means 1 second ahead prediction,  $\tau = 30$  means 30 seconds ahead prediction ect. When  $\tau = 0$  the wave-field will be predicted 0 seconds ahead which is commonly referred to as the "nowcast". A typical number of resolve wave-components  $N = 1500$ .

It is not hard to imagine that the quality/ reliability of the predicted wave-field depends on the accuracy at which the components can be obtained. One of the most challenging parts of wave-field prediction is the determination of the correct amplitudes of the wave-height components ( $|\hat{\eta}_{a,n}|$ ) [13][18]. There are several techniques developed to resolve this problem like shadowing techniques or techniques based on the Signal to Noise ratio [4]. In these methods only the radar data is used for the estimation of the wave-heights. In contrast to the methods as mentioned above, another commonly used method is to use the response of the ship to scale the wave-components [13][16][17].

#### Real-time motion prediction models

There are several models developed to predict wave-induced ship motions which in general can be divided into two categories: time-domain models and frequency-domain models. In this section three different models, found in literature, will be presented and discussed.

The first model which can be found [13][5] is a -classical- frequency-domain approach where the ship motions are calculated by superposing the motion response of each individual wave-component using RAO's.

These RAO's are pre-calculated using Boundary Element Method (BEM) software. In other words, the resulting ship motions are calculated by:

$$\xi_i(x, y, t, \tau) = \Re \left[ \sum_{n=1}^N \tilde{\eta}_{a,n} \cdot H_i(\omega_{e,n}, \mu_n, U) \cdot e^{-j(\omega_n \cdot (t+\tau) - k_{x,n} \cdot t - k_{y,n} \cdot y)} \right] \quad (1.2)$$

where the wave components  $\eta_{\hat{a},n}, \vec{k}_n$  and  $\omega_n$  are those obtained from the radar data, as described in the previous section, and  $H(\omega_n, \mu_n, U)$  are the RAO's as mentioned above. The downside of this method is that it does not take -higher order- viscous effects into account and only applies to small slow varying motions. Furthermore, as already mentioned in Section 1.1.1 there are also uncertainties in the RAO's due to loading conditions.

The second model found [1], an adaptive filter method based on a frequency domain approach where the ship is represented as a barge. Since the geometry of a barge can analytically be described, an analytical time-domain description for the Froude-Krilov forces and moments can be made. Then by a power series expansion of these forces, this analytical solution can be rewritten into a combination of three linear time-series. In a frequency-domain representation for the  $i$ -th DOF the equation corresponding to the above is defined as:

$$Y^i(\omega) = H_{yx,1}^i(\omega, U)X_1^i(\omega) + H_{yx,2}^i(\omega, U)X_2^i(\omega) + H_{yx,3}^i(\omega, U)X_3^i(\omega) \quad (1.3)$$

where  $X_1^i(\omega) \dots X_3^i(\omega)$  are the Froude-Krilov forces and moments as mentioned above,  $Y^j(\omega)$  is the frequency-domain description of the measured motions, and  $H_{yx}$  are TF's which need to be determined. The advantage of rewriting the force into three linear-time domain representations is that the additional terms introduced represents higher-order corrections for shorter waves[1]. In order to solve  $H_{yx}$ , the history of the measured motions in combination with the "historical" forces are used. The derivations of the TF's and eventually the prediction of the motions, will be explained in some more detail in the upcoming sub-sections. The downside of this method is that no diffraction forces are included and that the geometry of a barge is not the same as that of a ship.

The third model found in literature [3] is a time-domain model based on Cummins equations. The great advantage of direct modeling in the time-domain is that -higher order- non-linear effects can be taken into account which is impossible in first-order frequency-domain approaches. However, the research outlined in this thesis is restricted to linear frequency-domain models only. Therefore the time-domain approach is out of the scope of the research and will not be further discussed. Nevertheless, if at the end, it is concluded that non-linearities have a significant on the results this time-domain model is a great reference for future studies.

### Transfer function estimation and corrections based on measurements

In the past several attempts have been made to increase the accuracy of real-time motion prediction by deriving or adjusting the RAO's / transfer-functions, based on historical measurements and predictions. The difficulty of deriving RAO's from measurements is that the function  $H_i(\omega_{e,n}, \mu_n, U)$  is depending on the wave-direction[1].

As already discussed in one of the previous section, Alford et al. [1] uses an adaptive filter method to calculate wave induced ship motions by deriving transfer-functions based on historical calculated forces and measured motions. To determine the transfer-functions  $H_{yx}$  they first multiply Equation 1.3 with the complex conjugate to obtain a **system** of cross- and auto spectra:

$$\Phi_{yx}^i(j\omega) = H_{yx}^i(j\omega)\Phi_{xx}^i(j\omega)$$

Then based on **historical** data they calculate the cross and auto-spectra  $\Phi_{yx}$  and  $\Phi_{xx}$  and solve  $H_{yx}$ . When the TF's are determined, in combination with the -in meanwhile- **predicted** values for  $X_1^i(\omega) \dots X_3^i(\omega)$  to obtain  $Y(\omega)$  via Equation 1.3. By transforming the acquired frequency-domain of the predicted motions into the time domain, via an IFFT, motions in the time-domain are obtained. One may notice that this work has similarities to the work presented in this report. Differences are, in this report a higher order expansion is not made for the correction to shorter waves while the work by Alford. et. al. does not include the diffraction forces and represents the ship as an barge. This does **not** mean that one approach is necessarily better than

the other. A future -comparative- study should provide an answer to which approach is preferred.

Another approach -under the assumption that the wave-heights components can accurately be determined-, linear-scaling of the pre-computed RAO's by the difference in the 0th moment of the predicted and measured motions [15]. The difference between this method and proposed solution in this report is that they use a linear scaling factor for the whole RAO, and thus a frequency **independent** solution, while via a spectral analysis no initial RAO is assumed which results in a frequency **dependent** solution.

There is one part in the work mentioned above which, from a personal perspective, describes exactly what the essence of accurate real time-motion prediction is all about and where this research fits in, namely: "The relative difference between the calculated and the measured spectral moments, (...) is an indirect measure of how accurate (or inaccurate...) the onsite sea state is estimated or how well the RAO describes the considered response for the given conditions. In reality, it would be more precise to change the word 'or' with 'and', since it is the combined effect of the estimated sea state and the particular RAO (...)" (Nielsen and Iseki, [15], p.3). Relating this quote to this research, it will be shown that estimating transfer-functions from -unscaled-forces and motions will counteract for both the uncertainties of the wave amplitudes ( $|\hat{h}_{a,n}|$ ) as for the uncertainties in the transfer-functions (as discussed in Section 1.1.1).

### Spectral analysis

As mentioned in Section 1.1.1 the main objective is to estimate a force-to-motion TF from measured motions and predicted forces which will be used to increase the accuracy of real-time motion prediction. For the estimation of the transfer-functions different techniques can be used which will all take as an input  $F_i(t)$  and  $\xi_{i,m}(t)$  as an output signal. Below a brief introduction of the used estimation method will be given

A literature review on spectral analysis showed that there are, in general, numerous options to estimate a TF based on a system with an in- and output[11][21]. Since the area of the estimating transfer-functions from measured ship responses is still quite unexplored, the choice has been made to start with the two most straight forward methods found in literature; the Empirical Transfer Function Estimation method (ETF) and the Cross Spectral Method (CSM)[11][7][21]. In both methods two time-domain signals are first transformed into the frequency-domain, via a Fourier Transformation, and afterwards the TF's are simply obtained due to multiplications and divisions of those spectral results. In these books also methods are described how the outcome of the TF's can be stabilized by for example: Welch-averaging and applying window functions to the time-domain signals. An extensive explanation about the estimation, smoothing techniques, and factors which will affect the outcome of the estimated transfer-function, will be given in Chapter 3.

## 1.2. Sub-objective and research questions

To recall from Section 1.1.1, the main objective of this research is to refine the accuracy of real-time ship motion predictions by inserting estimated transfer-functions into a linear ship motion model based on a frequency-domain approach. In the previous section it was shown that there are several methods which can be used to estimate these transfer-functions. In order to evaluate the different estimation methods and to assess if these estimations result in more accurate predictions, the sub-objective of this research is described as follows:

*"The sub-objective of this research is to develop numerical models to assess if estimated transfer-function will result in more accurate motion predictions by comparing the frequency- and time-domain solutions to those based on pre-calculated transfer-functions"*

As one may notice from the problem description and literature review from the previous section, the problem has become a two-fold. At the one hand, one may want to which estimation method should be used to estimate a transfer-function from measurement. At the other hand, one would like to know if and by how much the accuracy of the motion predictions increases when those estimated transfer-functions are used. Therefore, the first main question will be defined as:

*"Which transfer-function estimation method and smoothing techniques should be used to increase the accuracy of real-time motion prediction?"*

As stated in the previous section, beside the different estimation methods there are also techniques to smoothen the results. Furthermore, there may also be other factors, which not have been initially anticipated, which influences the results. Also, the solution should be obtained within an acceptable time-window for practical usage. Therefore, to answer the first main questions the following sub-questions need to be answered:

- “What are the -dis- advantages of the CSM and ETFE?”
- “How can the results of the estimation methods be smoothened?”
- “Which factors will influence the outcome of the estimation methods?”
- “In which time-window can a reliable estimate of the transfer-function be made?”

For the second part the main question will be defined as:

“How much does the accuracy of real-time ship motion prediction increase when an estimated transfer-function is used in a linear ship motion model, based on a frequency-domain approach, compared to the solutions obtained from pre-calculated transfer-functions?”

To answer this question the following sub-questions have been defined:

- “Which measure(s) should be applied to asses the accuracy of the predicted ship motions?”
- “How accurate can ship motions be predicted when a pre-calculated transfer-functions are used?”
- “How accurate can ship motions be predicted when an estimated transfer-function is used?”
- “Are there other factors which influences the accuracy of real-time motion prediction?”

## 1.3. Notations & Definitions

### 1.3.1. Axis system

For the sake of notation, Figure 1.1 shows the definitions of the axis systems used throughout the document. Table 1.1 shows the definitions related to those axis system. As shown in the figure, an earth- and ship bound axis system is defined. The origin ( $O$ ) in the ship-bound axis system is defined in the Center Of Gravity (COG). The spatio-temporal origin ( $O'$ ) is defined at a certain geographical position on earth which will changes over time. The z-axis in both the ship- as earth bound axis system is pointing towards the reader, i.e. a right-handed coordinate system. Table 1.2 shows the definitions and notations of the different of the 6 (DOF). The axis column as shown in table indicates among which axis, as defined in Figure 1.1, the translation or rotation occurs. A important remark,  $\theta$  and  $\Psi$  are defined counterclockwise with respect to the axis system.

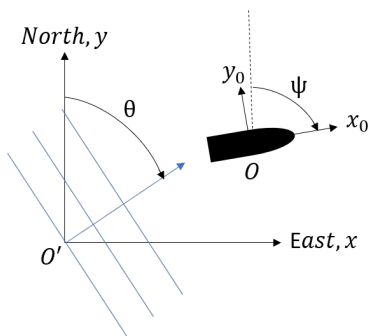


Figure 1.1: Axis system definition

	Notation	Unit
Wave direction	$\theta$	rad
Heading	$\Psi$	rad
Ship fixed coordinates	$x_0, y_0$	m
Earth fixed coordinates	$x, y$	m

Table 1.1: Axis system definition

Table 1.2: Definitions of translations and rotations.

Translations	Axis	Notation	Unit	Rotations	Axis	Notation	Unit
Surge	$x_0$	$\xi_1$	m	Roll	$x_0$	$\xi_4$	rad
Sway	$y_0$	$\xi_2$	m	Pitch	$y_0$	$\xi_5$	rad
Heave	$z_0$	$\xi_3$	m	Yaw	$z_0$	$\xi_6$	rad

### 1.3.2. Transfer function estimates

In Chapter 3 two methods to estimate a TF from measured data will be presented, the Cross-Spectral method (CSM) and the Empirical Transfer Function Estimation ETFE. Also different techniques will be presented to average the results, i.e. the  $\overline{ETFE}$  and  $\overline{CSM}$  methods. By averaging it is meant that the full motion and force record is divided into  $M$  blocks and their intermediate results are averaged. The equations for the different transfer-function estimations are defined as:

$$\begin{aligned}
 ETFE/CSM: \quad \check{G}_i(j\omega) &= \frac{Y_i(j\omega)}{X_i(j\omega)} \\
 \overline{ETFE}: \quad \check{G}_i(i\omega) &= \frac{1}{M} \sum_{m=1}^M \frac{Y_i^m(j\omega)}{X_i^m(j\omega)} \\
 \overline{CSM}_1: \quad \check{G}_i(j\omega) &= \frac{\frac{1}{M} \sum_{m=1}^M Y_i^m(j\omega) X_i^{*m}(j\omega)}{\frac{1}{M} \sum_{m=1}^M X_i^m(j\omega) X_i^{*m}(j\omega)} \\
 \overline{CSM}_2: \quad \check{G}_i(j\omega) &= \frac{\frac{1}{M} \sum_{m=1}^M Y_i^m(j\omega) Y_i^{*m}(j\omega)}{\frac{1}{M} \sum_{m=1}^M X_i^m(j\omega) Y_i^{*m}(j\omega)}
 \end{aligned} \tag{1.4}$$

where  $i$  denotes the DOF observed,  $Y_i(j\omega)$  is the Fourier Transform of the motion signal ( $\xi_i(t)$ ),  $X_i(j\omega)$  the Fourier Transform of the force signal ( $F_i(t)$ ), and  $*$  denotes that the complex conjugate is taken. An extensive discussion about these estimation methods is given in Section 3.1.

## 1.4. Document structure

The document has been well organized following the so called IMRAD structure, i.e.: Introduction, Methodology, Results, and Discussion. This and the previous sections were part of the introduction, Chapter 1. The content of the other chapters will be briefly discussed below.

The methodology part of this research has been spread out over two chapters, Chapter 2 and 3. In Chapter 2 the numerical models which have been developed to estimate the TF and predict ship motions are discussed. In more detail, some topics which will be presented are: how wave-components can be obtained through radar data, what the governing equations are to calculate the wave-induced ship motions, explanation of the prediction time parameter  $\tau$ , and what the difference is between reconstructing and predicting ship motions.

In Chapter 3 different techniques are presented how to estimate the TF's from measured motion and force records. The estimation methods discussed are the -averaged- Empirical Transfer Function Estimation method ( $\overline{ETFE}$ ) and the averaged Cross-Spectral Method ( $\overline{CSM}_1, \overline{CSM}_2$ ). Also different techniques are shown on how to smoothen the estimations via window-functions and Welch-averaging.

In Chapter 4, synthetic and sea trial data will be used to derive a transfer-function to reconstruct and predict wave induced ship motions, obtained from the numerical model described in Chapter 2.3 and the transfer-function estimation techniques as given in Chapter 3. The results are analyzed via defined assessment criteria defined in section 4.1. And finally, in Chapter 5 the conclusions and recommendations will be given.

# 2

## Ship motions prediction

To predict wave-induced ship motions there are basically two main components required. A prediction of the wave-field and a method on how the ship response to those waves. In this section a thorough explanation will be given how the information from a ship its navigational radar can be used to obtain wave components and how these can be used to calculate the wave-induced ship motions, based on linear ship motion theory. In this chapter also an explanation about the developed models will be given and the argumentation why the wave-induced forces can be used as an input for the estimation of transfer-functions. The described models are used in Chapter 3 and 4 to estimate transfer functions and predict the ship motions, driven by synthetically generated data and sea trial results.

### 2.1. Wave-field prediction

As already mentioned in Section 1.1.1 the wave components can be predicted with the use of the ship its (coherent) navigational radar. For the explanation on how wave components can be subtracted from radar data the explanation as given by Naaijen et. al.[14][13] will be followed.

On every revolution of the radar a 2-D image is obtained from the back-scatter of the radar,  $\sigma_r(x, y, t)$ , which is illustrated in Figure 2.1 (left). From this data than a 3-D spectrum can be obtained as function of the wave number,  $S_{\sigma_r}(\vec{k}, \omega_r)$ , using a 3-D Fast Fourier Transform (FFT). To gain confidence of the spectrum obtained the solutions of multiple radar revolutions/images, typically between 5-10, are averaged [13]. Then a so called dispersion filter is used to only keep the wave components which are related to the ocean waves which results in a 2-D spectrum  $S_{\sigma_r}(\vec{k})$ . By assuming that the back-scatter is related to tilt, the following relation should hold:

$$\delta\sigma_r(x, y) = \beta_i \partial_r \eta(x, y) \quad (2.1)$$

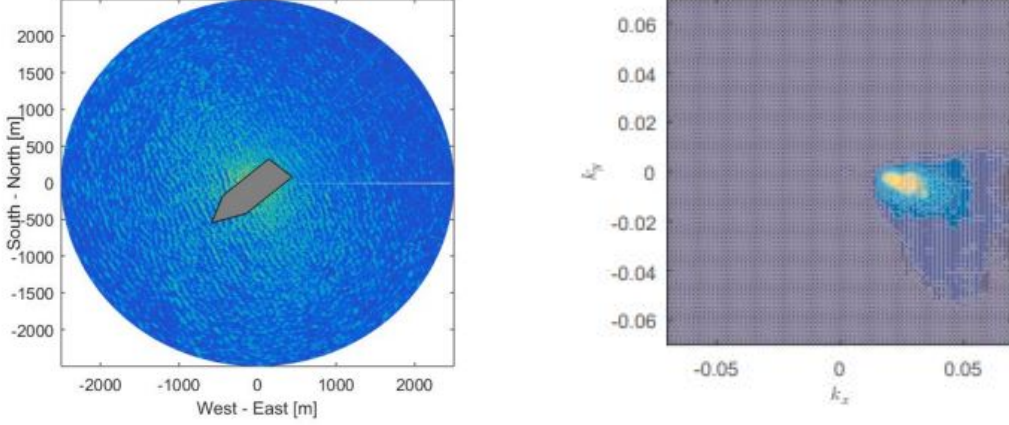
where  $\beta_i$  is a scaling factor, which will be discussed below, and  $\eta(x, y)$  is defined as:

$$\eta(x, y) = \Re \left[ \hat{\eta}_a(\vec{k}_n) e^{i(\vec{k}_n \cdot \vec{x})} \right] \quad (2.2)$$

from which the complex amplitudes  $\hat{\eta}_a(\vec{k}_n)$  are solved by a least square fitting method. An example of the wave-components obtained from the described above is illustrated in Figure 2.1 (right). The scaling parameter  $\beta_i$  is required since the "image" obtained from the radar is 2-D. This thus means that the exact wave-heights are unknown. To linearly-scale the wave components the ratio between the standard deviation of the calculated unscaled motions and measured motions are used, for every DOF separately. In mathematical notations this thus yields:

$$\beta_i = \sqrt{\frac{\sigma_{\xi_i}^2}{\sigma_{\xi_{i,m}}^2}}. \quad (2.3)$$

The estimation of the true amplitudes of the waves is in general a challenging task, as already mentioned in Section 1.1.2, and can be accomplished in several ways [13][18][4][15]. However, in this research it is assumed that this scaling is naturally adopted when a TF is estimated from unscaled force records and absolute measured motions thus  $\beta_i$  will not be adopted into the model when forces are calculated.



(a) Example of raw back scatter  $\sigma_r(x, y)$  image

(b) Example of wave-amplitudes  $|\hat{\eta}_a(\vec{k}_n)|$  as function of  $|k_x|$  and  $|k_y|$

Figure 2.1: Raw scatter data obtained from radar (left) and the phase resolved wave field components (right)[14][13]

## 2.2. Separation of the directional dependent wave-forces

The main goal of this section is to show that wave induced forces and moments can be used as an input signals for the estimation of transfer-functions, which will be discussed in Chapter 3. Before this argumentation will be given first, a brief recap of linear ship motion theory will be held be used for the argumentation of this statement as well as an introduction to the next section.

### 2.2.1. Linear Ship motion theory: a brief recap

It is well known and accepted that under mild conditions, i.e. small displacements and angles, wave induced ship motions can be calculated by linear ship motion theory[9]. In this theory the resulting ship motions are calculated by the summation of the steady-state responses of the ship to each individual wave, also known as the super-position principle. The steady state response, to a single wave, of the motions ( $\xi_i(t)$ ) is the result of the following mass-spring system:

$$\vec{F}_{FK}(t, \omega, \mu) + \vec{F}_d(t, \omega, \mu) = (I + A(\omega, U))\ddot{\vec{\xi}}(t) + B(\omega, U)\dot{\vec{\xi}}(t) + \vec{\xi}(t) \quad (2.4)$$

where:  $A(\omega, U)$  and  $B(\omega, U)$  are the frequency dependent added mass and damping coefficients matrices,  $I$  is the inertia/ mass matrix, and the matrix  $C$  contains information of the spring coefficients. Furthermore,  $F_{i,FK}(t, \omega, \mu)$  and  $F_{i,d}(t, \omega, \mu)$  are the Froude-Krilov and respectively diffraction forces, which together form the wave-induced forces, i.e.  $\vec{F}_w(t, \omega, \mu) = \vec{F}_{FK}(t, \omega, \mu) + \vec{F}_d(t, \omega, \mu)$ . The time-domain steady state solution of the wave-forces of a single frequency can be defined as:

$$F_{i,w}(t, \omega, \mu) = \Re \left[ F_{a,i}(\omega, \mu) e^{-j(\omega t + \epsilon_{\eta, F_i})} \right] \quad (2.5)$$

and for the motion yields:

$$\xi_i(\omega, \mu, U) = \Re \left[ \xi_{a,i}(\omega, \mu, U) e^{-j(\omega t + \epsilon_{\eta, \xi})} \right] \quad (2.6)$$

Substituting the two expressions as given above into equation 2.4 yields:

$$\Re \left[ F_{a,i}(\omega, \mu) e^{-j(\omega t + \epsilon_{\eta, F_i})} \right] = \Re \left[ (-\omega^2 (I + A(\omega, U)) - \omega B(\omega, U) + C) \xi_{a,i}(\omega, \mu, U) e^{-j(\omega t + \epsilon_{\eta, \xi})} \right] \quad (2.7)$$

In order to find  $\xi_{a,i}$  and  $\epsilon_{\eta,\xi}$  requires  $F_{a,i}(\omega)$ ,  $\epsilon_{\eta,F_i}$ ,  $A(\omega)$ ,  $B(\omega)$ ,  $I$ , and  $C$ , to be defined. Since it is assumed that the reader of this report is somewhat familiar with -linear- ship motion dynamics, the determination of the static matrices, that is:  $I$  and  $C$ , will not be discussed and only a brief recap of the determination of the fluid related coefficients will given below to highlight the important aspects in this and the following sections.

For the determination of the fluid-related -normalized- coefficients, that is:  $F_{a,i}(\omega)$ ,  $\epsilon_{\eta,F_i}$ ,  $A(\omega, U)$ , and  $B(\omega, U)$ , usually Boundary Element Method software (BEM), based on potential theory, is used. By normalization is meant that the obtained coefficients are divided by the, usually small, wave-height or displacement they have been calculated with. This can be rectified by the fact that linear theory is used which means that if (for example) the wave forces are calculated with a wave-height of  $\eta_a = 1$  [m] that the wave-forces at (for example)  $\eta_a = 2$  [m] can be found by multiplying the normalized coefficient with 2. In other words, for a single wave of height  $\eta_a$  and a certain  $\omega$  the a time-domain description of the force is defined as:

$$F_{i,w}(t, \omega, \mu) = \Re \left[ \eta_a \frac{F_{a,i}(\omega, \mu)}{\eta_1} e^{-j(\omega t + \epsilon_{\eta,F_i})} \right] = \Re \left[ \eta_a H'_{0,i}(j\omega, \mu) e^{-j(\omega t)} \right] \quad (2.8)$$

where the  $j\omega$  notation has been adopted as a reminder that the transfer-function  $H'_{0,i}(j\omega, \mu)$  is complex. The additional 0 in the subscript of the TF has been chosen as a reminder that these are pre-calculated. Similar argumentation about normalizing the coefficients also holds for the other fluid related coefficients ( $A(\omega, U)$  and  $B(\omega, U)$ ), which are related to the fluid motion due to the **motion** of the vessel itself, and thus not the wave height as for the wave forces. As a final remark, the coefficients as defined above are usually calculated at the Center Of Gravity (COG). If eventually a displacement or rotation at another point is required transformation matrices are used.

By solving Equation 2.7, with the normalized coefficients as described above, will eventually result in:

$$\xi_i(t, \omega, \mu, U) = \Re \left[ \eta_a \frac{\xi_{a,i}(\omega, \mu, U)}{\eta_1} e^{-j(\omega t + \epsilon_{\eta,\xi})} \right] = \Re \left[ \eta_a H_{0,i}(j\omega, \mu, U) e^{-j(\omega t)} \right] \quad (2.9)$$

With the motions and forces for one single wave defined it follows that the resulting motions, for the  $i$ th DOF, can be found by the summation of  $N$  wave-components. By taking also into account: vessel speed, the distance between the vessel and spatio-temporal origin, wave numbers, and the random phase angle of the wave-component, that this results in:

$$\xi_i(x, y, t) = \Re \left[ \sum_{n=1}^N \hat{\eta}_{a,n} \cdot H_{0,i}(j\omega_{e,n}, \mu_n, U) \cdot e^{-j(\omega_n \cdot t - k_{x,n} \cdot x - k_{y,n} \cdot y)} \right] \quad (2.10)$$

where  $H_{0,i}(j\omega_n, \mu_n, U)$  are the wave-to motion transfer-functions, also as Response Amplitude Operators (RAO's). The frequency of encounter ( $\omega_{e,n}$ ) as shown in the equations above can be calculated by:

$$\omega_e = \omega - |\vec{k}|U \cos(\mu) \quad (2.11)$$

For the force a similar expression can be found, namely:

$$F_{i,w}(x, y, t) = \Re \left[ \sum_{n=1}^N \eta_{a,n} \cdot H'_{0,i}(\omega_{e,n}, \mu_n) \cdot e^{-j(j\omega_n \cdot (t) - k_{x,n} \cdot x - k_{y,n} \cdot y - \epsilon_n)} \right] \quad (2.12)$$

where  $H'_{0,i}(j\omega_n, \mu_n)$  are the wave-to-force transfer functions.

### 2.2.2. Forces and moments as input signals for transfer-function estimations

In this report it is assumed that the calculated wave-forces ( $F_w = F_{FK} + F_d$ ), which will be shorthanded as  $F$  in further notations, can be taken as an input for the different estimation techniques of the TF, which will be discussed in Chapter 3. The argumentation why this is a reasonable assumption will be discussed in the upcoming paragraphs.

As stated by -for example- Alford et. al [1] solving the inverse problem, to find the RAO's as given in Equation 2.10 from measurements, can be a quite challenging task due to the directional dependent transfer function  $H_{0,i}(j\omega, \mu, U)$ . However, from Equation 2.4 it can be seen that the directional dependency is "added"

to the transfer-functions by the wave forces  $F(\omega_n, \mu_n, U)$  and not by: mass- and inertia forces ( $I$ ), forces due to fluid-motions induced by the ship its motions ( $A(\omega, U), B(\omega, U)$ ), and spring forces ( $C$ ). In other words, applying the same excitation force ( $F_{w,i}(t)$ ) from two different directions results in the same motion response, when the coupling terms are neglected. As a result, when the main-diagonal of the matrices  $I, A, B$ , and  $C$ , are used for calculating the transfer-function  $H_{0,i}(j\omega_n, \mu_n, U)$  the operation:

$$G_i(j\omega_n, \mu_n, U) = \frac{H_{0,i}(j\omega_n, \mu_n, U)}{H'_{0,i}(j\omega_n, \mu_n, U)} \quad (2.13)$$

results in a polar-symmetric force-to-motion transfer-function, for a constant  $U$ . What is meant with polar-symmetry is illustrated in Figure 2.2 in the form of a contour plot and two similar cross sections.

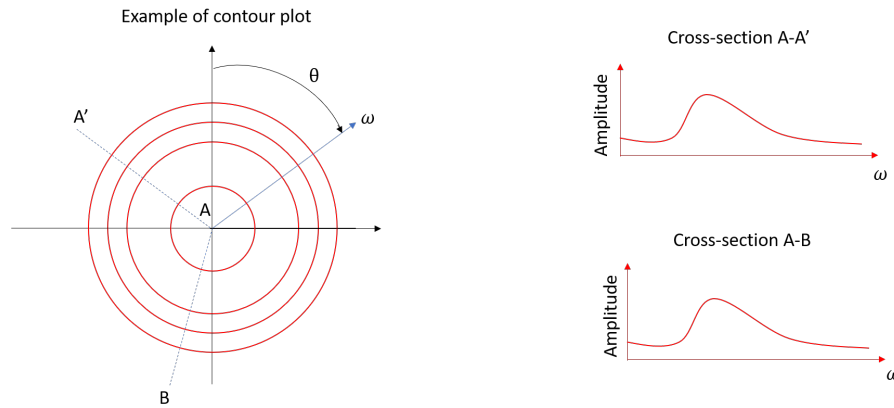


Figure 2.2: Polar symmetry in case of zero velocity

Since the solution for  $G_i$  is the same in every direction,  $\mu_n$  can be eliminated from Equation 2.13 and the 3-D problem becomes a 2-D problem (for a constant  $U$ ). By rewriting Equation 2.10 to an equivalent form defined as:

$$\xi_i(x, y, t) = \Re \left[ \sum_{n=1}^N \hat{\eta}_{a,n} \cdot H'_{0,i}(j\omega_{e,n}, \mu_n) \cdot G_i(j\omega_{e,n}) e^{-j(\omega_n \cdot t - k_{x,n} \cdot x - k_{y,n} \cdot y)} \right] \quad (2.14)$$

results in a description for the total/resulting ship motions which contains a part which is and part which is **not** directional dependent. In more detail, the  $H'_i(j\omega_{e,n}, \mu_n)$  is the directional depending wave-to-force TF while  $G_i(j\omega_{e,n})$  is the directional independent force-to-motion TF. By taking the force in the  $i$ -th direction ( $F_i(t)$ ) as an input and the motions in the  $i$ -th direction ( $\xi_{i,m}(t)$ ) as an output, in the next chapter different method will be discussed on how the transfer-function  $G_i(j\omega_{e,n})$  can be estimated.

Elaborating on the coupling terms, also for the coupling terms (non-diagonal terms) holds that the directional dependency is added by the wave forces (see Equation 2.4). This means that also for each non-diagonal term the solution of Equation 2.13 is polar-symmetric. When (for example) the coupling between heave and pitch is made, for heave Equation 2.14 can be extended to:

$$\begin{aligned} \xi_3(x, y, t) = \Re & \left[ \sum_{n=1}^N \hat{\eta}_{a,n} H'_{0,3}(j\omega_{e,n}, \mu_n) G_{33,i}(j\omega_{e,n}) e^{-j(\omega_n \cdot (t+\tau) + k_{x,n}x + k_{y,n}y)} \right] \\ & + \Re \left[ \sum_{n=1}^N \hat{\eta}_{a,n} H'_{0,5}(j\omega_{e,n}, \mu_n) G_{35,i}(j\omega_{e,n}) e^{-j(\omega_n \cdot (t+\tau) + k_{x,n}x + k_{y,n}y)} \right] \end{aligned} \quad (2.15)$$

where  $G_{33,i}(j\omega_{e,n})$  relates the heave force to the heave motion and  $G_{35,i}(j\omega_{e,n})$  relates the pitch moment to the heave motion. As a consequence of extending the equation, there is now one equation with two unknowns which cannot be solved straight away. However, the contributions of the coupling terms to the total/resulting motions are in general small compared to those from induced by the main excitation force. There-

fore, in this research the coupled effects are initially neglected<sup>1</sup>.

## 2.3. Numerical models

In this section the numerical models to estimate the transfer-functions and to predict the ship its motions will be discussed. The main idea behind the model is that for every DOF separately the -historical- measured motions ( $\xi_{m,i}$ ) and calculated forces ( $F_i$ ) will be used to estimate/train the TF's. Then, those estimated TF's will be used to predict the ship its motions in the future.

Although the main idea behind the model and the corresponding governing equations are rather simple, due to the large amount of -in time changing- variables the model has become quite complex. Therefore, before discussing the models themselves the following topics will be discussed:

- Governing equations
- Time-variables
- Spatio-temporal origin
- Influence of heading and velocity
- Training data
- The numerical models

### Governing equations

In the model three governing equations can be found: one to calculate the forces ( $F_i(x, y, t, \tau)$ ), one to calculate the motions ( $\xi_i(x, y, t, \tau)$ ) based on estimated transfer-functions ( $\check{G}_i(j\omega)$ ), and one to calculate the motions ( $\xi_i(x, y, t, \tau)$ ) based on pre-calculated transfer-functions functions ( $H_{0,i}(j\omega)$ ). The difference to the force- and motion equations as shown in the previous section (Equation 2.10, 2.12 and 2.14) is that an additional time parameter is included  $\tau$ . This parameter will be discussed in more detail in one of the following sub-sections.

The motion predictions based on the pre-calculated TF's (the current situation) are for the  $i$ -th DOF calculated by:

$$\xi_i(x, y, t, \tau) = \Re \left[ \sum_{n=1}^N \beta_i \hat{\eta}_{a,n} H_{0,i}(j\omega_{e,n}, \mu_n) e^{-j(\omega_n \cdot (t+\tau) + k_{x,n}x + k_{y,n}y)} \right]. \quad (2.16)$$

The motion prediction based on estimated TF's (the proposed solution) are for the  $i$ -th DOF calculated by:

$$\xi_i(x, y, t, \tau) = \Re \left[ \sum_{n=1}^N \hat{\eta}_{a,n} H'_{0,i}(j\omega_{e,n}, \mu_n) \check{G}_i(j\omega_{e,n}) e^{-j(\omega_n \cdot (t+\tau) + k_{x,n}x + k_{y,n}y)} \right] \quad (2.17)$$

And the wave-force predictions for the  $i$ -th DOF are calculated by:

$$F_i(x, y, t, \tau) = \Re \left[ \sum_{n=1}^N \hat{\eta}_{a,n} H'_{0,i}(j\omega_{e,n}, \mu_n) e^{-j(\omega_n \cdot (t+\tau) + k_{x,n}x + k_{y,n}y)} \right] \quad (2.18)$$

In which:

$\beta_i$	=	Scaling factor for the wave-height components	
$F_i(x, y, t, \tau)$	=	-Predicted- wave forces for DOF i	
$\xi_i(x, y, t, \tau)$	=	-Predicted- motions for DOF i	
$k_{x,n}, k_{y,n}$	=	Wave number components	(2.19)
$x, y$	=	Distance to spacial-temporal origin	
$\hat{\eta}_{a,n}$	=	complex wave-height component	

<sup>1</sup>In the final stage of this research, a small additional study has been performed where the coupling between heave and pitch was made. In Section 4.4 this method and the results will be shown. The coupling of the other DOF's will be left for future studies.

$\omega_n$	=	Wave-frequency component	
$\mu_n$	=	Wave direction relative to the vessel	
$H'_{0,i}(j\omega_{e,n}, \mu_n)$	=	Pre-calculated wave-to-force TF	
$H_{0,i}(j\omega_{e,n}, \mu_n)$	=	Pre-calculated wave-to-motion TF	
$\check{G}_i(j\omega_{e,n})$	=	Estimated force-to-motion TF	(2.20)
$U$	=	vessel velocity	
$t$	=	Time	
$\tau$	=	Prediction time	

The  $j\omega$  notation in the transfer-functions has been chosen as a reminder to the fact that these are complex variables.

### Time-variables

One may notice that there are two time-variables involved in these equations,  $t$  which is a time variable with respect to the spatio-temporal origin and  $\tau$  the prediction time. By keeping  $\tau$  fixed, at for example  $\tau = 30$ , and evolving over  $t$  will result in constant prediction of the motions 30 seconds ahead. There is one specific case which should be mentioned called a **now-cast** prediction, in this case  $\tau = 0$  while evolving over  $t$ . In other words the motions are real-time predicted 0 seconds ahead.

One of the difficulties of the additional time parameter  $\tau$  is that parts of the Equations 2.16 till 2.18 are depending on parameters which are basically unknown in the future, like the velocity  $U$  and the heading  $\Psi$ , and therefore need to be estimated as well. However, when a vessel is sailing at a constant speed in a certain direction it is safe to assume that these parameters can be predicted with decent accuracy and are therefore considered to be known in the models. More specifically, since the motion predictions will be re-simulated from sea-trial data, and thus the exact positions are known, "future" information is used to determine the heading, position and velocity.

### Spatio-temporal origin

As mentioned in Section 1.1.2 and 2.1, the wave-field is predicted with a spatio-temporal origin. In other words, the origin at which the wave-field is predicted changes over time, due to movement of the vessel and thus also the positions at which the radar images are obtained. This origin corresponds to a certain geological position on earth expressed in latitude and longitude, like for example: 52.0171774, 4.3595728 (in decimal degrees).

Since the wave-field predictions are updated every 6 [s], the distance from the ship its COG to the spatio-temporal origin also changes over time. The above is illustrated in Figure 2.3 where  $O'_1 \dots O'_3$  denotes the different spatio-temporal origins and  $t_1 \dots t_6$  the position of the vessel as function of time. Relating the above to the force and motion equation as shown in the Equations 2.16 till 2.18, at every point in -future- time the position  $x$  and  $y$  needs to be defined. As previously stated, it is assumed that under a constant heading and speed the future positions can accurately be calculated and therefore will be adopted into the model as known parameters.

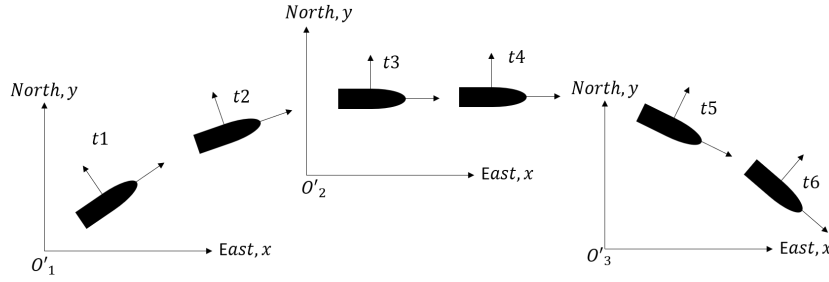


Figure 2.3: Change of spatio-temporal origin and movement of the vessel

## Heading and velocity

As shown in the Equations 2.16 till 2.18, the transfer-function  $H'_0(j\omega_{e,n}, \mu_n)$  is depending on the wave direction, relative to the vessel, and the velocity ( $\omega_{e,n}$ ). By the definition of the heading of the vessel as  $\Psi$  and the wave direction in the earth fixed axis system as  $\theta$  as illustrated in Figure 1.1 the wave-direction relative to the vessel can be calculated by:

$$\mu_n = \Psi(t + \tau) - \theta_n \quad (2.21)$$

This variable needs to be calculated as well, for every future time step.

For the vessel velocity  $U$ , as shown in Equation 2.11 the frequency of encounter is a speed- and directional dependent variable which makes  $H_0(j\omega_{e,n})$ ,  $H'_0(j\omega_{e,n}, \mu_n)$ , and  $\check{G}_i(j\omega_{e,n})$  a speed dependent variables as well. The speed is, again, a -future- time dependent variable which has been adopted into the model as a known variable.

## Training, predicting and reconstructing

When ship motions are predicted during operations by the method proposed in this report, the transfer-functions can only be estimated/ trained from data which lies in the past. This may sound quite arbitrary but, in Chapter 4 sea-trail data will be used for re-simulating motion predictions. This thus means that also data which lies in the -re-simulated- future is available what can be used for training the TF as well. Figure 2.4 illustrates this difference where  $\Omega_T$  denotes the set of data which **available** for training the TF and  $\Omega_t$  represents the data which is **used** for training, i.e.  $\Omega_t \subseteq \Omega_T$ . The data which is contained within  $\Omega_T$  are the recorded motions ( $\xi_{i,m}(t)$ ) and a now-cast prediction of the forces ( $F_i(t)$ ).

The reason why the future data is used is because some of the data records from the Sea-trials are relatively short. After the estimation of the TF there would thus not be a sufficient amount of data left to make a qualitative assessment if the accuracy of the motion predictions increases. The justification that this can be done is because the transfer-function is time independent function which should not change over a -short-time interval.

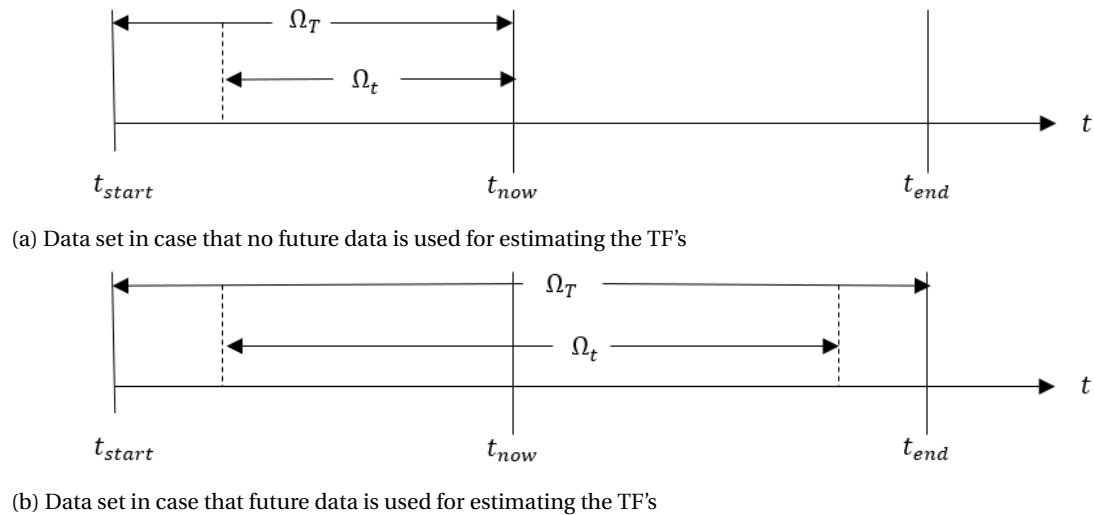


Figure 2.4: Difference in the use of the available data for training the TF's

### Numerical models

Two numerical models have been made, in Matlab2018a, to determine if the use of estimated transfer-functions will result in a more accurate motion predictions. The main difference between the models, one model uses data from obtained from sea-trials measurements while the other model uses synthetically generated data. A flowchart of both models is illustrated in Figure 2.5 and 2.6. As shown in the figures, both models contain the same four blocks. In the first block, the green block, the transfer functions are estimated ( $\check{G}_i(j\omega)$ ). In the second block, the blue block, the motions are predicted based on those estimated transfer-functions. In the yellow block, the motions are predicted based on the pre-calculated transfer-functions  $H_{0,i}(j\omega)$ . In the last block, the predicted motions are compared. Furthermore, in both models the same pre-calculated TF's ( $H_{0,i}$  and  $H'_{0,i}$ ) are used. These transfer-functions correspond to a SPA-4207, a navy patrol vessel build by Damen Shipyards, and are illustrated in Appendix C.

#### Sea-trial data driven model

Figure 2.5 shows the flow-chart of the numerical model, based on sea trial data. As shown in the chart, there are several components required to estimate the transfer-functions (in the green block) and to predict the motions (in the yellow and blue block). The transfer-functions  $H_{0,i}(j\omega)$  and  $H'_{0,i}(j\omega)$  are obtained by BEM software, as already mentioned above. The other variables will be discussed below.

For the wave-components, every 6 seconds a file is received from the radar data analysis that contains the wave-components:  $\omega_n, \vec{k}_n$  and  $\hat{\eta}_n$ , which are related to a certain geographical origin ( $O'$ ). As shown in the chart, the amplitudes ( $\hat{\eta}_n$ ) and wave-numbers ( $\vec{k}_n$ ) are directly inserted into the (corresponding) equations. For the wave-frequency ( $\omega_{e,n}$ ) and wave directions ( $\mu_n$ ), an additional step is required since these variables are depending on the heading ( $\Psi$ ) and velocity ( $U$ ) of the vessel, as already discussed in one of the previous sub-sections.

The velocity and heading for the estimation of the TF's (the green block) is obtained from historical GPS data. In combination with the radar data, the distance to the spatio-temporal origin ( $x, y$ ) and the remaining wave-components are calculated ( $\mu$  and  $\omega_e$ ). For the motion predictions in the blue and yellow block; As already discussed in one of the previous sub-section, under normal circumstances the heading ( $\Psi$ ), velocity ( $U$ ), and the geological location of the origin of the vessel ( $O$ ), have to be predicted as well. However, in this model they have been taken as known variables and are therefore are also directly adopted from the GPS data into the model.

In the red block, the predicted motions ( $\xi_i(t)$ ) based on the pre-calculated and estimated TF's are compared to the measured motions ( $\xi_{i,m}$ ). In Section 4.1 different assessment criteria are defined, which are used

to determine if the use of estimated-transfer functions ( $G_i(j\omega)$ ) will result in more accurate motion predictions.

#### Synthetic data driven model

Figure 2.6 shows the flow-chart of the synthetic model. The main difference with the previously discussed model is that the wave-components are synthetically generated. For the generation of those wave-components, the method as described by Goda [6] is used. In this method first a 2-D wave spectrum is defined where, with the use of a distribution-function, directional dependency is assigned to. This procedure is discussed in more detail in Appendix B. The difference to the wave-components obtained from the radar-data analysis, the synthetic components have the right amplitudes. As already discussed in Section 2.1, the wave-components obtained from the radar-data analysis need an additional scaling factor ( $\beta_i$ ) since no information about the true amplitude can be subtracted from the 2-D "images".

Another difference to the model based on sea-trial data, the vessel is kept at a fixed position. This means that the heading ( $\Psi$ ), velocity ( $U$ ), and the distance to the spatio-temporal origin ( $x, y$ ), are not taken into account. Furthermore, to simulate the measured motions  $\xi_{i,m}$  in the transfer-estimation block (green block), motion signals ( $\xi_{i,m}$ ) are created using Equation 2.16. These motion signals are generated with the same wave-components which are used for the generation of the force signal.

#### Verification and validation of the model

For the verification of the numerical models, motions calculated by pre-calculated TF's ( $H_{0,i}(j\omega)$ ) have been compared to those calculated by Next Ocean. The results were identical which verified the model. For the validation, in Section 4.1 assessment criteria will be defined to assess how accurate (or inaccurate) the motions are predicted compared to those measured.

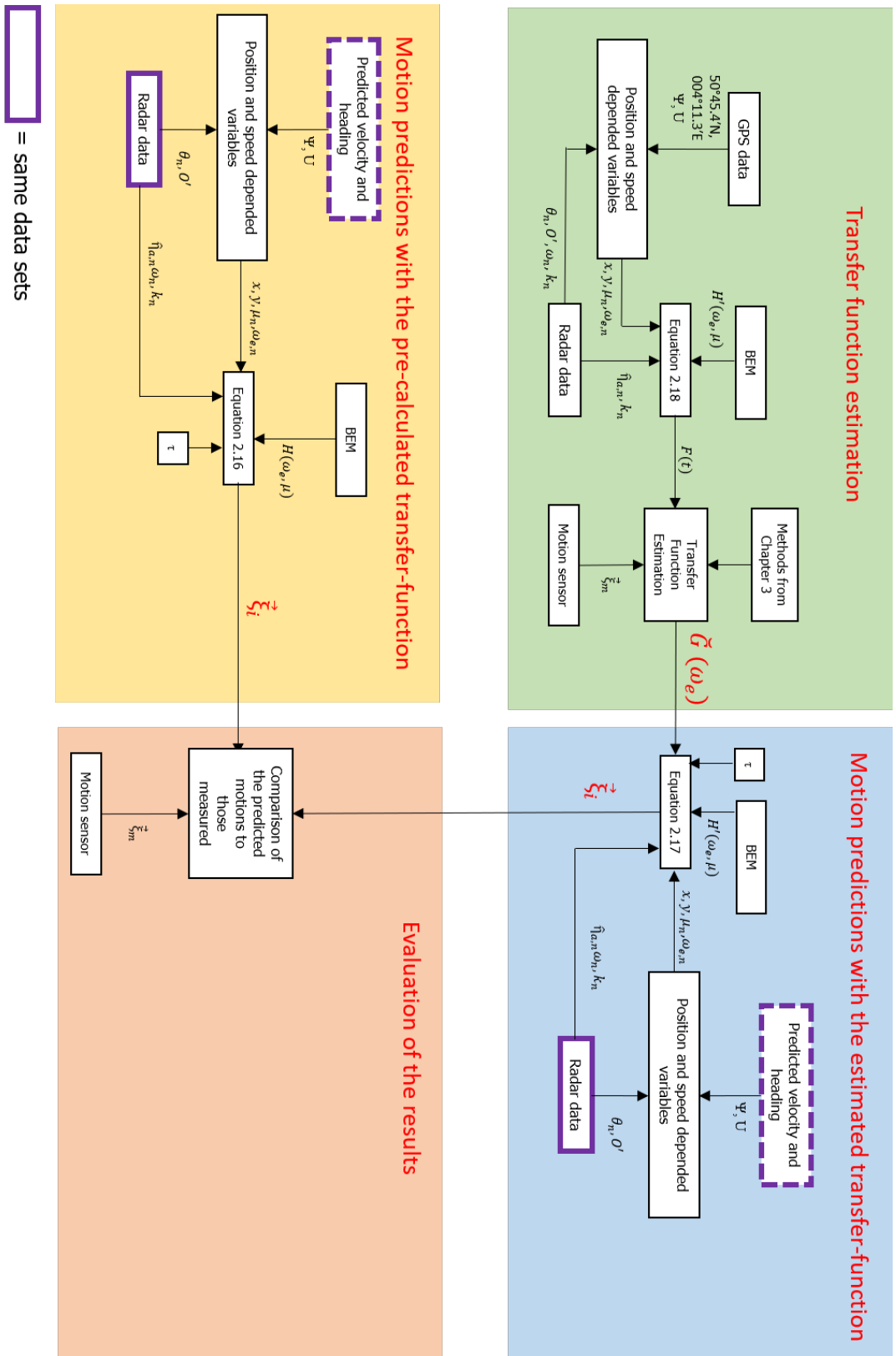


Figure 2.5: Flowchart of numerical model driven by sea trial data. In the green block the transfer-function is estimated by the methods as described in Chapter 3. In the yellow block the motions are predicted based on those pre-calculated TF's, Equation 2.16. In the blue block the motions are predicted by the estimated TF's, Equation 2.17. In the red block, the solutions based on the pre-calculated- and estimated TF's are compared to the measured motion signals.

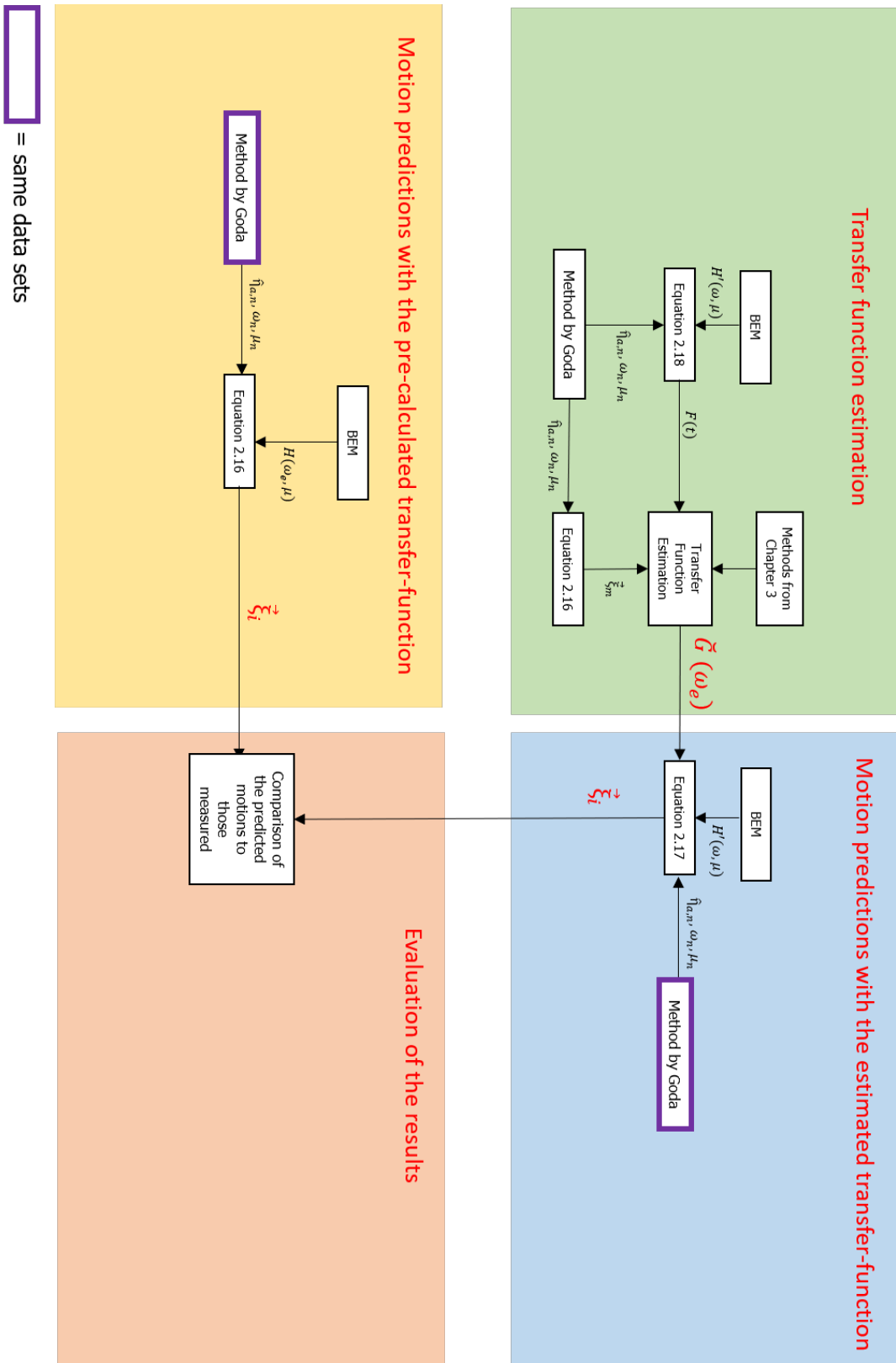


Figure 2.6: Flowchart of synthetic model. In the green block the transfer-function is estimated by the methods as described in Chapter 3. In the yellow block the motions are predicted based on those pre-calculated TF's, Equation 2.16. In the blue block the motions are predicted by the estimated TF's, Equation 2.17. In the red block, the solutions are compared and evaluated.



# 3

## Transfer Function Estimation

In this Chapter two methods will be presented on how to estimate transfer functions from measured motions and forces. The methods which will be discussed are the Empirical Transfer Function Estimation (ETFE) and the Cross Spectral Method (CSM), Section 3.1. Furthermore, different techniques will be discussed on how to improve the results using: window-functions and (Welch) averaging (Section 3.3). In Section 3.4 synthetically generated data will be used to evaluate the different estimation techniques, which will be used in Chapter 4.3 to estimate a transfer-function from sea trial data and eventually reconstruct and predict wave-induced ship motions.

Independent of the method chosen, the steps required to estimate a transfer-function, for the  $i$ -th DOF, are shown in Figure 3.1 and can be defined as follows: The recorded motion and force signal (a) are divided into  $M$  -overlapping- blocks and then modified using a window-function (b). Each block is then transformed from the time-domain into the frequency domain using a Fast Fourier Transformation (c). Using the frequency domain descriptions different methods are deployed (d) to estimated the transfer-function  $\check{G}_i(j\omega)$ (e).

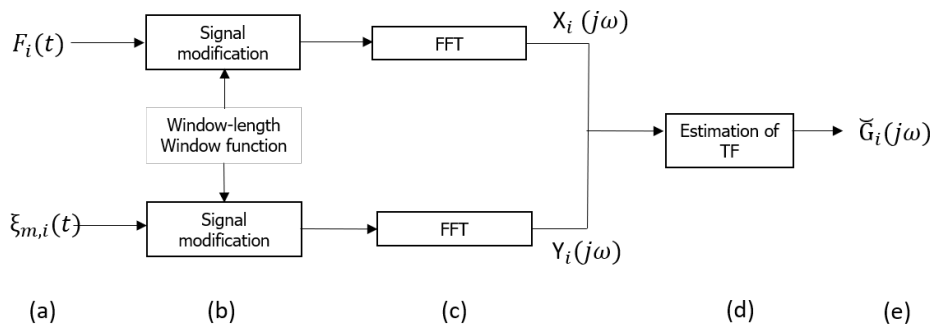


Figure 3.1: Flowchart for estimation of transfer function

### 3.1. Transfer function estimation methods

Before discussing methods to **estimate** transfer functions (TF's) -or more formally Frequency Response Functions (FRF)- and smoothing the results, the basic **system** which is concerned will be discussed. This is a **linear** time-invariant Single Input Single Output (SISO) system which **ideally** can be written for the  $i^{th}$  DOF in the time-domain as:

$$y_i(t) = g_{i,0}(t) * x_i(t) \quad (3.1)$$

where  $*$  denotes convolution,  $g_0$  is the (exact) unit impulse function,  $y(t)$  is the output,  $x(t)$  is the input. Relating this to the research, the output,  $y(t)$ , will be defined as the measured motions ( $\xi_{i,m}(t)$ ) and the input,  $x(t)$ , are the wave induced forces and moments ( $F_i(t)$ ). Now, by transforming the equation above from the time-domain into the frequency domain using a Discrete Fourier Transformation (DFT), see Appendix A

more information on this procedure, will results in:

$$Y(j\omega) = G_0(j\omega)X(j\omega) \quad (3.2)$$

where the  $j\omega$  notation has been chosen as a reminder that these Fourier Transforms are complex numbers. The ultimate goal is thus to **estimate** the true transfer-function  $G_0$  by using the data from  $x(t)$  and  $y(t)$ .

### Noise

A careful reader may have noticed that in the paragraphs above words such as: estimate, linear and ideally, have been emphasized. This is because the measured in and output signals are not ideal, which means that they are affected by noise, and not necessarily have to be linear. In other words, the measured input ( $x_i(t) = F_i(t)$ ) signal as given in equation 3.1 can be defined as:

$$x_i(t) = x_0(t) + n_x(t) \quad (3.3)$$

and for the output signal yields ( $y_i(t) = \xi_{i,m}(t)$ )

$$y_i(t) = y_0(t) + n_y(t) \quad (3.4)$$

where  $x_0$  and  $y_0$  represent the exact **linear** signals and  $n_x(t)$  and  $n_y(t)$  represents the noise disturbances. Noise in this sense are contributes to everything which is disturbing the **linear** system, and thus also non-linear phenomena. In the frequency-domain the two above expressions become:

$$X_i(j\omega) = X_0(j\omega) + N_X(j\omega) \quad (3.5)$$

$$Y_i(j\omega) = Y_0(j\omega) + N_Y(j\omega) \quad (3.6)$$

In this report it is assumed that the noise is uncorrelated to the in- and output and has a Gaussian distribution with a zero mean. These assumptions underlie the fundamental principles of estimation methods presented in the upcoming sections. In mathematical expressions the properties of noise are [21]:

$$\begin{aligned} \mathbb{E}\{N_X(j\omega)\} &= 0 & \mathbb{E}\{N_Y(j\omega)\} &= 0 \\ \mathbb{E}\{|N_X(j\omega)|^2\} &= \sigma_X^2(j\omega) & \mathbb{E}\{|N_Y(j\omega)|^2\} &= \sigma_Y^2(j\omega) \\ \mathbb{E}\{N_X(j\omega)N_Y^*(j\omega)\} &= \sigma_{XY}^2(j\omega) & \mathbb{E}\{N_Y(j\omega)N_X(j\omega)\} &= 0 \end{aligned} \quad (3.7)$$

where the  $\mathbb{E}$  symbol represents the expected value.

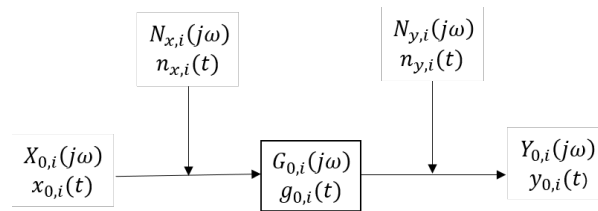


Figure 3.2: Basic system

### Discrete signals

In the equations as shown in the previous sub-sections are shown in continuous time and frequency while the actual signals are discrete. Figure 3.3 the difference between a continuous and discrete sampled signals is shown, where  $\Delta t$  is the time-step between each sample. The rate at which the the samples are collected will be referred to as the sampling-frequency and is calculated by:

$$f_s = \frac{1}{\Delta t}. \quad (3.8)$$

This sampling rate should be at least twice the highest frequency which occurs in the system to prevent under-sampling, also known as the Nyquist sampling theorem. The motion- and force signals used for the analysis

in this thesis are sampled at 10 Hz which is well above this limit ( $\sim 0.6$  Hz). Furthermore, the result of the DFT are discrete as well. The frequency step can be calculated by:

$$\Delta\omega = \frac{f_s}{N_s} \quad (3.9)$$

where  $N_s$  is the number of samples used for the DFT.

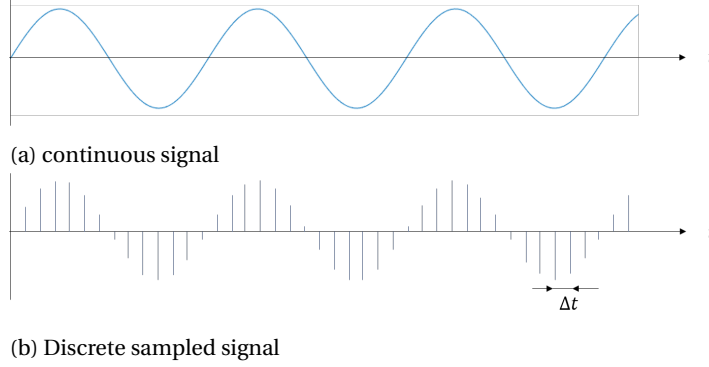


Figure 3.3: Difference between a continuous and discrete signal

### 3.1.1. Empirical Transfer Function Estimation

A commonly used method to estimate the TF's is by the Empirical Transfer Function Estimation method (ETFE). In this method the TF is directly estimated by dividing the frequency-domain description, as given in Equation 3.2, of the measured output by the frequency-domain description of the measured input, i.e. [11] [21]:

$$\check{G}_i(j\omega) = \frac{Y_i(j\omega)}{X_i(j\omega)} \quad (3.10)$$

where the notation  $\check{G}$  is chosen as a reminder that the TF's are estimates. As shown in the previous section the input and output are contaminated by noise and so the estimate TF contains errors. Furthermore, in Section 3.3.1 it will be shown that leakage errors will occur due to the Fourier Transformation itself [11] [21]. In other words, the TF which will be estimated can be defined as:

$$\check{G}(j\omega) := \frac{Y(j\omega)}{X(j\omega)} = \frac{Y_0(j\omega) + N_Y(j\omega)}{X_0(j\omega) + N_X(j\omega)} + T_G(j\omega) = G_0(j\omega) \frac{1 + N_Y(j\omega)/Y_0(j\omega)}{1 + N_X(j\omega)/X_0(j\omega)} + T_G(j\omega) \quad (3.11)$$

where  $T_G(j\omega)$  represents the contribution due to leakage as mentioned above.

#### Bias and variance properties

In general there are two main error sources that can be distinguished, which together form the total error, variable errors and systematic errors. To understand some of the basic principles/ properties of the systematic and variable errors, in the upcoming paragraphs the explanation by Pintelon et. al [21] will be followed.

To evaluate the systematic error, bias ( $b(j\omega)$ ), and the variability, variance  $var(j\omega)$ , in the approximation as given in equation 3.11 the -transient- term ( $T_G(j\omega)$ ) will be neglected and the remaining terms can be written as an -equivalent- Taylor Series expansion [21] which yields:

$$\check{G}_N(j\omega) = G_0(j\omega) \left( 1 + \frac{N_Y(j\omega)}{Y_0(j\omega)} \right) \left( 1 - \frac{N_X(j\omega)}{X_0(j\omega)} + \left( \frac{N_X(j\omega)}{X_0(j\omega)} \right)^2 + \text{higher order} \right) \quad (3.12)$$

Due to this notation all the terms after the true TF ( $G_0(j\omega)$ ) are related to the errors that may occur.

Neglecting the terms higher than first order, the bias error is defined as the absolute difference between the expected and true TF which thus results in:

$$b(j\omega) := |\mathbb{E}\check{G}(j\omega) - G_0(j\omega)| = \left| \mathbb{E} \left[ G_0 \left( 1 + \frac{N_Y(j\omega)}{Y_0(j\omega)} \right) \left( 1 - \frac{N_X(j\omega)}{X_0(j\omega)} \right) \right] - G_0(j\omega) \right| \quad (3.13)$$

where  $X_0(j\omega_n) \neq 0$  and  $Y_0(j\omega_n) \neq 0$ . Evaluating this equation, one can observe that noise will not generate a bias error, as according to equation 3.7  $\mathbb{E}\{N_X(j\omega)\} = 0$  and  $\mathbb{E}\{N_Y(j\omega)\} = 0$ . However, the approximation as given above does not take the -transient- leakage errors into account which are related to the DFT itself, this will be explained in more detail in 3.3.1, and decays as  $1/\sqrt{N_s}$ .

Now for the variance, this is per definition the expected value of the difference between the estimated and expected transfer-function squared. i.e.:

$$\text{var}(\check{G}(j\omega)) = \mathbb{E}\left[|\check{G}(j\omega) - \mathbb{E}\check{G}(j\omega)|^2\right] \quad (3.14)$$

Following the same manner of reasoning as for the bias, by approximating the estimated TF using the first order terms only knowing that  $\mathbb{E}\check{G}(j\omega) = G_0(j\omega)$  as  $N_s \rightarrow \infty$  [7] results in:

$$\text{var}(\hat{G}(j\omega)) = |G_0(j\omega)|^2 \left( \frac{\sigma_X^2(j\omega)}{|X_0(j\omega)|^2} + \frac{\sigma_Y^2(j\omega)}{|Y_0(j\omega)|^2} - 2\Re\left(\frac{\sigma_{XY}(j\omega)}{Y_0(j\omega)X_0^*(j\omega)}\right) \right) \quad (3.15)$$

From this equation it clearly can be seen that the variance will depend on the terms like  $\frac{\sigma_X^2(j\omega)}{X_0(j\omega)^2}$  which directly are related to the signal-to-noise ratio which is defined as:

$$SNR = \frac{\sigma_{\text{signal}}}{\sigma_{\text{noise}}} \quad (3.16)$$

From equation 3.15 and the definition of the SNR as given above, one may notice that the variance can only be small if the SNR ratio is high, i.e.  $\sigma_{\text{signal}} \gg \sigma_{\text{noise}}$ . However, unlike the bias error, the variance will not vanish for stochastic signals [11] [7]. A brief explanation why: When -for example- a sine wave with frequency  $\omega_k$  is generated, on every period new energy/ information is added to  $X_0(\omega_k)$  and  $Y_0\omega_k$ , which thus makes the variance decrease (see Equation 3.15). For stochastic signals however, increasing the number of samples will result in a more dense frequency grid but the energy/ information will also be distributed over those -multiple- frequencies.

Summarizing the properties above, the ETFE for a stochastic signal has the following properties [11] [7]:

- The ETFE is asymptotically unbiased, i.e.  $\lim_{N_s \rightarrow \infty} \mathbb{E}G(e^{i\omega}) = G_0(e^{i\omega})$ .
- The variance does not decrease with an increasing number of samples and converges to  $\frac{\Phi_{yy}(\omega)}{\Phi_{xx}(\omega)}$ <sup>1</sup>.
- The ETFE at different frequency's are asymptotically uncorrelated.

### Averaging

To reduce the poor variance behaviour of the transfer-functions estimated by the ETFE first, the full length of the signal is divided into  $M$  blocks each containing  $l_w$  samples. Second, for each block the in- and output signals are transformed into the frequency domain using the DFT. Finally, to estimate the TF's the frequency-domain descriptions of each block are averaged in the following way [11]:

$$\check{G}_i(j\omega) = \frac{1}{M} \sum_{m=1}^M \frac{Y_i^m(j\omega)}{X_i^m(j\omega)} \quad (3.17)$$

This method will be referred to as the averaged Empirical Transfer Function Estimation method ( $\overline{ETFE}$ ). The parameter  $l_w$  related to the window-length which will be discussed in more detail in Section 3.3.1. One should notice that the numerator and the denominator is divided simultaneously, due the phase relation between  $X(j\omega)$  and  $Y(j\omega)$ .

A brief explanation why the numerator and the denominator simultaneously have to be divided: Since the signals are stochastic the phase angles in each block will be randomly distributed. When the blocks are averaged separately this results in  $\mathbb{E}\left[\frac{1}{M} \sum_{m=1}^M Y_i^m(j\omega)\right] = 0$  and  $\mathbb{E}\left[\frac{1}{M} \sum_{m=1}^M X_i^m(j\omega)\right] = 0$ . One may suggest

<sup>1</sup>See Section 3.2 & 3.1.2 for the definitions of  $\Phi_{yy}(\omega)$  and  $\Phi_{xx}(\omega)$

that by zero-padding<sup>2</sup> the signals to a fixed time origin, the phase angles will no longer be randomly distributed and thus the numerator and denominator can be averaged separately, i.e.  $\mathbb{E}[\frac{1}{M} \sum_{m=1}^M Y_i^m(j\omega)] \neq 0$  and  $\mathbb{E}[\frac{1}{M} \sum_{m=1}^M X_i^m(j\omega)] \neq 0$ . However, in Section 4.4 it will be numerically shown that this way of averaging will not result in a better approximation for  $\check{G}(j\omega)$ .

Although averaging, by Equation 3.17, will counteract the poor variance behaviour, still large outliers may occur when  $Y_m(j\omega) \gg X_m(j\omega)$  due the presence of noise. In the next section it will be shown that the numerator and denominator can be separately be averaged when the CSM method is used, which resolves the problem due to the outliers.

### 3.1.2. Cross-Spectral method

In the previous section it was shown that estimating the TF with the ETFE method results in a rough estimation of the true TF, due to the poor variance. In this section another method will be presented which -partaly- resolves this problem and is called the cross-spectral method (CSM). It first will be shown that the CSM has a -very- strong relation with the ETFE as mentioned in the previous section, but has an additional advantage when the solutions are averaged.

#### Connection to the ETFE

The proof of the connection starts with multiplying both sides of equation 3.1 with  $x(t - \tau)$  [2] [7]:

$$y(t)x(t - \tau') = g_o(t) * x(t)x(t - \tau') \quad (3.18)$$

which can be rewritten to an equivalent form defined as:

$$R_{yx}(\tau') = g_o(t) * R_{xx}(\tau') \quad (3.19)$$

where  $R_{yx}(\tau')$  is called the cross-correlation function,  $R_{xx}(\tau')$  is the auto-correlation function, and  $\tau'$  is an additional time parameter. Transforming the equation from above into the frequency-domain yields:

$$\Phi_{yx}(j\omega) = G_0(j\omega)\Phi_{xx}(\omega) \quad (3.20)$$

where  $\Phi_{yx}(j\omega)$  is known as the cross-spectral density function and  $\Phi_{xx}(j\omega)$  is known as the auto-spectral density function, which will be shorthanded as cross- and auto-spectra in further notations.

If it assumed that the process is quasi-stationary then, by definition, the cross-correlation function is defined as [7]:

$$R_{yx}(\tau') := \mathbb{E}[y(t)x(t - \tau')] = \lim_{N_s \rightarrow \infty} \frac{1}{N_s} \sum_{t=0}^{N_s-1} [y(t)x(t - \tau')]. \quad (3.21)$$

From this equation it follows that the most straightforward way to estimate this function is by [7]:

$$\check{R}_{yx}(\tau') = \frac{1}{N_s} \sum_{t=0}^{N_s-1} [y(t)x(t - \tau')]. \quad (3.22)$$

By substituting this equation into the definition of the DFT (See Appendix A), this results in an estimation of the cross-spectrum of:

$$\check{\Phi}_{yx}(j\omega) = \frac{1}{N_s} Y(j\omega)X^*(j\omega) \quad (3.23)$$

where  $^*(j\omega)$  denotes that the complex conjugate should be taken.

Following a similar procedures as for the cross-spectra, also for the auto-spectra a relation to the DFT can be found:

$$\check{\Phi}_{xx}(\omega) = \frac{1}{N_s} X(j\omega)X^*(j\omega). \quad (3.24)$$

<sup>2</sup>Zero-padding is a technique where a number of zero's are added to a signal to decrease  $\Delta\omega$ .

By substituting the auto- and cross-spectra as defined above in Equation 3.20, the transfer function for the  $i$ -th DOF can be estimated by:

$$\check{G}_i(j\omega) := \frac{\check{\Phi}_{i,yx}(j\omega)}{\check{\Phi}_{i,xx}(j\omega)} = \frac{Y_i(j\omega)X_i^*(j\omega)}{X_i(j\omega)X_i^*(j\omega)}. \quad (3.25)$$

The above mentioned method to estimate the TF will be referred to as the  $CSM_1$  method in further notation. By following a similar derivation as for the  $CSM_1$  method, a second estimation method can be derived by multiplying both sides of equation 3.1 with  $y(t - \tau')$ . This alternative method will be defined as  $CSM_2$  where the TF's can be estimated by the following equation:

$$\check{G}_i(j\omega) := \frac{\check{\Phi}_{i,yy}(j\omega)}{\check{\Phi}_{i,xy}(j\omega)} = \frac{Y_i(j\omega)Y_i^*(j\omega)}{X_i(j\omega)Y_i^*(j\omega)} \quad (3.26)$$

The two estimation methods as given above will by definition be equivalent to the ETFE, see equation 3.10, and thus will hold the same bias and variance properties, for one single realization. However, by multiplying the equation with the complex conjugate of one of the signal itself, the denominator or numerator (depending on which definition observed) becomes a real value, i.e. the phase information is in the numerator or denominator. This has an advantage which will be shown in the following sub-section.

### Averaging

For the  $\overline{ETFE}$  it was stated that averaging has to be performed for the whole fraction at once, due to the fact that the phase angles of  $X_i(j\omega)$  and  $Y(j\omega)$  are related. However, since the denominator of the  $CSM_1$  only contains a real number the numerator and denominator can be averaged separately. Of course the same applies for the  $CSM_2$  but then for the numerator. This result for the  $\overline{CSM_1}$  in:

$$\check{G}_i(j\omega) := \frac{\check{\Phi}_{i,yx}(j\omega)}{\check{\Phi}_{i,xx}(j\omega)} = \frac{\frac{1}{M} \sum_{m=1}^M Y_i^m(j\omega) X_i^{*m}(j\omega)}{\frac{1}{M} \sum_{m=1}^M X_i^m(j\omega) X_i^{*m}(j\omega)} \quad (3.27)$$

and for the  $\overline{CSM_2}$  in:

$$\check{G}_i(j\omega) := \frac{\check{\Phi}_{i,yy}(j\omega)}{\check{\Phi}_{i,xy}(j\omega)} = \frac{\frac{1}{M} \sum_{m=1}^M Y_i^m(j\omega) Y_i^{*m}(j\omega)}{\frac{1}{M} \sum_{m=1}^M X_i^m(j\omega) Y_i^{*m}(j\omega)}. \quad (3.28)$$

By averaging the numerator and denominator separately the problem of the outliers due to the variance is significantly reduced but an additional problem arises. Evaluating this problem for the  $\overline{CSM_1}$ , since [21]:

$$\text{a.s. } \lim_{M \rightarrow \infty} \approx G_0(j\omega) \frac{1 + \sigma_{YX}^2(j\omega) / \mathbb{E}\{Y_0(j\omega)X_0^*(j\omega)\}}{1 + \sigma_X^2(j\omega) / \mathbb{E}\{X_0(j\omega)X_0^*(j\omega)\}} \quad (3.29)$$

an additional bias error will arise, which did not appear in the ETFE, which only will be zero if  $\sigma_X^2(j\omega) = 0$  and  $\sigma_{XY}^2(j\omega) = 0$ . The same of course applies when the  $\overline{CSM_2}$  method is analyzed. The method which should be applied depends on the signal where the highest SNR can be found [21]. If a higher SNR can be found at the input signal ( $\xi_{i,m}(t)$ ) then the  $\overline{CSM_1}$  method should be used but if the SNR is much higher at the output ( $F_i(t)$ ) signal than the  $\overline{CSM_2}$  method should be deployed.

### 3.1.3. Summary estimation methods

In the previous sections two different methods were shown to estimate the TF's, the Empirical Transfer Function Estimation method ETFE and the Cross-Spectral Method CSM. It has been shown that the CSM has a close relation with the ETFE when one single record is observed but results in different estimation when averaged. While the estimate of the TF by the  $\overline{ETFE}$  will suffer from outliers the estimation by the  $\overline{CSM}$  may result in an additional bias error. To summarize all the definitions of the estimation techniques, which will be

used in the rest of the report:

$$\begin{aligned}
\overline{ETFE/CSM}: \quad \check{G}_i(j\omega) &= \frac{Y_i(j\omega)}{X_i(j\omega)} \\
\overline{ETFE}: \quad \check{G}_i(i\omega) &= \frac{1}{M} \sum_{m=1}^M \frac{Y_i^m(j\omega)}{X_i^m(j\omega)} \\
\overline{CSM}_1: \quad \check{G}_i(j\omega) &= \frac{\frac{1}{M} \sum_{m=1}^M Y_i^m(j\omega) X_i^{*m}(j\omega)}{\frac{1}{M} \sum_{m=1}^M X_i^m(j\omega) X_i^{*m}(j\omega)} \\
\overline{CSM}_2: \quad \check{G}_i(j\omega) &= \frac{\frac{1}{M} \sum_{m=1}^M Y_i^m(j\omega) Y_i^{*m}(j\omega)}{\frac{1}{M} \sum_{m=1}^M X_i^m(j\omega) Y_i^{*m}(j\omega)}
\end{aligned} \tag{3.30}$$

### 3.2. Spectral density functions, coherence function & variance

In the previous section it was shown that in CSM cross- and auto-spectra are used for the estimation of the transfer-function. Using such spectra can be appealing in such a way that they are related to "energy", or more formally spectral-density functions. To recall from that section, the following system for estimating the TF's was defined [7] [11]:

$$\Phi_{yx}(j\omega) = G_0(j\omega)\Phi_{xx}(\omega); \tag{3.31}$$

In this equation there are no contributions to noise. This is because noise contributions (which will be generalized in further notations as  $v(t)$ ) are uncorrelated to the in- and output signal, i.e.  $\Phi_{vx}(j\omega) = 0$  and  $\Phi_{vy}(j\omega) = 0$ . However, noise will subtract energy from the system and therefore also the following equilibrium should be satisfied:

$$\Phi_{yy}(\omega) = |G_0(j\omega)|^2\Phi_{xx}(\omega) + \Phi_{vv}(\omega); \tag{3.32}$$

where  $\Phi_{vv}(\omega)$  represents the noise contained in the system. By substituting Equation 3.31 into 3.32 an estimation for the noise spectrum can be made:

$$\check{\Phi}_{vv}(\omega) = \check{\Phi}_{yy}(\omega) - \frac{|\check{\Phi}_{yx}(j\omega)|^2}{\check{\Phi}_{xx}(\omega)} \tag{3.33}$$

where, to recall from the previous section, the auto- and cross-spectra should be calculated by:

$$\Phi_{yx}(j\omega) = \frac{1}{MN_s} \sum_{m=1}^M Y_i^m(j\omega) X_i^{*m}(j\omega) \tag{3.34}$$

$$\Phi_{yy}(\omega) = \frac{1}{MN_s} \sum_{m=1}^M Y_i^m(j\omega) Y_i^{*m}(j\omega) \tag{3.35}$$

$$\Phi_{xx}(\omega) = \frac{1}{MN_s} \sum_{m=1}^M X_i^m(j\omega) X_i^{*m}(j\omega) \tag{3.36}$$

Basically, the noise estimate as given above is nothing more than the difference between the measured auto-spectra ( $\Phi_{yy}(\omega)$ ) and calculated auto-spectrum based on estimated TF's ( $|\check{G}_i(j\omega)|^2\Phi_{xx}(\omega)$ ). The use such noise estimations is of interest because it gives an indication about how well two frequencies are correlated. Two signals become uncorrelated when  $Y_i^m(j\omega) X_i^{*m}$  gives a different solution (in amplitude and/ or phase) for every block  $m$ . Possible sources noise sources are [21]:

- A nonlinear distortion, like the non-linear behaviour of ship motions.
- Other inputs beside  $x(t)$  which contributes to the output, like wind, steering and other external factors.
- Extraneous noise in the measurements, like a noise in sensors and due to modeling.
- Leakage errors due the DFT.

In the field of spectral analysis and system identification, there are two measures related to the noise estimate which are commonly used for the assessment of the system. The first, the so called Coherence function which is defined as [21] [11]:

$$\gamma_{XY}^2(\omega) := \frac{|\check{\Phi}_{yx}(j\omega)|^2}{\check{\Phi}_{xx}(\omega)\check{\Phi}_{yy}(\omega)}. \quad (3.37)$$

which provides a number between 0 and 1, as function of the frequency. If the Coherence function is 1 the frequencies are perfectly correlated while the opposite applies when the coherence function is 0. As for a second commonly used measure, from the coherence function also a direct estimation of the variance of  $\check{G}(j\omega)$  can be made. This can be calculated by [21]:

$$\check{\sigma}_{\check{G}}^2(j\omega) \approx |\check{G}(j\omega)|^2 \frac{1 - \gamma^2(\omega)}{\gamma^2(\omega)} \quad (3.38)$$

Because both the coherence and variance indicate how well the in- and out-put signals are correlated, they will be used in Section 4.2 and 4.3 as assessment criteria for the frequency-domain solutions.

### 3.3. Window-functions & Welch-averaging

In this section two methods will be discussed to improve the TF estimates, applying window-functions and Welch averaging. Window-functions are used to reduce the spectral leakage and Welch-averaging to recover the energy lost due to the applied window-function.

#### 3.3.1. Window function

As mentioned in Section 3.1.1 the quality of the estimated-transfer functions will be affected by a phenomena called spectral leakage, caused by the Discrete Fourier Transformation (DFT) [11] [21]. This phenomena occurs because one of the assumptions when using a DFT is that the signal is periodically extended outside the measured interval. Since for stochastic signals this is not the case additional frequency components will be generated. The generation of those additional frequency components can be explained by the following example: The solid black line in the upper-part of Figure 3.4 shows a time-domain description of a generated sine wave between 0 and ~ 12.5 seconds. As one may notice, the dashed and dotted lines are time-shifted copies the same sine wave periodically extended outside the measured interval. This extension outside the measured interval, in this case, results in additional frequencies within the frequency domain which are not present in the original signal. The result in the frequency-domain is shown in the bottom part of Figure 3.4, which should be 1 solid spike.

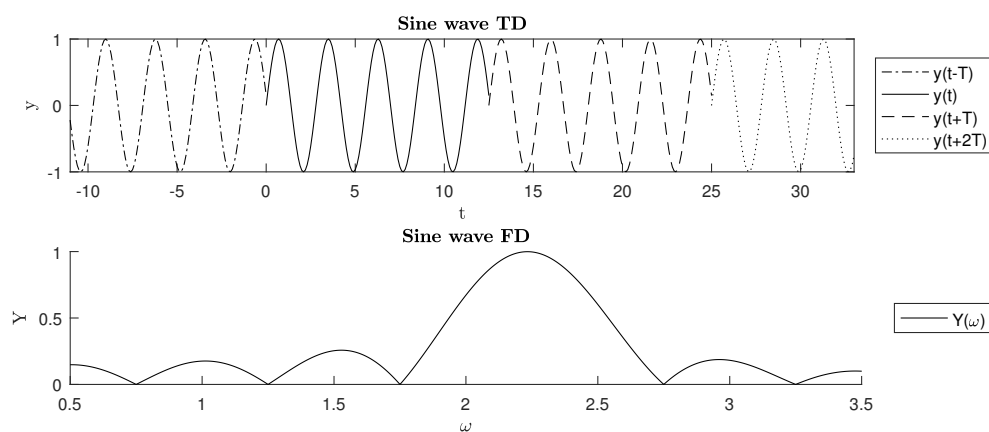


Figure 3.4: Example of a sine wave periodically extended outside the measured interval. The top figure gives the time-domain description and the bottom figure the frequency domain description

To reduce the effect of spectral leakage, so called window-functions are usually applied [11] [7] [21]. A window-function,  $w(t)$ , is a function which tempers the beginning and the end of a time-domain signal

within a certain interval and is zero outside that interval, illustrated in Figure 3.5. These-functions can be applied to the **measured** input and output signal, in the time-domain this yields:

$$w(t) \cdot y(t) = g(t) * (w(t) \cdot x(t)) \quad (3.39)$$

and in the frequency domain this yields:

$$W(\omega) * Y(\omega) = G(\omega) \cdot (W(\omega) * X(\omega)) \quad (3.40)$$

From the equations as given above it can be seen that due to the convolution in the frequency-domain it is easier to apply the window in the time-domain.

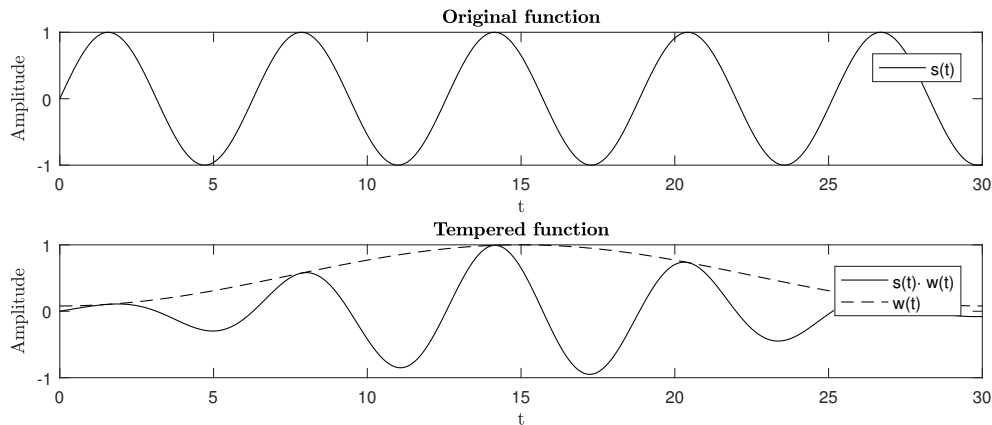


Figure 3.5: -Un- windowed sine wave

The window applied in Figure 3.5 was a Hamming window. Beside this window there are a lot of other window functions which can be used, all with their own characteristics which will be explained in the upcoming paragraphs. In this report three window-functions will be shown and evaluated:

- Hamming Window
- Rectangular Window (No window)
- Blackman-Harris window

There are 4 basic properties, illustrated in Figure 3.6, which can be defined when window-functions are evaluated:

- **Main lobe width at -3dB:** The width of the main lobe which indicates how many frequency **bins** next to the main lobe will be effected by spectral leakage. This is of special interest for TF's who have highly fluctuating dynamic behaviour. If two frequency components with a high gradient are close to each other the lower component can be buried underneath the higher component.
- **Scallop loss:** The maximum error which can occur. This error arises when the exact frequency component falls between the frequency components obtained from the DFT. Although a low scallop loss will result in a better amplitude estimation the main lobe width will increase as well. Therefore, a trade-off between scallop loss and main lobe width is required.
- **Highest side lobe level:** The height, in dB, of the first side lobe. This gives an indication of the spectral leakage outside the main lobe width. A high side lobe level results in less spectral leakage, outside the range of the main-lobe.
- **Side lobe falloff:** The rate at which the side lobes decreases.

Figure 3.7 shows a time-domain and frequency-domain description for three windows and Table 3.1 gives the corresponding characteristics [22]. One may notice from the table and figure that increasing the main

lobe width will decrease the scallop loss and side-lobe level. However, this thus also means a larger leakage of the main-lobe into the neighbouring frequencies bins. Therefore, in Section 3.4.3 the window-functions will be compared.

Beside the type of window, the window-length ( $w_l$ ) is also important. Figure 3.8 shows for  $w_l = 64$  and  $w_l = 512$  a frequency-domain description of the Hamming window. With more samples the frequency resolution increases which will result in a narrower main lobe when evaluated in the "frequency-space" rather than in the "sample-space". In other words, with an increasing window-length the effect of spectral leakage reduces (with  $1/\sqrt{w_l}$ ) since the main-lobe will be spread over a narrower frequency band. Although applying a window-function will reduce the effect of spectral leakage, it will never vanish [11].

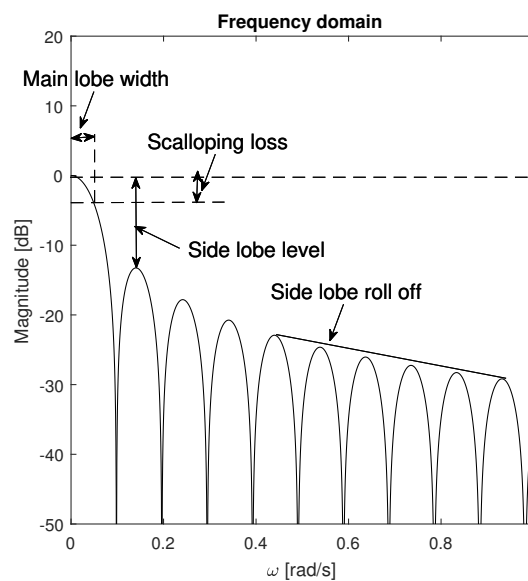


Figure 3.6: Properties of a window functions

Table 3.1: Characteristics of different window-functions

Window	Highest sidelobe level (dB)	Side lobe falloff (dB/octave)	Scallop loss (dB)	Main lobe width at -3dB (bins)
Rectangular	-13	-6	3.92	0.89
Hamming	-43	-6	1.78	1.3
Blackman Harris 4-sample	-74	-6	1.03	1.74

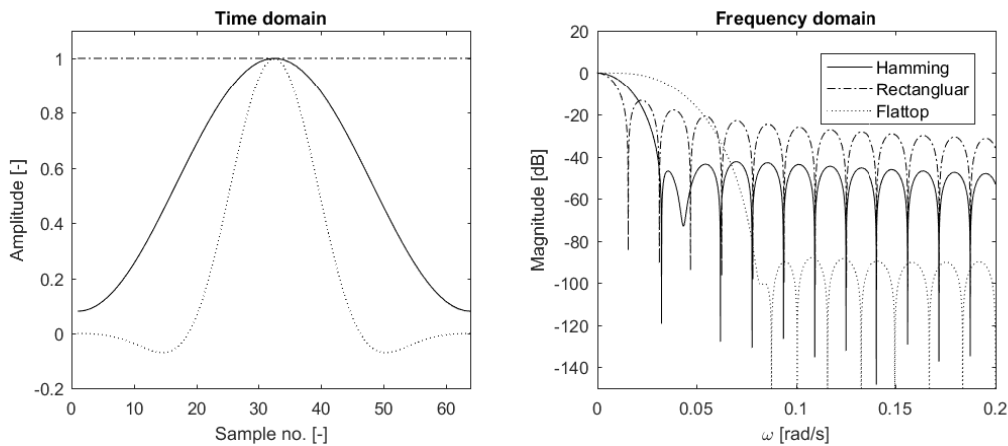


Figure 3.7: Comparison between window functions ( $N_s=64$  samples)

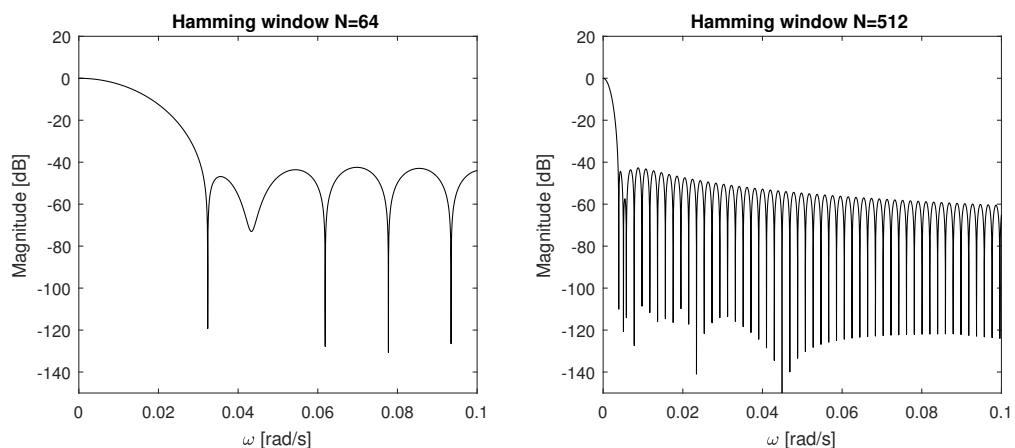


Figure 3.8: Hamming window with  $N_s=64$  and  $N_s=512$

### 3.3.2. Welch averaging method

In the previous section it was shown that spectral leakage can be reduced when the a window function is applied. The downside of this method is that information/ energy will be lost due to the tempering of the beginning and end of the signals. To overcome this problem, the total length of a record can be divided into  $M$  **overlapping** blocks, with a length of  $l_w$  samples, illustrated in Figure 3.9. Then, transforming the signals into the frequency domain and deploying one of the averaged estimation methods as given in Section 3.1 will provide a solution where most of the energy/ information is retained. This procedure is known as the Welch method or Welch averaging [11]. Although the amount of overlap can be varied from 0 to 100%, an overlap of more than  $\sim 50\%$  (depending on the amount of samples and type of window used) will not provide new information and will not significantly improve the results [11]. For all the averaged estimation techniques ( $ETFE$  and  $CSM_1$ ) in this report the amount of overlap will be kept at a fixed value of 75%.

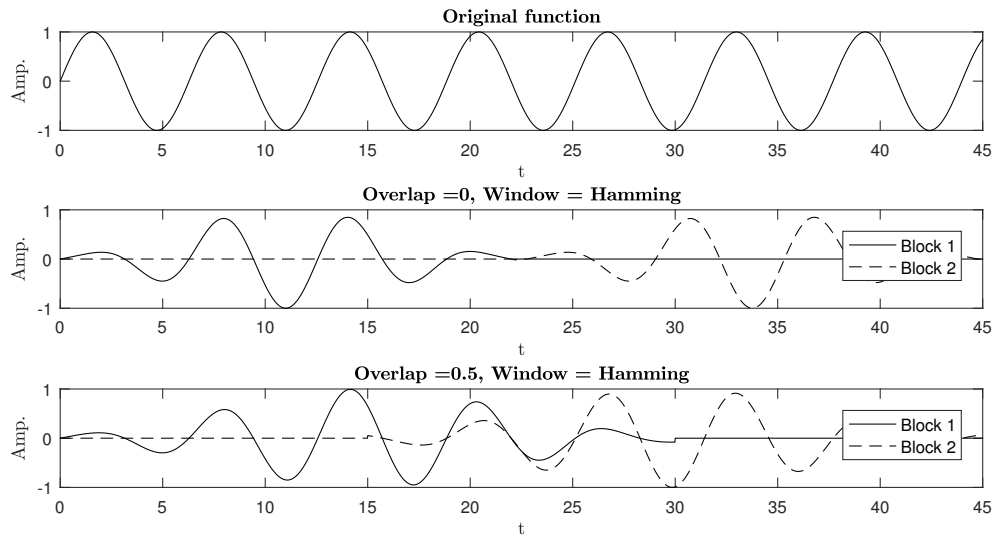


Figure 3.9: A sine wave divided into  $M = 2$  blocks. The top of the figure shows the original sine wave. The middle figure shows the same sine wave with 0% overlap. The bottom figure shows the sine wave with 50% overlap. In both the middle and bottom figure an Hamming window is applied

### 3.4. Transfer function evaluation

In Section 3.1 several methods were discussed on how a TF can be estimated from the calculated forces and measured motions. In Section 3.3 different techniques were discussed that smoothen the estimation methods, by reducing spectral leakage and Welch-averaging. In this section synthetically generated data will be used to analyze those estimation- and smoothing techniques, which will form the foundation of the estimation of the TF in the next chapter.

In the following sub-sections the following topics will be discussed:

- The effect of noise on the transfer function
- The effect of record- and window length
- The effect of different window functions

The results shown in this section have been obtained by the numerical model as described in Section 2.3. The wave-components are synthetically generated using the method proposed by Goda [6]. The wave-parameters have been chosen in such a way that they correspond to those during the sea trials, i.e. a JOHN-SWAP wave-spectra,  $T_p = 7.6$  [s],  $H_{1/3} = 2.2$  [m] [14], and a mean wave direction of  $\bar{\mu} = 1/4\pi$ . Furthermore, the sampling frequency ( $f_s$ ) of the motion and force signals has been set to 10 [Hz], which corresponds to the frequency used in the sea trial data.

#### 3.4.1. Effect of noise

In Section 3.1 it was stated that the presence of noise will affect the outcome of the estimated transfer-function. To recall, for the  $ETFE$  and  $\overline{ETFE}$  it is likely that a larger(er) variances may occurs while for the  $CSM$  a bias error may be created. Furthermore, as already discussed in Section 3.1.2, according to R. Pintelon and J. Schoukens [21] the choice between the  $\overline{CSM}_1$  or  $\overline{CSM}_2$  depends on which signal which contains the most noise. If the noise at the input signal is higher than the noise at the output signal, the  $\overline{CSM}_2$  method should be applied. When the noise at the output signal is higher than the noise at the input signal, the  $\overline{CSM}_1$  method should be applied. For the averaged, that is:  $\overline{ETFE}$   $\overline{CSM}_1$ , and  $\overline{CSM}_2$ , the following settings are used for estimation: An Hamming window, a window-length of  $w_l = 400$  [-], and an overlap of 75%.

In the upcoming paragraphs and next section Gaussian white noise is added to the **time-domain** motion- ( $\xi_{i,m}(t)$ ) and force ( $F_i(t)$ ) signals to study the effected on the estimation techniques. In order to add noise, the standard deviation of the noise is required for the Gaussian distribution function. As shown in Section 3.1.1 a quantity related to this is the SNR ratio defined as:

$$SNR = \frac{\sigma_{\text{signal}}}{\sigma_{\text{noise}}} \quad (3.41)$$

The standard deviation  $\sigma_{\text{signal}}$  can easily be calculated for the (undisturbed) force- and motion signals. By substituting these standard deviations with a pre-defined SNR ratio into the equation above, a standard deviation for noise ( $\sigma_{\text{noise}}$ ) can be obtained . In other words, the standard deviation for the noise at the output signal can be calculated by:

$$\sigma_{i,y} = \alpha \sigma_{\xi_{i,m}} \quad (3.42)$$

and the standard deviation noise at the input signal can be calculated by:

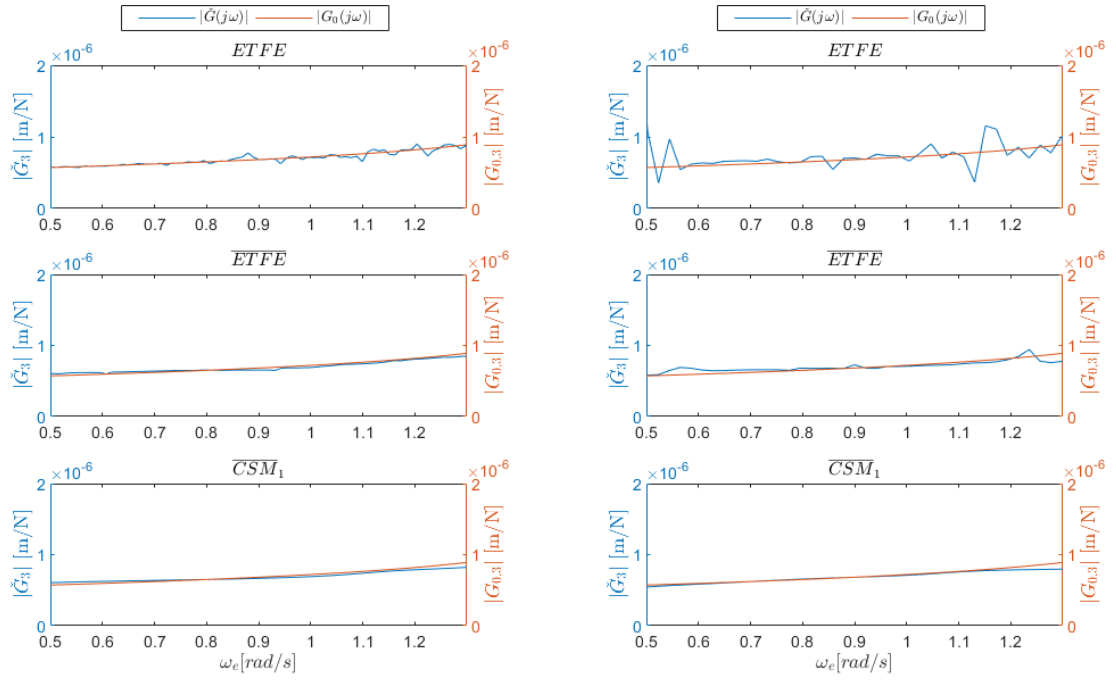
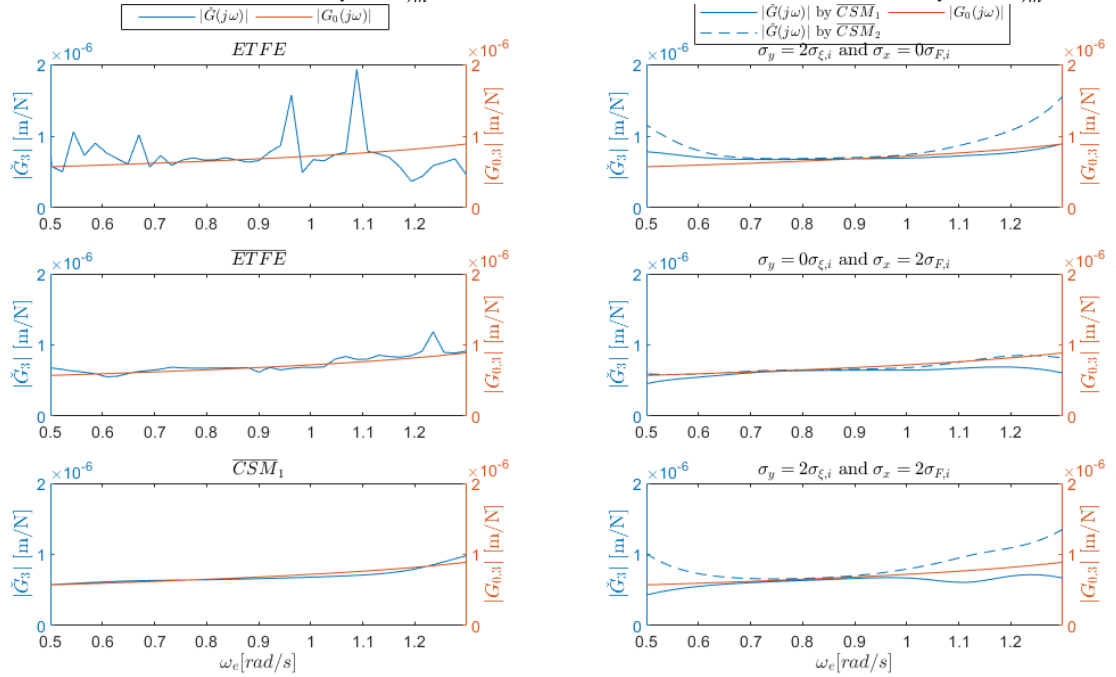
$$\sigma_{i,x} = \alpha \sigma_{F_i}. \quad (3.43)$$

were the factor  $\alpha = \frac{1}{SNR}$ . By increasing  $\alpha$  more noise will added to the signal observed. In the following paragraphs first, noise will be added to the output-signal ( $\xi_{i,m}(t)$ ) for the evaluation of the ETFE,  $\overline{ETFE}$ , and  $\overline{CSM}_1$ . In this signal the highest noise level, i.e. lowest SNR ratio, can be expected due to the non-linear behaviour of ship motions. Seconly, noise will be added to the in- and/or output signal for the evaluation of the  $\overline{CSM}_1$  and  $\overline{CSM}_2$ . This because, as already mentioned above the choice between the  $\overline{CSM}_1$  or  $\overline{CSM}_2$  depends on which signal which contains the most noise.

Figure 3.10a till 3.10c shows for an increasing noise level at the output signal, the TF's ( $\check{G}_i(j\omega)$ ) estimated by the ETFE,  $\overline{ETFE}$ , and  $\overline{CSM}_1$ . As shown in Figure 3.10a, when the signal is free of noise the estimated TF's ( $\check{G}_3(j\omega)$ ) are almost equivalent to the pre-calculated TF ( $G_{0,3}(j\omega)$ ). The largest deviations between the pre-calculated TF and the estimated TF can be found when the ETFE method is used. Increasing the noise level, as illustrated in Figure 3.10b and 3.10c, shows that the variable error strongly increases when the the ETFE is used for estimating the TF. For the  $\overline{ETFE}$  the variable error also increases but less than the ETFE results. This can be explained by he fact that averaging will decrease the variable error. When the results of the  $\overline{CSM}_1$  are compared to those of the  $\overline{ETFE}$ , it is shown that the estimations by  $\overline{CSM}_1$  are slightly better as those of the  $\overline{ETFE}$ .

Figure 3.10d shows the estimation of the TF by the  $\overline{CSM}_1$  and  $\overline{CSM}_2$ . In the top of the figure the results are shown where only noise is added to the output signal ( $\xi_{i,m}(t)$ ), in the middle figure noise is added only to the input signal ( $F_i(t)$ ), and in the bottom figure noise is added to both signals. When only noise is added to the output signal, the  $\overline{CSM}_1$  shows a lower bias error as the  $\overline{CSM}_2$ . With a similar amount of noise only added to the input signal, the opposite applies which means that the  $\overline{CSM}_2$  shows a lower bias error. When noise is added to both the input and output signal, the  $\overline{CSM}_1$  shows much a lower bias as the  $\overline{CSM}_2$ .

With the above observations made and the assumption that the most noise can be expected at the output signal, i.e. measured motions  $\xi_{i,m}$ , it can be concluded that the most accurate estimates of the transfer-functions probably will be obtained by the  $\overline{CSM}_1$  or  $\overline{ETFE}$  method.

(a) Comparison estimation methods:  $\sigma_y = 0\sigma_{\xi_m}$ (b) Comparison estimation methods:  $\sigma_y = 0.5\sigma_{\xi_m}$ (c) Comparison estimation methods:  $\sigma_y = 1\sigma_{\xi_m}$ 

(d) Comparison noise at in- and output CSM methods

Figure 3.10: Estimation the heave transfer-functions under the influence of noise. The red line in all the figures represents the pre-calculated TF. Figure 3.10a till 3.10c shows for an increasing noise level at the output signal, the estimated TF's by the ETFE,  $\overline{ETFE}$  and  $\overline{CSM}_1$ . Figure 3.10d shows the estimated TF's by the  $\overline{CSM}_1$ , and  $\overline{CSM}_2$ . In the top of the figure noise is only added to the output signal, in the middle noise is only added to the input signal, and in the bottom figure noise is added to both signals. For the averaged results, that is:  $\overline{ETFE}$ ,  $\overline{CSM}_1$ , and  $\overline{CSM}_2$ , the following settings are used: An Hamming window, a window-length of  $w_l = 400$  [-], and an overlap of 75%.

### 3.4.2. Signal & window length

In this section an analysis will be made between the maximum available time for training/estimating the TF and the window-length  $w_l$ . This evaluation is of interest because, increasing the window-length will decrease the bias error but increases the variable error, especially when one of the signals contains noise. This is also known as the bias-variance trade-off [11]. For the evaluation, a measure for the error between the estimated TF ( $\check{G}_i(j\omega)$ ) and the pre-calculated TF ( $G_{0,i}(j\omega)$ ) is defined. This error is the absolute difference between the amplitudes of the estimated TF ( $|\check{G}_i(j\omega)|$ ) and those pre-calculated ( $|G_{0,i}(j\omega)|$ ) integrated over the domain  $0.5 \leq \omega \leq 1.3$ , and averaged over  $R = 20$  realizations. I.e.:

$$\bar{\epsilon} = \frac{1}{R} \sum_{r=1}^R \int_{\Omega} \left| |\check{G}_i^r(j\omega)| - |G_{0,i}^r(j\omega)| \right| \quad (3.44)$$

Figure 3.11 shows this error for different window-lengths, as function of the total time available for training the TF. In the top of each figure the error is shown based on the  $\overline{CSM}_1$ , the middle figure shows the results based on the  $\overline{ETFE}$ , and the bottom figure shows the results based on the ETFE. For the ETFE, the window-length is (by definition) always equal to  $w_l = t \cdot f_s$ . The difference between the Figures 3.11a till 3.11c is the amount of noise added to the output signal. The noise at the output signal has been generated in the same way as discussed in the previous sub-section.

Figure 3.11a shows the errors when no noise is added to the output signal ( $\sigma_{i,y} = 0\sigma_{\xi_{i,m}}$ ). As shown in the figure, for the  $\overline{ETFE}$  and  $\overline{CSM}_1$  in general holds that increasing the training time will asymptotically decrease the error. This can be explained by the fact that more averages will reduce the variable error. The results of the  $\overline{CSM}_1$  also show that for a long training time ( $t = 800$ ) holds, increasing the window-length results in a lower error. This can be explained by the fact that by increasing the window-length more samples are evaluated, which reduces the leakage error by  $\frac{1}{\sqrt{N_s}}$  as discussed in Sections 3.1.1 and 3.3.1. One may also notice that the error of the  $\overline{CSM}_1$  is in general lower as the one of the  $\overline{ETFE}$ . This can be explained by the fact that the  $\overline{ETFE}$  is more sensitive for outliers, as explained in Section 3.1.1. The results of the ETFE (bottom figure) show that these errors are much higher as those of the  $\overline{ETFE}$  and  $\overline{CSM}_1$ .

Figure 3.11b and 3.11c show the errors of the estimated TF's, for an increased noise level at the output signal. In Figure 3.11b the results are shown with a standard deviation for noise of  $\sigma_{y,i} = 0.5\sigma_{\xi_{m,i}}$  and Figure 3.11c shows the results where  $\sigma_{y,i} = 1\sigma_{\xi_{m,i}}$ . As shown in the figures, increasing the noise level will in general result in larger errors. Furthermore, for the averaged estimation techniques ( $\overline{ETFE}$  and  $\overline{CSM}_1$ ) also the decay rate of the error decreases. This can be explained by the fact that the variable error increases and therefore more averages are required to reduce this error. Another observation which one can make between the results of the  $\overline{ETFE}$  and  $\overline{CSM}_1$ , the decay rate of the error where the TF's are estimated by  $\overline{CSM}_1$  is higher as the one those by  $\overline{ETFE}$ . Since the decay rate of the error decreases, a smaller window-lengths may be preferred when only a limited amount of training time is available. When the results of the ETFE are observed (bottom figures), the errors of the ETFE increases with an increased noise level and are much higher as those of the  $\overline{ETFE}$  and  $\overline{CSM}_1$ .

With the above observations made, it can be concluded that the choice of the window-length ( $w_l$ ) depends on the noise level in the signal and the total training time available.

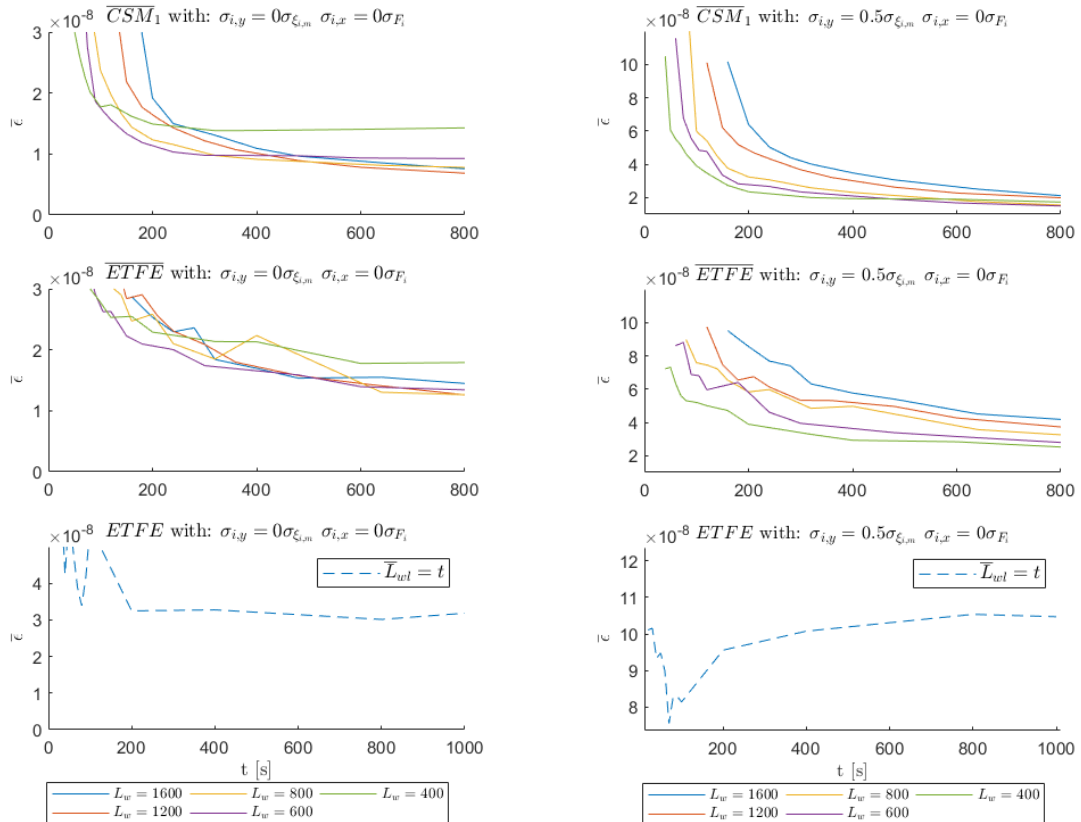
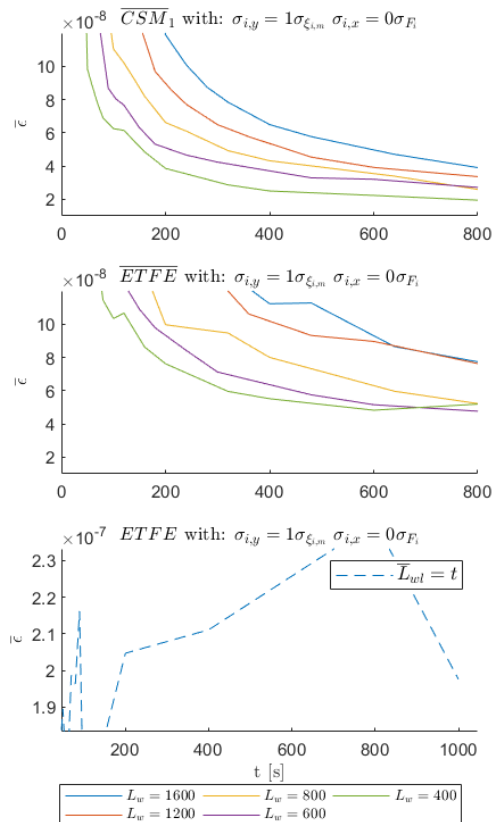
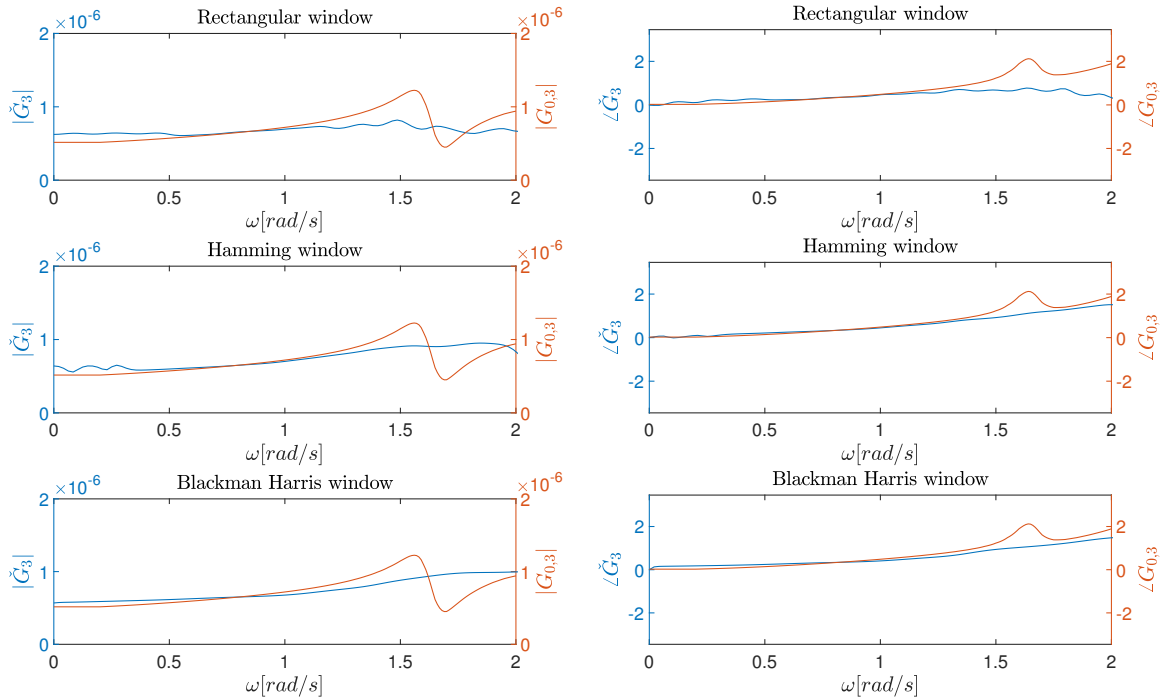
(a) Comparison estimation methods:  $\sigma_{y,i} = 0\sigma_{\xi_{m,i}}$ (b) Comparison estimation methods:  $\sigma_{y,i} = 0.5\sigma_{\xi_{m,i}}$ (c) Comparison estimation methods:  $\sigma_{y,i} = 1\sigma_{\xi_{m,i}}$ 

Figure 3.11: Errors between estimated- and pre-calculated transfer-functions, as function of window-length and total training-time for the TF's. In the top of all the figures the results are shown when the TF's are estimated by the  $\overline{CSM}_1$ , the middle figures show the results of the  $\overline{ETFE}$ , and the bottom figures show the results of the ETFE. The difference between the figures 3.11a till 3.11c are the noise levels at the output signal. For the averaged results, an Hamming window is applied with 75% overlap.

### 3.4.3. Window functions

In Figure 3.12 the estimated transfer functions are shown using different window functions. One may notice from the different estimates that the worst solutions are obtained when a Rectangular window is applied. Comparing the Hamming window to the Blackman-Harris window shows that a slight better solution can be obtained when a Hamming window is used, especially at  $\omega > 1$ .



(a) Amplitudes

(b) Phase angles

Figure 3.12: Comparison of different window functions. The transfer-functions are estimated by the  $\overline{CSM}_1$  with: a window-length of  $w_l = 400[-]$  and an overlap of 75%

### 3.4.4. Summary and discussion

In the previous sections several analysis were made to evaluate the different estimation methods as described in Section 3.1, driven by synthetically generated data. It is shown that due to the presence of noise bias- and variance errors occur. Especially the ETFE method will be affected by noise and therefore is not recommended for estimation the TF's. It also is shown that the  $\overline{CSM}_1$  is less influenced by noise than the  $\overline{CSM}_2$ . Comparing the  $\overline{CSM}_1$  to the  $\overline{ETFE}$  showed that the error faster decays when the TF's are estimated by the  $\overline{CSM}_1$ . Furthermore, in general applies that the longer the record the lower the error. Although a very long record in combination with a large window will result in a low(er) error, due to time limitations for training the TF's and the presence of noise a smaller window may be preferred.



# 4

## Results

The main objective of this research is to improve the accuracy of predicted wave-induced ship motions with the use of TF's estimated from measured motions ( $\xi_{i,m}$ ) and a now-cast prediction of the forces ( $F_i(t)$ ). In this section, the time- and frequency domain solutions resulting from these estimated TF's will be compared to the solutions where pre-calculated TF's are used. To recall from Section 2.3, in case that pre-calculated wave-to-motion transfer-functions ( $H_0(j\omega)$ ) are used the motions are predicted by:

$$\xi_i(x, y, t, \tau) = \mathbb{R} \left[ \sum_{n=1}^N \beta_i \hat{\eta}_{a,n} H_{0,i}(j\omega_{e,n}, \mu_n, U) e^{-j(\omega_n \cdot (t+\tau) + k_{x,n}x + k_{y,n}y)} \right] \quad (4.1)$$

while in the case of the estimated force-to-motion transfer-function ( $\check{G}_i(j\omega)$ ) the motions are predicted by:

$$\xi_i(x, y, t, \tau) = \mathbb{R} \left[ \sum_{n=1}^N \hat{\eta}_{a,n} H'_{0,i}(j\omega_{e,n}, \mu_n) \check{G}_i(j\omega_{e,n}) e^{-j(\omega_n \cdot (t+\tau) + k_{x,n}x + k_{y,n}y)} \right]. \quad (4.2)$$

In order to determine if the predicted motions are more accurate when estimated TF's are used, in Section 4.1 assessment criteria are defined. In Section 4.2 and 4.3 these criteria will be used for the evaluating the results. The difference between Section 4.2 and 4.3 is that in Section 4.2 synthetically generated data is while the results of 4.3 are based on sea-trial data. This chapter will end with a discussion about two different topics, Section 4.4.

### 4.1. Assessment criteria

In this section time- and frequency-domain criteria are presented which are used in Section 4.2 and 4.3 to evaluate if the use of estimated TF's ( $\check{G}(j\omega)$ ) will result in more accurate motion predictions. For the time-domain comparison, the cross-correlation coefficient is used to evaluate the linear relationship between the measured- and calculated motions, while the ratio of standard deviations will give an indication of the similarity between the amplitudes of the measured- and calculated motions. For the frequency-domain solutions, the motion response-spectra of the calculated- and measured motions will be compared. As already stated in Section 3.2, the difference between the motion response-spectra based on the estimated TF's ( $\check{G}(j\omega)$ ) and the measured motion-response spectra can be evaluated with the use of the so called Coherence function. Therefore, also this function will be used as an assesment criterea.

#### Time-domain criteria

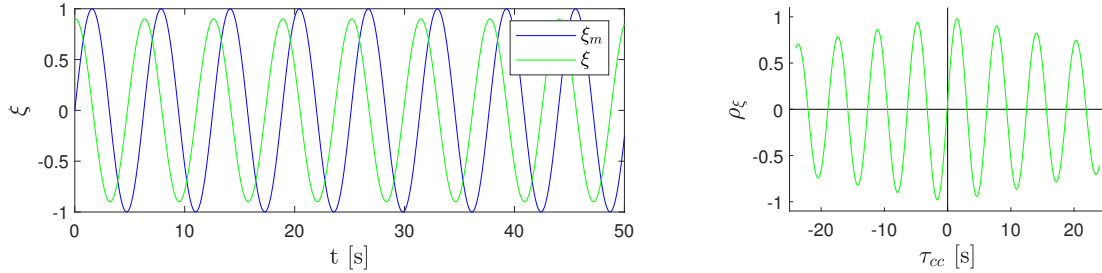
The cross-correlation coefficient ( $\rho_{\xi_i}(\tau_{cc})$ ) is an index between -1 and 1 which indicates how well two time-domain signals are **linearly** related and how much the signals lag from one-another. This parameter is commonly used in real time-motion prediction to compare the predicted motions against those measured [13][1].

This correlation coefficient can for the  $i$ -th DOF be calculated by:

$$\rho_{\xi_i}(\tau_{cc}) = \frac{1}{T} \int_0^T \frac{\xi_i(t) - \bar{\xi}_i}{\sigma_{\xi_i}} \frac{\xi_{i,m}(t + \tau_{cc}) - \bar{\xi}_{i,m}}{\sigma_{\xi_{i,m}}} dt, \quad (4.3)$$

where  $\xi_{i,m}$  represents the measured motion,  $T$  is the total time/ length of the record observed,  $\tau_{cc}$  is a time-shift operator, and  $\sigma_{\xi_i}$  and  $\sigma_{\xi_{i,m}}$  are the standard deviations. Below an illustrative example will be given how the outcome of this function should be interpreted.

Figure 4.1a shows an example of a measured sine wave ( $\xi_m$ ) with an amplitude of 1 -blue line- and a "calculated" sine wave ( $\xi$ ) with an amplitude of 0.9 -green line-. Both the waves have a frequency of  $\omega = 1$  [rad/s]. Furthermore, one may notice from the figure that  $\xi_m$  lags  $\sim 1.5$  [s] from  $\xi$  or equivalent that  $\xi$  is  $\sim 1.5$  [s] ahead of  $\xi_m$ . Figure 4.1b shows the cross-correlation coefficient between these two signals, as function of  $\tau_{cc}$ , calculated by Equation 4.3. From the figure, one may notice that the highest peak occurs around  $\tau_{cc} \approx 1.5$  [s], which is the same amount of lag as observed from Figure 4.1a, with a peak value of 1. This peak value of 1 indicates that the signals are fully **linear** related which means that their time-domain behavior is equivalent. This can be explained by the fact that both sine waves have the same frequency. However, as shown in Figure 4.1a the amplitudes of the sine waves are different and cannot be distinguished from this correlation function. Therefore, a second criteria will be defined in order to assess the similarities of the amplitudes of the measured and calculated motion signals.



(a) "Measured" sine wave ( $\xi_m$ ) and "calculated" sine wave ( $\xi_m$ )

(b) cross-correlation coefficient

Figure 4.1: An example for the interpretation of the cross-correlation coefficient. In the left figure: the blue line represents a measured signal ( $\xi_m(t)$ ) with an amplitude of 1 while the green line represents a calculated signal ( $\xi(t)$ ) with an amplitude of 0.9. Both the signals have a frequency of  $\omega = 1$  [rad/s]. The right figure shows the cross-correlation coefficient of the two signals by the green line.

For an assessment of the calculated amplitudes, a ratio of the standard deviations has been used. This ratio is the ratio between the standard deviation of the calculated motions and the measured motions, i.e.:

$$\sigma_{i,d} = \frac{\sigma_{\xi_i}}{\sigma_{\xi_{i,m}}}. \quad (4.4)$$

This ratio can be found in the work by Naaijen et. al [Naaijen2016] to determine the scaling/ correction of the calculated motions and by Alford et. al [1] to assess how well the amplitudes of the measured motions compare to those calculated. Ideally, this ratio should be 1 which means that the amplitudes of the calculated and measured motions are within the same range. A lower number means that the amplitudes are underestimated while a number higher than 1 indicates that the amplitudes are overestimated.

### Frequency-domain criteria

For the frequency-domain solutions the estimated transfer-functions ( $\check{G}_i(j\omega)$ ) will be visually compared to those pre-calculated ( $G_{0,i}(j\omega)$ ) to judge their similarity/ differences. However, such a comparison will not provide an answer to the question which method provides more accurate results. Therefore, it is more relevant to compare the motion response-spectra -or auto-spectra- of the calculated motions to the response-spectra of the measurements motions. A motion response-spectra can be estimated by:

$$\check{\Phi}_{i,yy}(\omega) = \frac{1}{NM} \sum_{m=1}^M Y_i^m(j\omega) Y_i^{*,m}(j\omega), \quad (4.5)$$

where the  $Y(j\omega)$  is the DFT of the measured- or calculated motion-signal, i.e.  $\xi_{i,m}(t)$  or  $\xi_i(t)$ . Furthermore, the calculated motions can either be obtained using the pre-calculated TF's  $H_{0,i}(j\omega)$  (Equation 4.1) or the estimated TF's  $\check{G}_i(j\omega)$  (Equation 4.2). One may notice that the difference between the motion response-spectra of the calculated- and measured motions is similar to the estimate of the noise spectra ( $\check{\Phi}_{\nu\nu}(\omega)$ ) as defined in Section 3.2 Equation 3.33.

In Section 3.2 it was also shown that noise estimates can be used to assess the quality of the system by a so called Coherence function and to estimate the standard deviation for the estimated TF's when the  $\overline{CSM}$  methods are used. To recall from that chapter, the coherence function is defined as [11]:

$$\gamma_i^2(\omega) = \frac{|\check{\Phi}_{i,yx}(\omega)|^2}{\check{\Phi}_{i,xx}(\omega)\check{\Phi}_{i,yy}(\omega)}, \quad (4.6)$$

where  $\check{\Phi}_{i,yy}$  can be calculated by the equation as shown above using the measured motions ( $\xi_{i,m}$ ) and the remaining spectra can be estimated by:

$$\check{\Phi}_{i,xx}(\omega) = \frac{1}{NM} \sum_{m=1}^M X_i^m(j\omega) X_i^{*,m}(j\omega) \quad (4.7)$$

$$\check{\Phi}_{i,yx}(j\omega) = \frac{1}{NM} \sum_{m=1}^M Y_i^m(j\omega) X_i^{*,m}(j\omega) \quad (4.8)$$

In the equations above,  $Y_i(j\omega)$  is the DFT of the measured motions and  $X(j\omega)$  is the DFT of a now-cast prediction of the forces. The result of the coherence function provides a number between 0 and 1 as a function of the frequency. Here 0 means that there is no correlation and 1 indicates a correlation between the in- and output, at a certain frequency. In Section 4.2 and 4.3 it will be shown that this function has a direct relation between the motion response-spectrum of the predicted and the one of the measured motions and therefore can be used as an assessment criteria.

Finally, to recall from Section 3.2 the coherence function can also be used to estimate the standard deviation of the TF's obtained through the  $\overline{CSM}$ . This can be calculated by:

$$\check{\sigma}_{\check{G}_i}^2 \approx |\check{G}_i(j\omega)|^2 \frac{1 - \gamma_i^2(\omega)}{\gamma_i^2(\omega)} \quad (4.9)$$

In Section 4.2 and 4.3 the standard deviation will be added to the estimated TF's. A large standard deviation will mean that there is a lot of variance in each block ( $m$ ) used to estimate the TF's.

## 4.2. Synthetic results

In this section a now-cast motion prediction will be made, driven by synthetic data, using the model as described in Section 2.3 with the transfer-function estimation techniques as described in Chapter 3. To recall from those chapters, first a set of time-domain motion and force signals is generated using synthetically generated wave components. After this set is generated, the motion- and force signals are used to estimate the TF's ( $\check{G}_i(j\omega)$ ) by -in this case- the  $\overline{CSM}_1$ . After the TF's are determined, a second set of wave-components is generated to make a prediction of the motions ( $\xi_i(t)$ ) using  $\check{G}_i(j\omega)$  and to generate the "measured" motions ( $\xi_{i,m}(t)$ ). Finally, the time- and frequency-domain solutions will be compared and assessed by the criteria given in the previous section. As already mentioned in section 3.4.4, beside an accurate solution it should also be obtained within a practical time limit. Therefore, the time limit for training the TF's has been set to 5 minutes.

The wave components required for the calculations have been synthetically generated by the method as described by Goda [6], which is explained in more detail in Appendix B. As input values for the generation of the wave-components, the same wave characteristics are chosen in such a way that they match those of the sea-trials in the next section. To recall this means: a JOHNSWAP wave-spectra,  $T_p = 7.6$  [s],  $H_{1/3} = 2.2$  [m][14], and a mean wave direction of  $\bar{\mu} = 1/4$  [ $\pi$ ]. Furthermore, the sampling frequency ( $f_s$ ) of the motion and force

signals has been set to 10 [Hz].

As mentioned above, in the upcoming sub-sections the results will be shown when the transfer-function is estimated using the  $\overline{CSM}_1$  method. Unless denoted otherwise, for the estimation an Hamming window has been used, a window-length of  $w_l = 400$  [-], and an overlap of 75%. As a final remark, the solutions will be shown for 6 degrees-of-freedom (DOF) of which the definitions are summarized in Table 4.1 as a reminder.

Table 4.1: Definitions degree of freedom

DOF	Notation	Unit	DOF	Notation	Unit
Surge	$\xi_1$	[m]	Roll	$\xi_4$	[rad]
Sway	$\xi_2$	[m]	Pitch	$\xi_5$	[rad]
Heave	$\xi_3$	[m]	Yaw	$\xi_6$	[rad]

### Time-domain comparison

Figure 4.2b shows the time-domain solutions of the synthetically generated measured motion ( $\xi_{i,m}$ ) -the blue line- and the motions obtained from the estimated transfer-function ( $\xi_i$ ) -the green line-. In almost all cases a perfect fit between the predicted- ( $\xi_i$ ) and measured-motions ( $\xi_{i,m}$ ) is shown. The largest deviations can be found at the roll- and yaw motions. Figure 4.2b shows the cross-correlation coefficients between the measured- ( $\xi_{i,m}$ ) and calculated motions ( $\xi_i$ ), obtained by Equation 4.3. To recall, this function shows the linear similarity between two signals and how much one lags from the other. The figure shows that in all cases this function is almost 1 at  $\tau = 0$  which means that the signals are almost perfectly related without any lag. This observation was also made from the time-domain solutions shown in Figure 4.2b.

In Section 3.4 it was shown that the accuracy of the TF's estimations depends on the amount of noise contained within the signals. Furthermore, it was also shown that in a noise free environment, in combination with an increased total time of estimating the TF's, in general holds that a larger window-length ( $w_l$ ) will result in a lower error. However, when noise is added to the system a shorter window was recommended to reduce the variable error. Therefore, in the two following paragraphs the time-domain results will be presented in a noise-free environment ( $\sigma_y = 0$ ) and an environment where noise is present ( $\sigma_y \neq 0$ ). In more detail, first noise has been added to the time-domain motion signal from which the TF's are estimated. Second, those estimated TF's ( $\check{G}_i(j\omega)$ ) are used to predict the ship motions (in a noise free environment).

For the first case, Table 4.2 shows the maximum cross-correlation coefficients for an increasing window length ( $w_l$ ) in a noise free environment ( $\sigma_y = 0$ ). It can be seen from the figure that increasing the window-length results in a higher maximum correlation-coefficient. This is what one may expect since it was already shown in the previous section that increasing the window length will decrease the total error on the transfer function.

For the second case, Table 4.3 shows the maximum correlation coefficients in the case that the TF's are estimated under the presence of noise which, after estimation, were used to make a noise free motion prediction. The results presented in the table show that increasing the window-length will not longer guarantee a lower correlation coefficient.

Table 4.2: Maximum cross-correlation coefficients in a noise free environment ( $\sigma_y = 0$ ), for an increasing window-length ( $w_l$ ). For the estimation of the TF's the  $\overline{CSM}_1$  has been used with an Hamming window and 75% overlap. The total amount of time for training the TF's has been limited to 5 min

$w_l$ [-]	Surge	Sway	Heave	Roll	Pitch	Yaw
	$\rho_{\xi_1}$	$\rho_{\xi_2}$	$\rho_{\xi_3}$	$\rho_{\xi_4}$	$\rho_{\xi_5}$	$\rho_{\xi_6}$
400	0.9906	0.9945	0.9984	0.9848	0.9976	0.9857
800	0.9925	0.9894	0.9985	0.9932	0.9973	0.9879
1600	0.9992	0.9992	0.9996	0.9946	0.9991	0.9811

Table 4.3: Maximum cross-correlation coefficients where the TF is estimated under the presence of noise ( $\sigma_y = 1\sigma_{\xi_{i,m}}$ ), for an increasing window-length ( $w_l$ ). For the estimation of the TF's the  $\overline{CSM}_1$  has been used with an Hamming window and 75% overlap. The total amount of time for training the TF's has been limited to 5 min

$w_l$ [-]	Surge	Sway	Heave	Roll	Pitch	Yaw
	$\rho_{\xi_1}$	$\rho_{\xi_2}$	$\rho_{\xi_3}$	$\rho_{\xi_4}$	$\rho_{\xi_5}$	$\rho_{\xi_6}$
400	0.9875	0.9827	0.9967	0.9673	0.9917	0.8955
800	0.9957	0.9915	0.9942	0.9912	0.9985	0.9807
1600	0.9663	0.9485	0.9532	0.9699	0.9623	0.9302

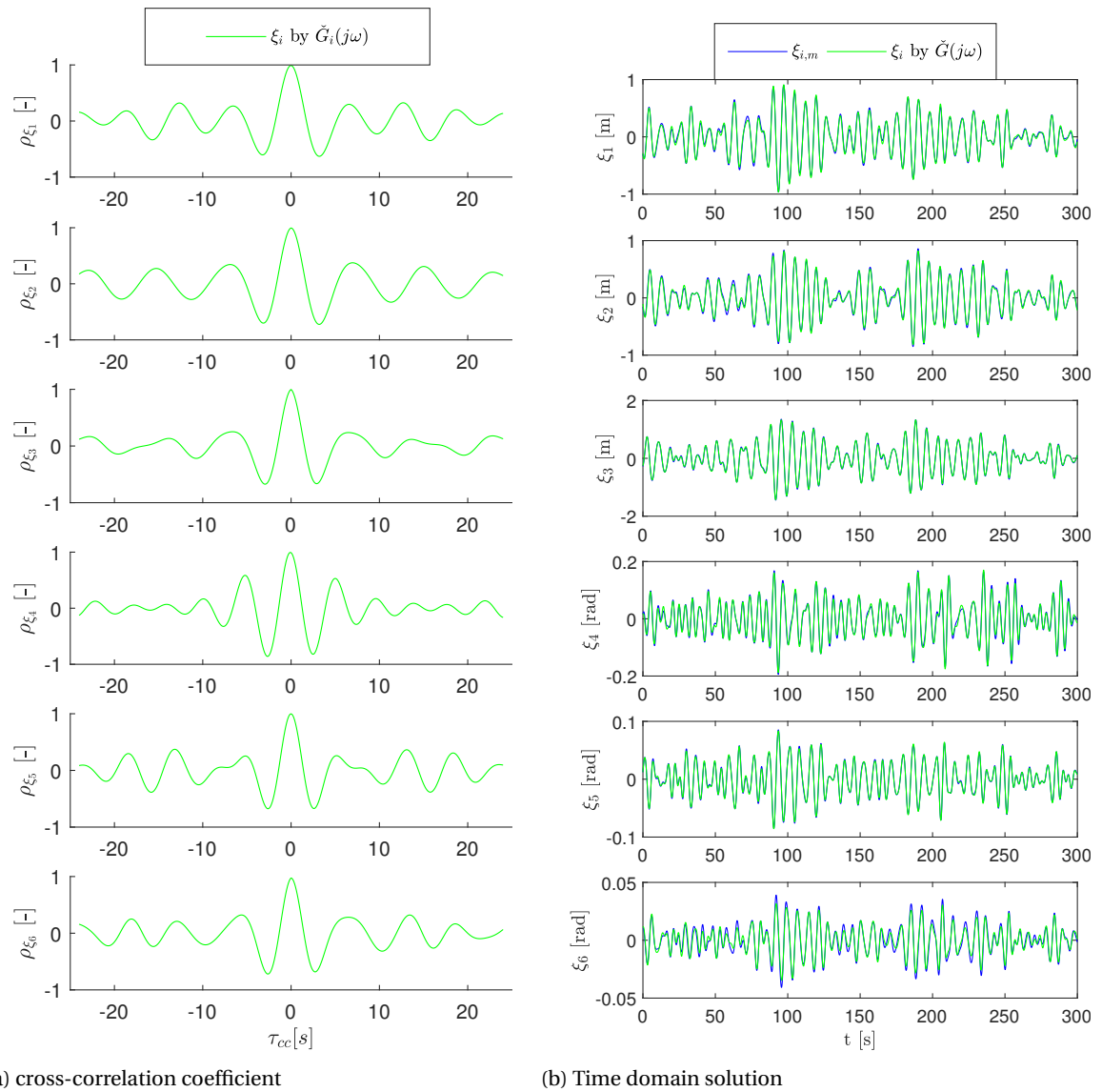


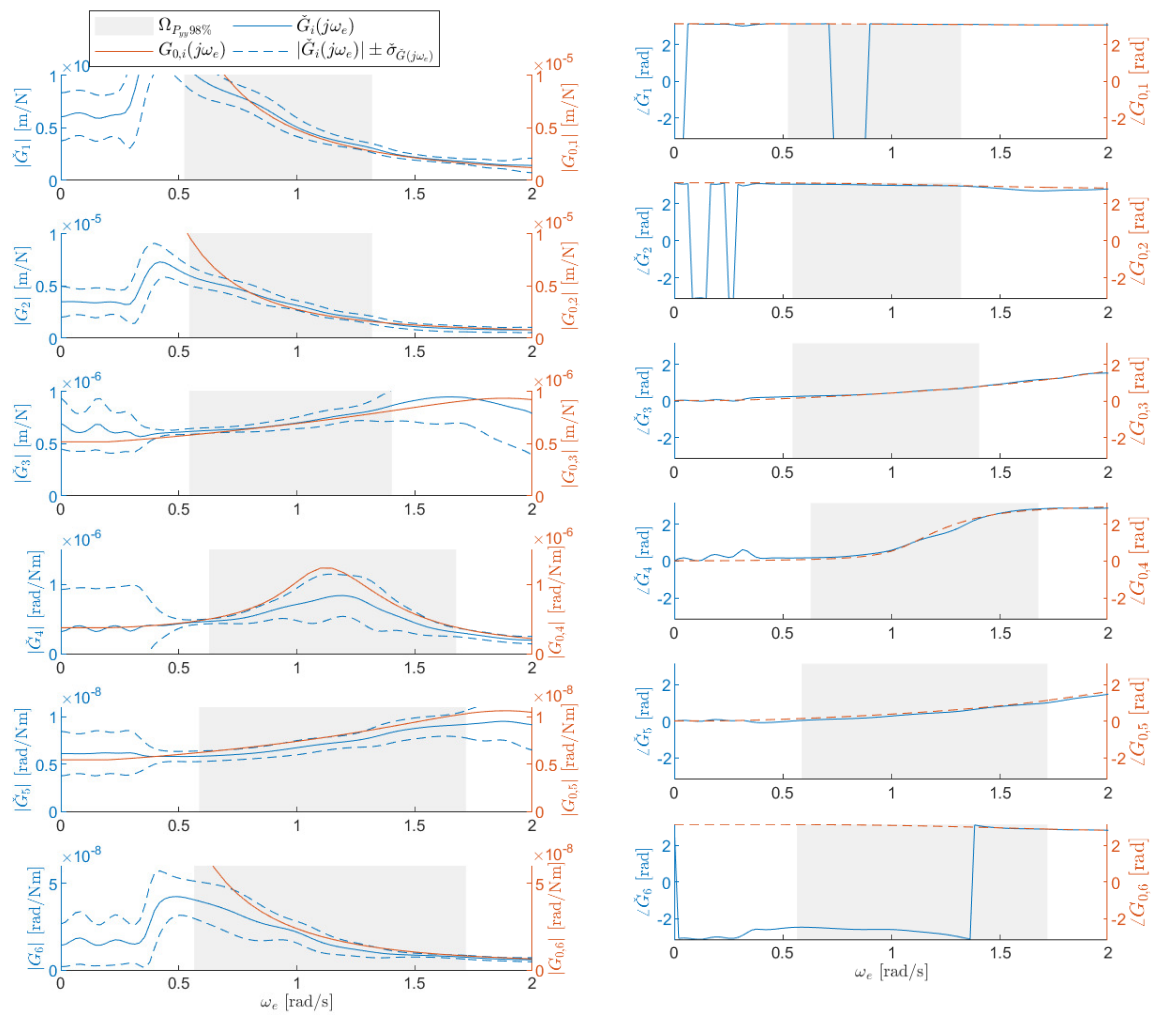
Figure 4.2: The left figure shows the cross-correlation coefficients between the measured ( $\xi_{i,m}$ ) and predicted signal ( $\xi_i$ ). In the right figure the time-domain solutions of the measured motions ( $\xi_{i,m}$ ) are shown -the blue line- as well as the predicted motions ( $\xi_i$ ) -the green line-. For the motion predictions the transfer-function has been estimated by the  $\overline{CSM}_1$  with: an Hamming window, a window-length of  $w_l = 400$  [-], and an overlap of 75%.

### Frequency-domain comparison

Figure 4.3 shows the amplitudes and phase angles of the estimated (force-to-motion) transfer-functions ( $\check{G}_i(j\omega)$ ) and pre-calculated (force-to-motion) transfer-functions ( $G_{0,i}(j\omega)$ ). In the figure: The red solid line shows the pre-calculated TF's, the blue solid line the estimated TF's, the blue dashed line represents the estimated standard deviation calculated by Equation 4.9, and the grey area represents the domain which contains 98% of the energy of the motion-response spectra ( $\omega_{P_{xx}98\%}$ ). One may notice that within the grey area the amplitudes of the pre-calculated- and estimated TF's can deviate, especially at lower frequencies and for the roll-motion.

However, as stated in Section 4.1 it is more relevant to examine the motion response-spectra ( $\check{\Phi}_{yy,i}(j\omega)$ ) rather than the differences in the TF's. Figure 4.4b shows these response-spectra for the measured motions -the solid red line- as well as the predicted motions -the solid blue line-, calculated by Equation 4.5. From the figure it can be seen that although the transfer-functions  $G_{0,i}(j\omega)$  and  $\check{G}_i(j\omega)$  deviated at the lower frequencies in most cases the response-spectra they produce are equivalent. Furthermore, it also can be seen that the largest differences in the response spectra can be found in the roll and pitch motions which is consistent with the observations from the time-domain comparisons. One possible explanation for this deviating behaviour is that in this report an uncoupled system is used while in reality ship motions are coupled. By this is meant that (for example) a motion in sway direction can also result in a additional roll motion. In Section 4.4 an extensive discussion will be held on how the currently used model can be improved by defining a coupled system.

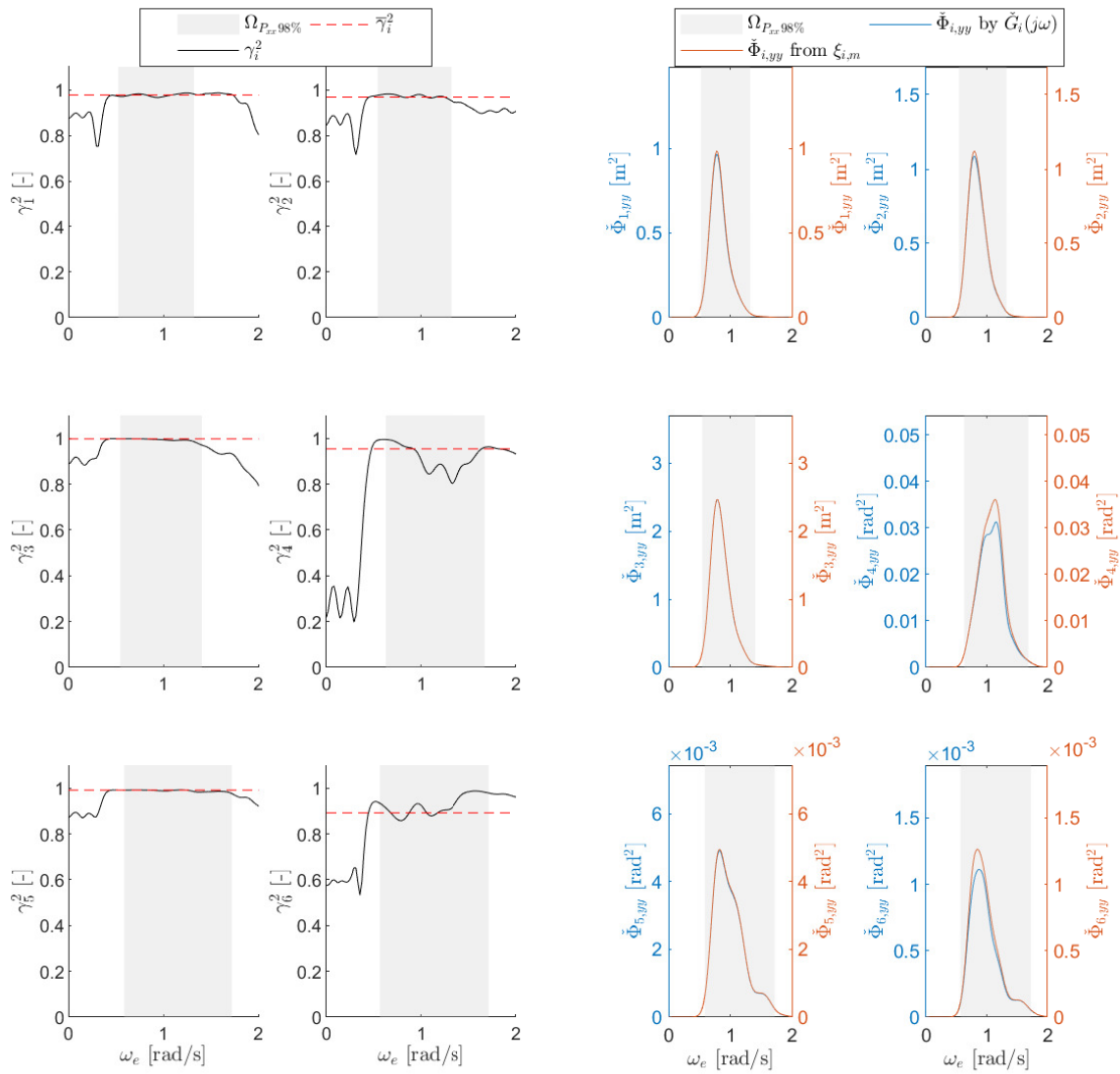
As stated in Section 3.2 and 4.1, the so called Coherence function can be used as a measure of the differences in the motion response-spectra and gives an overall assessment of the system. To recall from Section 3.2, a value of 1 means that the in- and output signal are perfectly correlated -at a certain frequency- while 0 means that there is no correlation between the signals. Figure 4.4a shows the coherence function -solid black line- as well as the mean of the coherence over the grey interval -dashed red line-. When the Coherence function is compared to the differences of the motion response-spectra, Figure 4.5, a direct relation can be found. By taking the mean value over the grey domain, a single value can be obtained which can be used to assess similarity of the motion response-spectra of the measured- and predicted motions. These single values will be used in the next section, where sea trial data is used for motion predictions.



(a) Amplitudes of the estimated- and pre-calculated TF's

(b) Phase angles of the estimated- and pre-calculated TF's

Figure 4.3: Amplitudes and phase angles of the pre-calculated TF's ( $G_{0,i}(j\omega)$ ) -solid red line- and the estimated TF's ( $\check{G}_i(j\omega)$ ) -solid blue line-.  $\check{G}_i(j\omega)$  has been estimated by the  $CSM_1$  with an Hamming window, a window-length of  $w_l = 400$  [-], and an overlap of 75%. The dashed blue line in the left figure represents the  $\check{G}_i(j\omega)$  plus or minus the variance, calculated by Equation 4.9



(a) Coherence function

(b) Motion response spectra

Figure 4.4: The coherence function (left) and the motion response spectra (right) where the solutions obtained from an estimated TF are obtained via the  $\overline{CSM}_1$  with: an Hamming window, a window-length of  $w_l = 400 [-]$ , and 75% overlap. The red dashed line in the coherence plot is the mean coherence over the interval which contains 98% of the energy of the motion response spectra.

### 4.3. Sea-trial results

In this section the data of the sea-trials conducted by Next Ocean in cooperation with Damen Shipyards will be used to evaluate if estimated TF's will increase the accuracy of real-time motion prediction. In the first part of the evaluation, Section 4.3.1, the full domain of the data records will be used to estimate the TF's. After determination those estimates will be used to (re)calculate a now-cast prediction of the motions. The estimation method used in that section is the  $\overline{CSM}_1$  with a window-length  $w_l = 400[-]$ , a sampling frequency  $f_s = 10$  [Hz], an Hamming window, and an overlap of 75%. In the second part, Section 4.3.2, variables like: the window-length and estimation method, are varied to study there influence on the results. In this section also cases will be studied where the now-cast will be changed to a forecast of  $\tau = 30$  and  $\tau = 60$  seconds, where half the record is used for training and the other half for predicting the motions of the vessel. From the results of the above mentioned analysis, in Section 4.3.3 conclusions will be drawn.

The sea trials as mentioned above where conducted on September 29<sup>th</sup> 2016, at the Northern Sea on a SPA-4207. This is a standard navy patrol vessel build by Damen Shipyards from which an example is shown in Figure 4.5. Table 4.4 summarizes some specifications of this vessel. The conditions at which the trials have been performed are summarized in Table 4.5. All the time-domain data has been generated at 10 [Hz]. As a final remark, the DOF's which will be evaluated in the upcoming sections are heave, roll and pitch.



Figure 4.5: SPA-4207

	Magnitude	Unit
Length	42	[m]
Breadth	7	[m]
Draught	2.5	[m]
Max speed	26.5	[kn]

Table 4.4: Vessel specifications

Table 4.5: Sea trial conditions

Run no.	Name	SOG [m/s]	$\mu$ [deg]	Duration [s]	$T_p$ [s]	$H_{1/3}$ [m]
1	Bow-quartering seas	0.52	161	736	7.6	2.2
2	Head seas	2.32	174	1306	7.5	2.2
3	Stern-quartering seas	4.10	307	1392	7.7	2.2
4	Following seas	2.72	346	1256	7.6	2.2
5	Bow-quartering seas	0.71	129	884	7.4	2.2
6	Beam seas	3.17	84	936	7.5	2.2

#### 4.3.1. Now-cast predictions for all runs

In this section a now-cast motions prediction by using TF's estimated by the  $\overline{CSM}_1$  ( $\check{G}_i(j\omega)$ ). These time- and frequency domain solutions will be compared to the solutions from pre-calculated TF's ( $G_{0,i}(j\omega)$  &  $H_{0,i}(j\omega)$ ), using the assessment criteria as defined in Section 4.1. In this section the figures shown correspond to run 2. The same figures for the other runs can be found in Appendix D.

In more detail, the TF's are estimated by the  $\overline{CSM}_1$  with a window-length  $w_l = 400[-]$ , a sampling frequency  $f_s = 10$  [Hz], an Hamming window, and an overlap of 75%. For the training of the TF's the full domain of the data records are used, i.e  $\Omega_t = [t_{\text{start}} \dots t_{\text{end}}]$ . After the TF's are estimated, the motions are re-calculated. The reason why for training the full data record is used is because some of the records are relatively short. This means that otherwise an insufficient amount of data would be left to make a qualitative assessment on how much the accuracy of the motion prediction increases. As already mentioned in Section 2.3 the use of "future" data for training can be justified because the transfer-function is a time independent variable.

### Time domain solutions

Figure 4.6b shows a part of the time-domain solution of the measured- and predicted motions for run 2. From visual observations it can be noticed that the predicted motions, the green and red line, are in general quite comparable to those measured, the blue line. It also can be noticed that in the case that when the estimated TF's ( $\check{G}_i(j\omega)$ ) are used, the amplitudes of the motions are lower as those calculated with the pre-calculated TF's ( $H_{0,i}(j\omega)$ ). In general, the fit between the measured and calculated motions depends on the run and DOF observed (see Appendix D). Another general observation, the best fit between the measured- and predicted motions can be found for heave and pitch and the worst fit for roll. Furthermore, it has been noticed that using  $\check{G}(j\omega)$  to calculate the motions often results in an underestimation of the amplitudes. A possible explanation for this last observation will be given in the next section, where the frequency-domain solutions are discussed.

Figure 4.6a shows the maximum cross-correlation coefficients, as function of  $\tau_{cc}$ , between the measured motions and those predicted. The green line represents the results where the motions are predicted with the estimated TF's ( $\check{G}_i(j\omega)$ ), obtained from the  $\overline{CSM}_1$ , while the red line shows the results where the motions are predicted by  $H_{0,i}(j\omega)$ . As shown in the figure, the maximum correlation-coefficients are slightly higher when a  $\check{G}_i(j\omega)$  is used. Furthermore, a maximum correlation-coefficient at  $\tau_{cc} \neq 0$  indicates that the calculated motions are lagging in time. Since for all DOF the maximum correlation coefficient  $\tau_{cc} \approx 0$ , the predicted motions barely lags with respect to the measured motions. This observation yields for the prediction where  $H_{0,i}(j\omega)$  is used as well as the prediction using  $\check{G}_i(j\omega)$ .

For the other runs, in Table 4.6 the maximum cross correlations are summarized as well as the difference in percentage. This difference has been calculated by:

$$\text{Difference \%} = \frac{\left| \rho_{H_{0,i}(j\omega)} - \rho_{\check{G}(j\omega)} \right|}{\left( \rho_{H_{0,i}(j\omega)} + \rho_{\check{G}(j\omega)} \right) / 2} \quad (4.10)$$

taking the negative sign into account when  $\rho_{H_{0,i}(j\omega)} > \rho_{\check{G}(j\omega)}$ . As shown in the table, in almost all cases the correlation-coefficient increases with  $\sim 1 - 10\%$  when estimated TF's ( $\check{G}_i(j\omega)$ ) are used. The only case where the maximum correlation-coefficient does not increase is for run 6. In the next section it will be shown that this can either come from non-linear phenomena or an erroneous predicted force signal. In Table 4.7 the lag between the measured- and predicted motions are summarized. The table shows that beside an increased correlation-coefficient also the lag is reduced when  $\check{G}_i(j\omega)$  is used.

Table 4.8 shows the ratio between the standard deviation of the calculated and measured motions, calculated by Equation 4.4. In contrast to the correlation-coefficient, much larger deviations can be found when the  $\check{G}_i(j\omega)$  is used for predicting the motions. This underestimation was already observed from the visual comparisons for which a possible explanation will be given in the next section. However, as mentioned in Section 4.1 the cross-correlation coefficient does not change when the motions are linear scaled. Therefore, the poor behaviour of this standard deviation can be artificially increased applying a linear scaling factor.

Table 4.6: Comparisons between the maximum cross-correlation coefficient of the measured ( $\xi_{i,m}$ ) and calculated ( $\xi_i$ ) motion signals. The calculated motions are obtained with the use of the pre-calculated ( $H_{0,i}(j\omega)$ ) or estimated ( $\check{G}_i(j\omega)$ ) TF's. Here  $\check{G}_i(j\omega)$  has been estimated with:  $\overline{CSM}_1$ ,  $w_l = 400[-]$ , an Hamming window, and an overlap op 75%

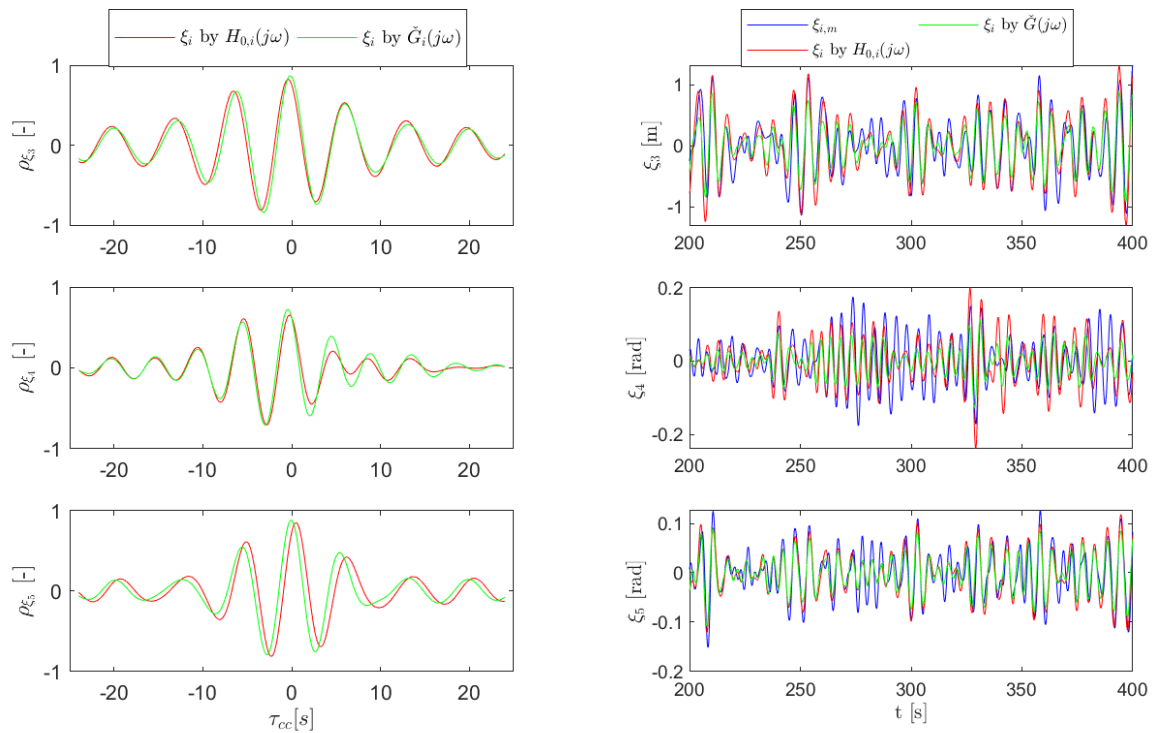
Run	$H_{0,i}(j\omega)$			$\check{G}(j\omega)$			Difference [%]		
	Heave	Roll	Pitch	Heave	Roll	Pitch	Heave	Roll	Pitch
	$\rho_{\xi_3}$	$\rho_{\xi_4}$	$\rho_{\xi_5}$	$\rho_{\xi_3}$	$\rho_{\xi_4}$	$\rho_{\xi_5}$	$\rho_{\xi_3}$	$\rho_{\xi_4}$	$\rho_{\xi_5}$
1	0.83	0.53	0.84	0.87	0.59	0.85	2.36	5.09	1.02
2	0.82	0.65	0.85	0.87	0.72	0.88	2.69	6.09	1.86
3	0.73	0.61	0.74	0.84	0.72	0.79	7.05	9.55	3.23
4	0.74	0.32	0.75	0.80	0.38	0.79	3.37	5.52	2.72
5	0.80	0.61	0.78	0.84	0.65	0.82	2.74	3.49	2.19
6	0.71	0.71	0.41	0.76	0.67	0.39	3.32	-3.69	-1.39

Table 4.7: Summary of lag in seconds between the predicted and calculated motions, in seconds. The calculated motions are obtained with the use of the pre-calculated ( $H_{0,i}(j\omega)$ ) or estimated ( $\check{G}_i(j\omega)$ ) TF's. Here  $\check{G}_i(j\omega)$  has been estimated with:  $\overline{CSM}_1$ ,  $w_l = 400[-]$ , an Hamming window, and an overlap op 75%

Run	$H_{0,i}(j\omega)$			$\check{G}(j\omega)$		
	Heave	Roll	Pitch	Heave	Roll	Pitch
	lag <sub>3</sub>	lag <sub>4</sub>	lag <sub>5</sub>	lag <sub>3</sub>	lag <sub>4</sub>	lag <sub>5</sub>
1	-0.1	0.4	0.4	0	0	0
2	-0.4	-0.3	0.5	-0.2	-0.4	-0.1
3	0.4	0.2	0.7	0	0	0
4	1.5	1.4	1.5	-0.1	-0.1	0
5	-1.1	0.3	-0.1	0	-0.1	0
6	-2.2	-2.0	-1.9	0.4	0.3	-0.2

Table 4.8: Ratio of standard deviations between the calculated- and measured motions. The calculated motions are obtained with the use of the pre-calculated ( $H_{0,i}(j\omega)$ ) or estimated ( $\check{G}_i(j\omega)$ ) TF's. Here  $\check{G}_i(j\omega)$  has been estimated with:  $\overline{CSM}_1$ ,  $w_l = 400[-]$ , an Hamming window, and an overlap op 75%

Run	$H_{0,i}(j\omega)$			$\check{G}(j\omega)$		
	Heave	Roll	Pitch	Heave	Roll	Pitch
	$\sigma_{3,d}$	$\sigma_{4,d}$	$\sigma_{5,d}$	$\sigma_{3,d}$	$\sigma_{4,d}$	$\sigma_{5,d}$
1	0.97	0.90	1.00	0.86	0.49	0.89
2	1.05	1.06	0.95	0.71	0.62	0.74
3	1.10	1.22	1.05	0.86	0.70	0.81
4	1.01	1.34	1.00	0.79	0.35	0.75
5	0.97	1.11	1.01	0.84	0.67	0.81
6	1.01	1.53	1.20	0.85	0.62	0.46



(a) Cross-correlation coefficient

(b) Time domain solution

Figure 4.6: Run 2: The left figure shows the cross-correlation coefficients between the measured- and predicted motions for. In the right figure the time-domain solutions of the measured motions are shown by the blue line. The green lines in both figures represents that the motions are predicted by using estimated TF's while the red lines show the solutions of the pre-calculated TF's. Furthermore,  $\tilde{G}_i(j\omega)$  has been estimated by the  $\overline{CSM}_1$  with: an Hamming window, a window-length of  $w_l = 400$  [-], and an overlap of 75%.

### Frequency domain solutions

Figure 4.7 shows the amplitudes and phase angles of the TF's estimated by the  $\overline{CSM}_1$  ( $\check{G}_i(j\omega)$ ) method and the pre-calculated TF's ( $G_{0,i}(j\omega)$ ) for run 2. The grey-shaded areas represents the domain which contains 98% of the energy of the motion response-spectrum, which will be referred to as  $\Omega_{P_{xx}98\%}$ . As shown in the figure, the order of magnitude between the pre-calculated TF's ( $G_{0,i}(j\omega)$ ) and the estimated TF's ( $\check{G}_i(j\omega)$ ) is significantly different. This difference comes from the fact that the amplitudes of the wave-components obtained from the "raw" radar data are un-scaled [14].

Furthermore, one may also notice from the figure that the pre-calculated TF's (red-solid) and the estimated TF's (solid-blue) are showing some deviations. The reason for these deviations can be found in a number of reasons like: the uncertainty in loading conditions, noise, errors in the wave-field predictions, and other reasons which will be discussed in the upcoming paragraphs. One single cause for the deviations can thus not be given. However, as shown during the synthetic analysis in Section 4.2 a deviation between the estimated- and pre-calculated transfer-functions does not directly results in a bad prediction.

Figure 4.8a shows the motion response-spectra of the of the measured- and calculated motions. To recall, these response-spectra are directly estimated by Equation 4.5 from the measured- and predicted time-domain signals ( $\xi_{i,m}(t)$  &  $\xi_i(t)$ ). The dashed-blue line shows the response-spectra of the motions calculated by the pre-calculated TF's ( $H_{0,i}(j\omega)$ ) and the solid blue line shows the results for the estimated TF's ( $\check{G}_i(j\omega)$ ). As illustrated in the figure, the motion response-spectra based on estimated TF's has a better agreement with the response-spectra of the measured motions compared to the spectra obtained from pre-calculated TF's. The above made observations does not only hold for run 2 but also for the other runs, except run 6 (see Appendix D).

The deviations between the response-spectra of the measured- and predicted motions can be found in several reasons. The first reason, an insufficient amount of resolved wave-components. In (for example) run 4 the wave-components are resolved till  $\omega_e \approx 1$  while the motion response spectra shows an additional peak at  $\omega_e \approx 1.25$ , due to the natural frequency (See Appendix D Figure D.12a). Since these frequency components are not resolved by the radar-data analysis, the motions at those frequencies will not be modeled.

As a second reason, the system used in this research does not take coupling effects between the motions into account. As already discussed in Section 4.2, in reality ship motions are coupled which means that a displacement in one direction also causes a displacement in another direction. In Section 4.4 an extensive discussion will be held on how the currently used model can be improved by defining a coupled system.

A third reason, uncorrelated signals/ non-linear phenomena. For the estimated TF's ( $\check{G}_i(j\omega)$ ) the correlation between the signals also plays an important roll. By this is meant, if the excitation force is uncorrelated to the motion (at a certain frequency) the estimated TF's will tend towards zero<sup>1</sup> ( $\check{\Phi}_{i,yx} \rightarrow 0$ ). One of the sources for signals/ frequencies to be uncorrelated is due to non-linear phenomena. When (for example) the response-spectra of the roll motion of run 3 is observed (See Appendix D Figure D.9a), it can be seen that near the natural frequency ( $\omega_e \approx 1.25$ ) the estimated TF ( $\check{G}_4(j\omega)$ ) tends toward zero, while the wave-components are resolved near that frequency. From a physical point of view this makes sense since large motions and/ or high velocities will make the system/ ship motions less linear, especially for the roll motion.

As a final remark for the differences in the response-spectra, the measured and calculated motion response-spectra for the heave motion in some cases have the same shape/ solution (See for example: D.9a & D.12a). This observation holds for the calculated response-spectra obtained using pre-calculated TF's ( $H_{0,i}(j\omega)$ ) as well as the spectra obtained from the estimated TF's ( $\check{G}_i(j\omega)$ ). The reason why especially the heave motion is of interest, is because it is the most linear motion which can be observed. This means that the (on linear theory based) calculated response-spectra should be the most comparable. Due to the similarity in these response spectra, it is quite assumable that during those runs the wave-components are well resolved and more importantly, the force can be used as a reliable input. Under the assumption that these (linear) forces can be taken as a reliable input, in future work other models can be defined where the non-linear response of the

<sup>1</sup>A brief explanation: When  $\check{\Phi}_{i,yx}$  is estimated (used for the estimation of the TF in the  $\overline{CSM}_1$ , see Section 3.1.2) the full length of the signal is divided into blocks and averaged. When the amplitude and phase angles in each block are different, on average the solution will tend to zero.

ship motions is taken into account. Defining a non-linear model may eventually result in even more accurate motion predictions. However, since the similarity among the response-spectra does not hold for every run, also a study will be recommended with the aim to assess the quality of the predicted force signal.

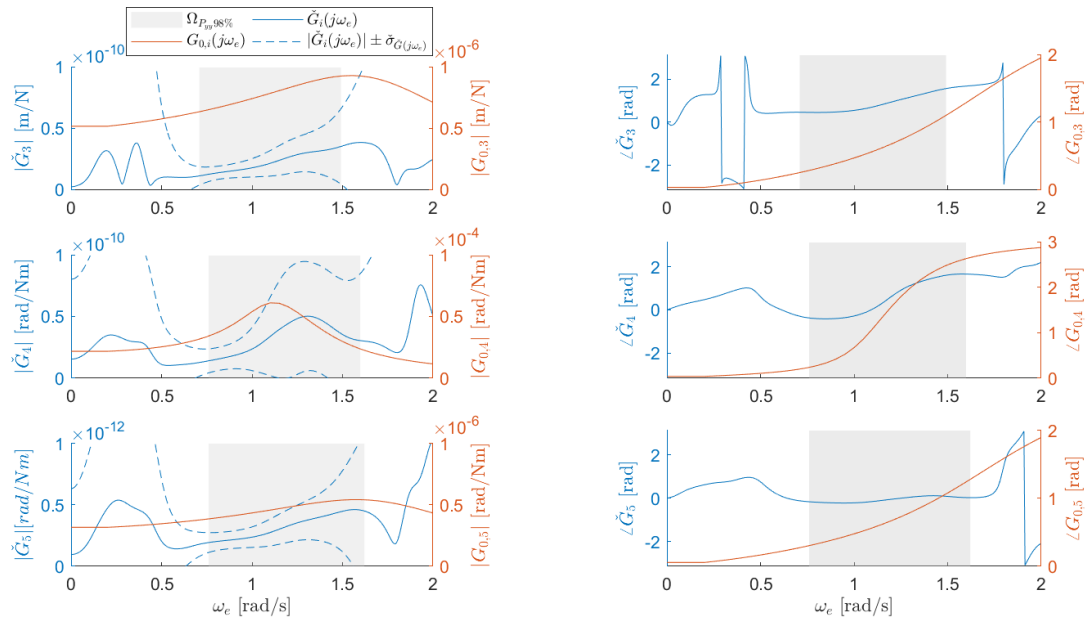
As already shown during the synthetic evaluation in Section 4.2, a direct relation of the difference between the calculated and predicted motion response-spectra (based on  $\tilde{G}_i(j\omega)$ ) can be found in the Coherence function. For run 2 this function is illustrated in Figure 4.8b. The red-dashed line in the figure represents the mean coherence over the domain  $\Omega_{P_{xx}98\%}$ . One may observe from the figure that in general the highest Coherence can be found at the lowest frequencies, within  $\Omega_{P_{xx}98\%}$ , and decays with an increasing frequency. Furthermore, when the different DOF's are compared shows that the coherence for the roll motion is significantly lower than those of the heave- and pitch motion. As already discussed above, due to non-linear phenomena the in- and output signals become less correlated which results in  $\check{\Phi}_{i,yx} \rightarrow 0$ . Since roll is the most non-linear motion which can be observed, also from a physical point of view it makes sense.

Table 4.9 summarizes the mean coherence function over the domain  $\Omega_{P_{xx}98\%}$  for all the runs. Comparing these results to the correlation-coefficients from Table 4.6 shows a strong similarity. By this is meant that a low correlation also results in a low coherence and vice versa.

In the previous section it was shown the correlation-coefficient only decreases for run 6. Two possible explanations for this are: an inaccurate predicted force signal or strongly non-linear behaviour. As shown in Table 4.9, the mean coherence of run 6 is in general low compared to the other runs. As already discussed above, a low coherence means that the in- and output signals are not well correlated. One of the reasons why signals are uncorrelated can be found in the non-linear response of the ship (output signal). If the system is strongly non-linear, the linear approximation will no longer hold and will thus result in poor prediction of the motions. However, one should also bear in mind that also the force (input signal) can contribute to the uncorrelated behaviour. This can occur when the solutions of each block ( $X^m(j\omega)$ ) varies from one realization to another, with respect to the solutions of the input signal ( $Y^m(j\omega)$ ). Because the coherence for heave (the most linear motion which can be observed) in run 6 is relatively low compared to the other runs, one may also say the force is inaccurately predicted.

Table 4.9: Mean coherence over the domain  $\Omega_{P_{xx}98\%}$

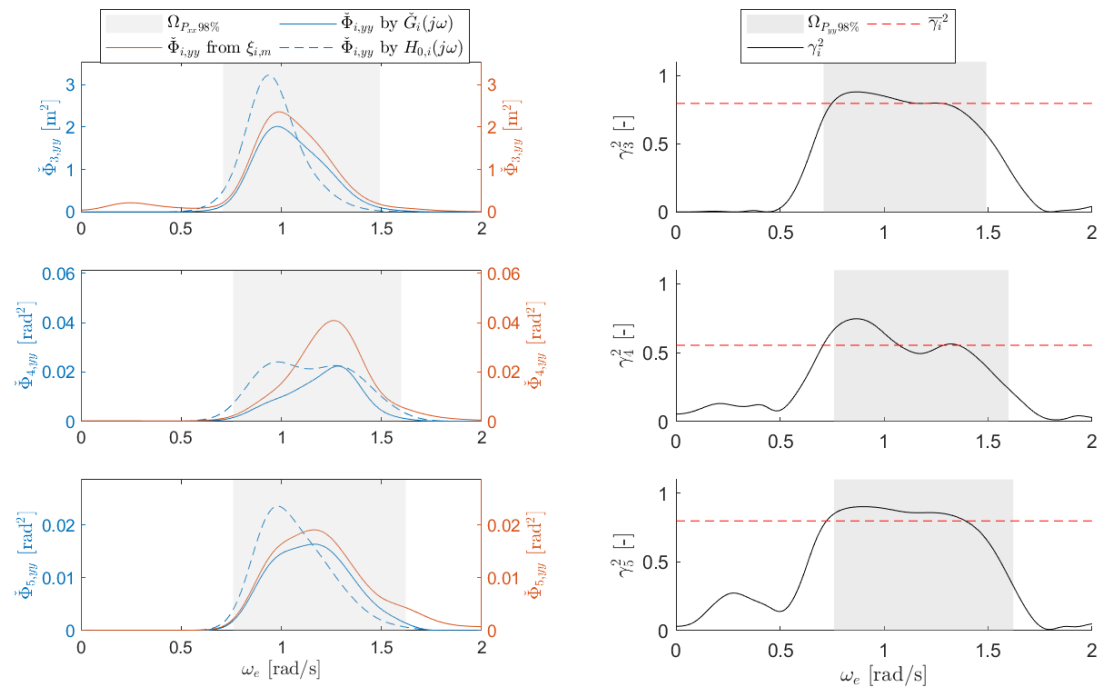
Run	$\bar{\gamma}_3^2$	$\bar{\gamma}_4^2$	$\bar{\gamma}_5^2$
1	0.78	0.49	0.81
2	0.79	0.55	0.79
3	0.72	0.56	0.65
4	0.63	0.38	0.63
5	0.74	0.59	0.72
6	0.48	0.33	0.26



(a) Amplitudes of the TF

(b) Phase angles of the TF

Figure 4.7: Run 2: The amplitudes and phase angles for of the pre-calculated TF's (solid red) and estimated TF's (solid blue). The blue dashed line represents the estimated TF plus or minus the estimated standard deviation. The grey area represents the domain which contains 98% of the energy of the motion response-spectra.  $\tilde{G}_i(j\omega)$  has been estimated by  $CSM_1$  with: an Hamming window, a window-length of  $w_l = 400$  [-], and an overlap of 75%.



(a) Motion response-spectra

(b) Coherence function

Figure 4.8: Run 2: The motion response-spectra (left) and the Coherence function (right). The blue dashed line in the left figure represents the motion response-spectra of the predicted motions obtained from pre-calculated TF's. The solid blue line shows the motion response-spectra in the case that estimated TF's are used. In the right figure, the red-dashed line is the mean coherence of the grey domain.  $\tilde{G}_i(j\omega)$  has been estimated by  $CSM_1$  with: an Hamming window, a window-length of  $w_l = 400$  [-], and an overlap of 75%.

### 4.3.2. Case studies

In the previous section a now-cast prediction was made for all the runs, based on pre-calculated TF's and TF's estimated by  $\overline{CSM}_1$ . In this section some of the variables will be changed to gain confidence that the obtained solutions is the best one may get, by the methods as discussed in this report. The cases which will be studied are:

- A comparison between the  $\overline{CSM}_1$  and  $\overline{CSM}_2$
- A comparison between the  $\overline{CSM}_1$ ,  $\overline{ETFE}$  and  $\overline{ETFE}$
- Varying the window length
- Time evaluation for transfer-function estimation
- Predicting motions for  $\tau = 30$  and  $\tau = 60$  [s], rather than reconstructing in the previous sections.

Unless denoted otherwise: Run 2 has been used for evaluations, where the full data record is used for training. For the averaged results ( $\overline{ETFE}$  and  $\overline{CSM}$ ), the following settings have been used: an Hamming window,  $w_l = 400$  [-], and 75% overlap.

#### Comparison between $\overline{CSM}_1$ and $\overline{CSM}_2$

In Section 3.1.2 and 3.4 it was stated that for the  $\overline{CSM}$  a bias error can arise due to the presence of noise in the input and/or output signal [21]. Depending on where the largest noise source can be found, either the  $\overline{CSM}_1$  or  $\overline{CSM}_2$  is recommended. Figure 4.9 shows the difference in estimation of the TF's for each method. The figures shows that bot estimates are different, especially at the higher frequencies. To assess which method should be used, Table 4.10 shows the maximum cross-correlation coefficients and Table 4.11 shows the standard deviations.

The results in the Table 4.10 show that in general the highest cross-correlation is obtained using the  $\overline{CSM}_1$  method. When the relative standard deviations between the calculated and measured motions are compared, Table 4.11 shows that the  $\overline{CSM}_2$  method tends to overestimate the amplitudes while the  $\overline{CSM}_1$  tends to underestimate the motion amplitudes. However, as already mentioned in one of the previous section "poor" standard deviations can be resolved without affecting the correlation coefficient, by applying a linear scaling factor to the calculated motions. Therefore, high correlations are preferred above high standard deviations which makes the  $\overline{CSM}_1$  more appealing for practical use.

Comparing these results to the results from Section 3.4 and the corresponding theory given in Section 3.1.2, these answers are also what one may expect. This because, the non-linear behaviour of the ship its measured motions will cause "noise" in the output signal which is higher than the noise of the linear modeled input signal, i.e. forces. In other words, due to the higher SNR at the output signal an higher bias error is expected when  $\overline{CSM}_2$  is used and therefore the  $\overline{CSM}_1$  will give a better approximation of the TF.

Table 4.10: Comparison of the maximum correlation coefficients between the  $\overline{CSM}_1$  and  $\overline{CSM}_2$ . For the estimations in both cases: an Hamming window,  $w_l = 400$  [-], and 75% overlap.

Run	Name	$\overline{CSM}_1$			$\overline{CSM}_2$		
		$\rho_{\xi_3}$	$\rho_{\xi_4}$	$\rho_{\xi_5}$	$\rho_{\xi_3}$	$\rho_{\xi_4}$	$\rho_{\xi_5}$
2	Head seas	0.86	0.72	0.88	0.85	0.72	0.87
3	Stern-quartering seas	0.83	0.72	0.79	0.82	0.67	0.77
4	Following seas	0.79	0.38	0.79	0.75	0.35	0.71
5	Bow-quartering seas	0.84	0.65	0.82	0.73	0.53	0.80
6	Beam-seas	0.76	0.67	0.39	0.74	0.66	0.40

Table 4.11: Summary of the Ratio of standard deviations obtained by the  $\overline{CSM}_1$  and  $\overline{CSM}_2$ . For the estimations in both cases: an Hamming window,  $w_l = 400$  [-], and 75% overlap.

Run	$\overline{CSM}_1$			$\overline{CSM}_2$		
	$\sigma_{\xi_{3,d}}$	$\sigma_{\xi_{4,d}}$	$\sigma_{\xi_{5,d}}$	$\sigma_{\xi_{3,d}}$	$\sigma_{\xi_{4,d}}$	$\sigma_{\xi_{5,d}}$
2	0.71	0.62	0.74	0.85	1.12	0.84
3	0.86	0.71	0.81	1.08	1.35	1.20
4	0.79	0.35	0.75	1.14	0.79	1.22
5	0.84	0.67	0.81	1.33	1.77	1.09
6	0.86	0.62	0.46	1.79	4.43	2.35

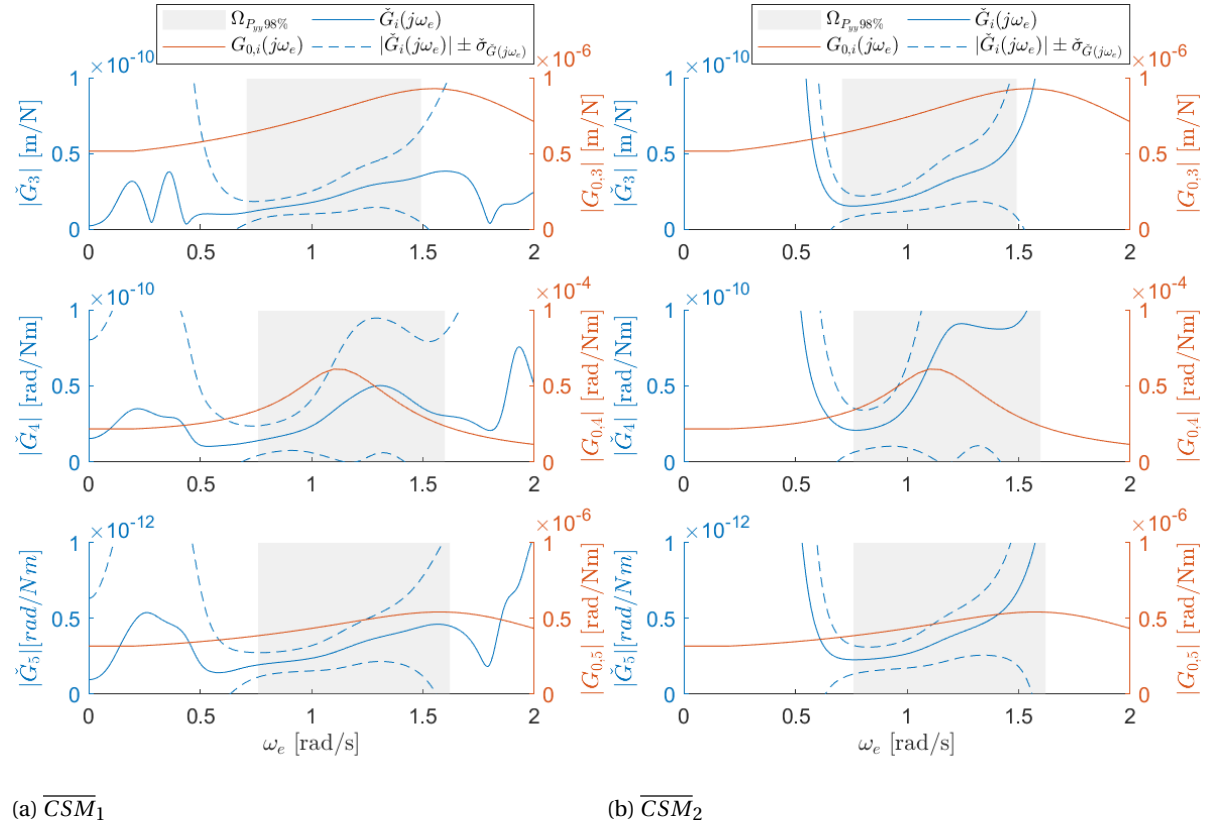


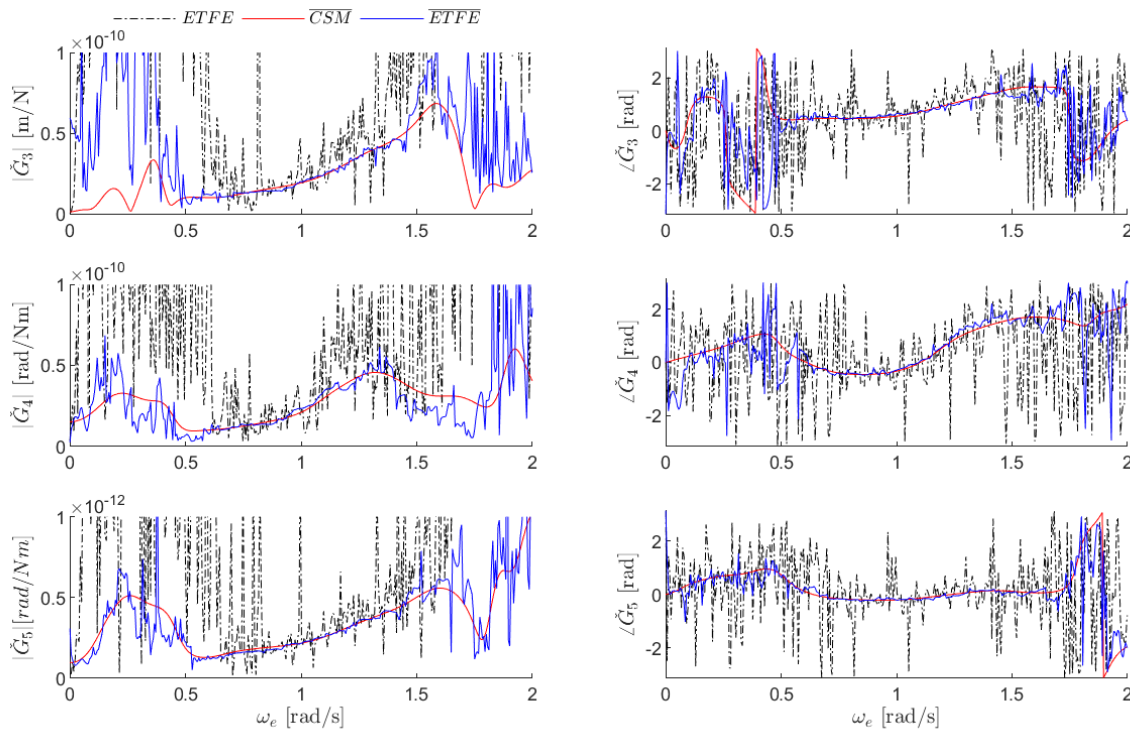
Figure 4.9: The amplitudes of the estimated TF's ( $\check{G}(j\omega)$ ) and the pre-calculated TF's ( $G_{0,i}(j\omega)$ ), for run 3. The left figure shows the results of the estimated TF's by  $\overline{CSM}_1$  and the right figure shows the results of  $\overline{CSM}_2$ . For the estimations in both cases: an Hamming window,  $w_l = 400$  [-], and 75% overlap.

Comparison between estimation methods

Table 4.12 shows the correlation-coefficients for the three different methods. The results in the table clearly show that -Welch- averaging will improve the result. This can be explained by the fact that averaging will reduce the variance of the estimated TF. Comparing the correlation-coefficients obtained from the  $\overline{ETFE}$  to the results of the  $\overline{CSM}_1$  method shows equivalent results. However, when the transfer-functions estimates are visually compared, as is illustrated in Figure 4.10, shows that the  $\overline{CSM}_1$  provides a smoother solution as the ETFE. Therefore, it is recommended to use the  $\overline{CSM}_1$

Table 4.12: Summary of cross-correlation coefficients (of run 2) obtained by the ETFE,  $\overline{CSM}_1$ , and  $\overline{ETFE}$ . For the averaged results: an Hamming window,  $w_l = 400$  [-], and 75% overlap,

Method	Heave	Roll	Pitch
	$\rho_{\xi_3}$	$\rho_{\xi_4}$	$\rho_{\xi_5}$
$\overline{CSM}_1$	0.85	0.72	0.87
$\overline{ETFE}$	0.85	0.72	0.87
ETFE	0.22	0.39	0.53



(a) Amplitudes of the transfer function

(b) Phase angles of the transfer function

Figure 4.10: Comparison between TF estimation methods for run 2. The solid blue line represents the TF estimation by the  $\overline{ETFE}$  method, the solid red represents the TF estimation by the  $\overline{CSM}_1$  method, and the black dashed line represents the TF estimation by the ETFE method. For the averaged results: an Hamming window,  $w_l = 400$  [-], and 75% overlap,

### Change in window length

Table 4.13 shows the correlation coefficients for an increasing window length, obtained using the TF's estimated by the  $\overline{CSM}_1$  method. The results clearly show that for all DOF the cross-correlation asymptotically increases and that a length of 400 samples seems sufficient. However, it should be noticed that the full domain of the record has been used for training the TF's, i.e.  $\Omega_t = [t_{start} \dots t_{end}]$ . This means that even for large windows, enough averages can be made to reduce the variance. An evaluation of both window-length and the total available time for training will be left for future studies.

Table 4.13: Maximum cross-correlation coefficients for an increasing window-length ( $w_l$ ), run 2. The TF's used to calculate the motions are estimated by  $\overline{CSM}_1$  with: an Hamming window and an overlap of 75%.

$w_l$ [-]	Heave	Roll	Pitch
	$\rho_{\xi_3}$	$\rho_{\xi_4}$	$\rho_{\xi_5}$
100	0.82	0.61	0.85
200	0.84	0.68	0.86
400	0.87	0.72	0.87
1000	0.87	0.72	0.87
2000	0.87	0.72	0.87

### Training time for the TF

Table 4.14 shows for an increasing training time the maximum cross-correlation coefficients, for the runs 2-4. For the motion predictions the estimated TF's are estimated by the  $\overline{CSM}_1$  method. The results in the table shown that within 2 minutes already high correlation factors can be found for all runs. However, it is recommended to use at least 5 till 7 minutes of data for the solution to converge. As an indication, the total number of blocks used for averaging are also shown in the table.

Table 4.14: Maximum cross-correlation coefficients for an increasing training time -run 2 till 4-. The TF's used to calculate the motions are estimated by  $\overline{CSM}_1$  with:  $w_l = 400$ [-], an Hamming window, and an overlap of 75%.

training time [s]	No. Blocks (M)	Run 2			Run 3			Run 4		
		Heave	Roll	Pitch	Heave	Roll	Pitch	Heave	Roll	Pitch
		$\rho_{\xi_3}$	$\rho_{\xi_4}$	$\rho_{\xi_5}$	$\rho_{\xi_3}$	$\rho_{\xi_4}$	$\rho_{\xi_5}$	$\rho_{\xi_3}$	$\rho_{\xi_4}$	$\rho_{\xi_5}$
120	8	0.86	0.73	0.87	0.84	0.69	0.78	0.78	0.38	0.77
180	14	0.86	0.74	0.86	0.84	0.71	0.79	0.78	0.38	0.78
240	20	0.85	0.74	0.86	0.84	0.71	0.78	0.78	0.37	0.77
300	26	0.86	0.72	0.87	0.84	0.71	0.78	0.79	0.37	0.77
360	32	0.86	0.72	0.87	0.84	0.72	0.79	0.79	0.38	0.78
420	38	0.86	0.72	0.87	0.84	0.72	0.79	0.79	0.38	0.78

### Motion prediction

In this sub-section one half of the data records are used for training TF's, i.e.  $\Omega_t = [t_{start} \dots t_{end}/2]$ . The other half of the data records is used to make a prediction of  $\tau = 0$ ,  $\tau = 30$  and  $\tau = 60$  seconds ahead. For the estimation of the TF's the  $\overline{CSM}_1$  method has been used with: an Hamming window, a window-length of  $w_l = 400$  [-], and an overlap of 75%.

Table 4.15 till 4.17 shows the correlation-coefficients for an increasing prediction horizon  $\tau$ . Comparing the results in the tables shows that with an increasing  $\tau$  the cross-correlation between the measured and predicted motions mildly decreases, independent of the method used to calculate the motions. More importantly, in all the cases the motions predicted by the estimated TF's ( $\check{G}_i(j\omega)$ ) outperform the predictions where the pre-calculated TF's ( $H_{0,i}(j\omega)$ ) are used. This observation contributes again to the statement that TF estimated by measurements will increase the accuracy of real-time motion prediction.

Table 4.15:  $\tau = 0$ [s]: Comparisons between the maximum cross-correlation coefficients of the measured ( $\xi_{i,m}$ ) and calculated ( $\xi_i$ ) motion signals. The calculated motions are obtained with the use of the pre-calculated ( $H_{0,i}(j\omega)$ ) or estimated ( $\check{G}_i(j\omega)$ ) TF's. Here  $\check{G}_i(j\omega)$  has been estimated with:  $\overline{CSM}_1$ ,  $w_l = 400$ [-], an Hamming window, and an overlap op 75%

Run	$H_{0,i}(j\omega)$			$\check{G}(j\omega)$			Difference [%]		
	Heave	Roll	Pitch	Heave	Roll	Pitch	Heave	Roll	Pitch
	$\rho_{\xi_3}$	$\rho_{\xi_4}$	$\rho_{\xi_5}$	$\rho_{\xi_3}$	$\rho_{\xi_4}$	$\rho_{\xi_5}$	$\rho_{\xi_3}$	$\rho_{\xi_4}$	$\rho_{\xi_5}$
2	0.84	0.67	0.85	0.88	0.74	0.87	2.27	6.26	1.07
3	0.76	0.56	0.71	0.88	0.70	0.77	7.51	12.40	3.68
4	0.70	0.30	0.76	0.77	0.37	0.76	4.31	6.05	0.52

Table 4.16:  $\tau = 30$ [s]: Comparisons between the maximum cross-correlation coefficient of the measured ( $\xi_{i,m}$ ) and calculated ( $\xi_i$ ) motion signals. The calculated motions are obtained with the use of the pre-calculated ( $H_{0,i}(j\omega)$ ) or estimated ( $\check{G}_i(j\omega)$ ) TF's. Here  $\check{G}_i(j\omega)$  has been estimated with:  $\overline{CSM}_1$ ,  $w_l = 400$ [-], an Hamming window, and an overlap op 75%

Run	$H_{0,i}(j\omega)$			$\check{G}(j\omega)$			Difference [%]		
	Heave	Roll	Pitch	Heave	Roll	Pitch	Heave	Roll	Pitch
	$\rho_{\xi_3}$	$\rho_{\xi_4}$	$\rho_{\xi_5}$	$\rho_{\xi_3}$	$\rho_{\xi_4}$	$\rho_{\xi_5}$	$\rho_{\xi_3}$	$\rho_{\xi_4}$	$\rho_{\xi_5}$
2	0.83	0.66	0.84	0.87	0.73	0.86	2.36	7.09	1.09
3	0.76	0.57	0.713	0.88	0.71	0.77	7.30	12.41	3.78
4	0.68	0.29	0.74	0.75	0.36	0.75	4.63	6.10	0.36

Table 4.17:  $\tau = 60$ [s]: Comparisons between the maximum cross-correlation coefficient of the measured ( $\xi_{i,m}$ ) and calculated ( $\xi_i$ ) motion signals. The calculated motions are obtained with the use of the pre-calculated ( $H_{0,i}(j\omega)$ ) or estimated ( $\check{G}_i(j\omega)$ ) TF's. Here  $\check{G}_i(j\omega)$  has been estimated with:  $\overline{CSM}_1$ ,  $w_l = 400$ [-], an Hamming window, and an overlap op 75%

Run	$H_{0,i}(j\omega)$			$\check{G}(j\omega)$			Difference [%]		
	Heave	Roll	Pitch	Heave	Roll	Pitch	Heave	Roll	Pitch
	$\rho_{\xi_3}$	$\rho_{\xi_4}$	$\rho_{\xi_5}$	$\rho_{\xi_3}$	$\rho_{\xi_4}$	$\rho_{\xi_5}$	$\rho_{\xi_3}$	$\rho_{\xi_4}$	$\rho_{\xi_5}$
2	0.82	0.65	0.83	0.86	0.73	0.85	2.38	7.41	0.80
3	0.74	0.58	0.70	0.86	0.73	0.76	7.31	13.83	4.17
4	0.67	0.28	0.74	0.74	0.36	0.74	4.74	7.77	0.11

### 4.3.3. Summary and conclusions sea trial analysis

In Section 4.3.1 a now-cast prediction of the ship motions was made based on TF's estimated by the  $\overline{CSM}_1$  method, where the full length of the data set was used for training. It is shown that these estimated TF's ( $\check{G}_i(j\omega)$ ) will result in an increase of the cross-correlation coefficient of  $\sim 1 - 10\%$ , compared to the results where pre-calculated TF's ( $H_{0,i}(j\omega)$ ) are used. Although the cross-correlation increases, the ratio of standard deviations between the calculated and measured motion is lower when estimated TF's are used. Therefore, an additional scaling factor is required to compensate for this. From the frequency-domain solutions it is shown that the estimated TF's ( $\check{G}_i(j\omega)$ ) are different compared to those pre-calculated ( $G_{0,i}(j\omega)$ ). However, by comparing the motion response-spectra it is shown that those obtained by using estimated TF's ( $\check{G}_i(j\omega)$ ) have a better relation to the response-spectra of the measured motions compared to the solutions obtained from pre-calculated TF's ( $G_{0,i}(j\omega)$ ).

In Section 4.3.2 different cases were studied. It is shown that the best and most smooth results are obtained from the  $\overline{CSM}_1$  method. It also is shown that with a window-length of 400 samples, within  $\sim 5 - 7$  minutes the solution has converged. And finally, for an increasing prediction horizon ( $\tau$ ) the cross-correlation using estimated TF's always outperforms the solutions from pre-calculated TF's.

With the above said, it is safe to conclude the use of estimated TF's by the  $\overline{CSM}_1$  method will increase the accuracy of real-time ship motion predictions with  $\sim 1 - 10\%$ .

## 4.4. Discussion

In this section two topics will be discussed. First, the system which is concerned in this report is a Single Input Single Output system while in reality the motions are coupled. Therefore, in Section 4.4.1 an alternative method will briefly be discussed on how to improve the accuracy of real-time motion predictions further using a coupled motion system. Secondly, an alternative method for averaging the ETFE will be presented.

### 4.4.1. A coupled system

As mentioned in Section 2.2.2 and 3.1, the system concerned in this thesis is a Single Input Single Output system (SISO). However, in reality ship motions are coupled which results in a Multiple Input Single Output system (MISO). By this is meant that (for example) a heave motion will also generate a pitch motion and vice versa. As already discussed in Section 2.2.2, taking the coupling terms into account results in one equation with two (or multiple) unknowns which cannot be solved straight away. However, in the upcoming sub-sections a method will be briefly discussed which resolves this problem. In more detail, the coupling between the heave- and pitch motion will be made while the couplings of the other DOF's will be left for future studies. The method which will be shown is basically an extension of the  $\overline{CSM}_1$  and comparable to the method used by Alford et. al [1].

#### Governing motion equations

Lets first assume that the total pitch motion is generated due to the force/moment in heave- and pitch direction ( $F_3(t)$  &  $F_5(t)$ ). Then the resulting ship motion for pitch can be calculated by:

$$\begin{aligned} \xi_5(x, y, t, \tau) = \mathbb{R} \left[ \sum_{n=1}^N \hat{\eta}_{a,n} H'_5(j\omega_{e,n}, \mu_n) G_{55,i}(j\omega_{e,n}) e^{-j(\omega_n \cdot (t+\tau) + k_{x,n}x + k_{y,n}y)} \right] \\ + \mathbb{R} \left[ \sum_{n=1}^N \hat{\eta}_{a,n} H'_3(j\omega_{e,n}, \mu_n) G_{53,i}(j\omega_{e,n}) e^{-j(\omega_n \cdot (t+\tau) + k_{x,n}x + k_{y,n}y)} \right] \end{aligned} \quad (4.11)$$

where  $G_{53}(j\omega)$  is the TF which relates the heave force ( $F_3(t)$ ) to the pitch motion and  $G_{55}(j\omega)$  relates the pitch moment ( $F_5(t)$ ) to the pitch motion. From the equation above one may notice that this is nothing more than an extension of the motion equation as given in Equation 2.17, Section 2.3, with an additional term for the coupling between the heave-force and pitch-motion. Furthermore, for heave similar argumentation's hold

which results in the following equation:

$$\begin{aligned} \xi_3(x, y, t, \tau) = \mathbb{R} \left[ \sum_{n=1}^N \hat{\eta}_{a,n} H'_3(j\omega_{e,n}, \mu_n) G_{33,i}(j\omega_{e,n}) e^{-j(\omega_n \cdot (t+\tau) + k_{x,n}x + k_{y,n}y)} \right] \\ + \mathbb{R} \left[ \sum_{n=1}^N \hat{\eta}_{a,n} H'_5(j\omega_{e,n}, \mu_n) G_{35,i}(j\omega_{e,n}) e^{-j(\omega_n \cdot (t+\tau) + k_{x,n}x + k_{y,n}y)} \right] \end{aligned} \quad (4.12)$$

where  $G_{35}(j\omega)$  is the TF which relates the pitch-moment ( $F_5(t)$ ) to the heave-motion and  $G_{33}(j\omega)$  relates the heave force ( $F_3(t)$ ) to the heave motion.

#### Transfer-function estimation

Similar to the (SISO) system of the uncoupled motions defined in Section 3.1, the linear time invariant system which now is concerned for pitch is defined as:

$$y_5(t) = g_{5,5}(t) * x_5(t) + g_{5,3}(t) * x_3(t) \quad (4.13)$$

and for heave:

$$y_3(t) = g_{3,3}(t) * x_3(t) + g_{3,5}(t) * x_5(t). \quad (4.14)$$

From the equations as given above, one may notice that in each equations now two unknowns arise, i.e. the  $g_{i,j}(t)$  terms. Since there is only one equation, per DOF, and two unknowns this cannot be solved straight away. In the following paragraphs a system of auto- and cross-spectra will be defined, similar to the  $\overline{CSM}_1$ , which resolves this problem. The derivation will be shown only for pitch because the same derivations also hold for heave.

As for the  $\overline{CSM}_1$ , both sides of Equation 4.13 are first multiplied with  $*x_3(t)$ . Then by substituting the equation into the definition of the DFT the frequency-domain solution becomes:

$$Y_5(j\omega) \frac{1}{N} X_3^*(j\omega) = G_{53}(j\omega) X_3(j\omega) \frac{1}{N} X_3^*(j\omega) + G_{55}(j\omega) X_5(j\omega) \frac{1}{N} X_3^*(j\omega) \quad (4.15)$$

which is equivalent to:

$$\Phi_{y_5 x_3}(j\omega) = G_{53}(j\omega) \Phi_{x_3 x_3}(\omega) + G_{55}(j\omega) \Phi_{x_5 x_3}(j\omega) \quad (4.16)$$

By following the same procedure but now by multiplying Equation 4.13 with  $*x_5(t)$  we can a second equation defined as:

$$\Phi_{y_5 x_5}(j\omega) = G_{53}(j\omega) \Phi_{x_3 x_5}(j\omega) + G_{55}(j\omega) \Phi_{x_5 x_5}(\omega) \quad (4.17)$$

Since there are now two equations and two unknowns ( $G_{53}(j\omega)$  and  $G_{55}(j\omega)$ ), the TF's can be estimated by solving the following matrix vector equation:

$$\begin{bmatrix} \check{\Phi}_{x_3 x_3}(\omega) & \check{\Phi}_{x_5 x_3}(j\omega) \\ \check{\Phi}_{x_3 x_5}(j\omega) & \check{\Phi}_{x_5 x_5}(\omega) \end{bmatrix} \begin{bmatrix} \check{G}_{53}(j\omega) \\ \check{G}_{55}(\omega) \end{bmatrix} = \begin{bmatrix} \check{\Phi}_{y_5 x_3}(j\omega) \\ \check{\Phi}_{y_5 x_5}(\omega) \end{bmatrix} \quad (4.18)$$

For the estimation of the auto- and cross-spectra shown in the equation above, the same techniques can be used as for the  $\overline{CSM}_1$ , that: is Welch averaging and applying window functions.

Following the same line of reasoning for the coupled heave motion, the transfer function  $G_{33}(j\omega)$  and  $G_{35}(j\omega)$  can be found by solving the system:

$$\begin{bmatrix} \check{\Phi}_{x_3 x_3}(\omega) & \check{\Phi}_{x_5 x_3}(j\omega) \\ \check{\Phi}_{x_3 x_5}(j\omega) & \check{\Phi}_{x_5 x_5}(\omega) \end{bmatrix} \begin{bmatrix} \check{G}_{33}(\omega) \\ \check{G}_{35}(j\omega) \end{bmatrix} = \begin{bmatrix} \check{\Phi}_{y_3 x_3}(\omega) \\ \check{\Phi}_{y_3 x_5}(j\omega) \end{bmatrix} \quad (4.19)$$

#### Results

Table 4.18 shows the maximum cross-correlations for heave and pitch for the cases where a coupled- and an un-coupled system is used, as well as the solutions of the pre-calculated TF's. The differences shown in the table are with respect to the correlation coefficients from the pre-calculated TF's ( $H_{0,i}(j\omega)$ ). This difference is calculated by Equation 4.10. From the table one may notice that using a coupled system will always result in

a better/higher correlation coefficient. The largest improvement can be found for heave in run 4. Therefore, in future studies is recommended to use a coupled system rather than an uncoupled system.

Table 4.18: Summary of the cross-correlation coefficients for heave and pitch using a coupled and uncoupled model. The differences as shown are calculated by Equation 4.10 and are with respect to the results when the pre-calculated TF's are used.

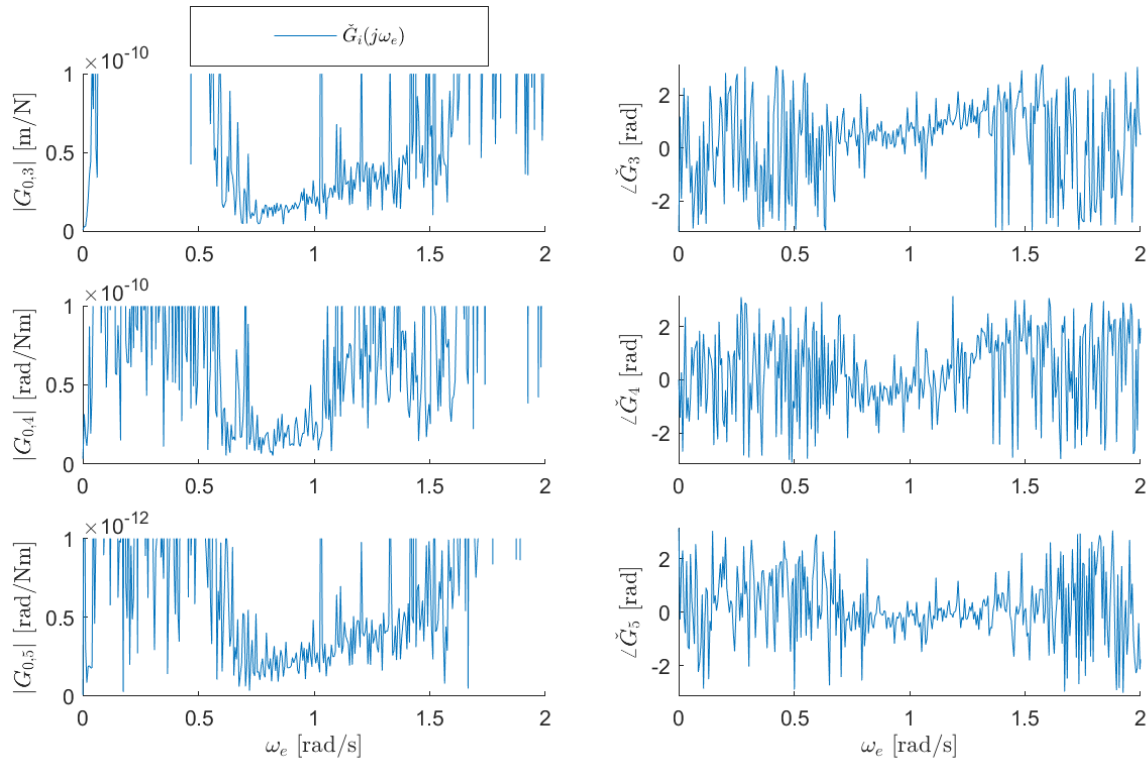
Run	Pre-calculated TF		Coupled TF estimation				Uncoupled TF estimation			
	$\rho_{\xi_i}$		$\rho_{\xi_i}$		Difference [%]		$\rho_{\xi_i}$		Difference [%]	
	Heave	Pitch	Heave	Pitch	Heave	Pitch	Heave	Pitch	Heave	Pitch
1	0.81	0.83	0.87	0.86	4.39	2.49	0.87	0.86	3.92	1.85
2	0.82	0.85	0.88	0.88	3.48	2.11	0.87	0.88	2.79	1.79
3	0.73	0.73	0.85	0.81	7.75	4.85	0.84	0.79	6.89	3.22
4	0.75	0.77	0.86	0.82	6.32	3.17	0.81	0.80	3.19	1.97
5	0.80	0.79	0.87	0.82	3.98	2.26	0.87	0.82	2.65	1.97
6	0.71	0.41	0.77	0.38	3.63	-1.35	0.76	0.37	3.26	-2.38

#### 4.4.2. An alternative method for averaging the ETFE

In Section 3.1.1 it was stated that the numerator and denominator have to be averaged simultaneously when the  $\overline{ETFE}$  method is used, because the signals are stochastic. However, one may say that when the blocks/signals are zero padded to a fixed time origin this is not necessarily required. By zero padding the signals to a fixed point, the phase angles in each block are no longer randomly distributed and so the numerator and denominator can be averaged separately. In other words, when the signals are zero padded to a fixed time origin the TF's can be estimated by:

$$\check{G}_i(j\omega) = \frac{\sum_{m=1}^M Y^m(j\omega)}{\sum_{m=1}^M X^m(j\omega)} \quad (4.20)$$

Figure 4.11 shows for run 2 the estimated transfer-function when this alternative way of averaging is deployed. Comparing this solution to the solution of the  $\overline{ETFE}$  illustrated in Figure 4.10 shows that the variable error is much higher when this alternative way of averaging is used. A possible explanation<sup>2</sup> for this, by averaging the numerator and denominator simultaneously the (cor)relation between  $X(j\omega)$  and  $Y(j\omega)$  is averaged which may act as a filter. By this is meant: Due to (for example) non-linear effects the solutions for each block  $Y^m(j\omega)$  will vary from one realization to another, which on average will result in a rough estimation. However, when the numerator and denominator are averaged simultaneously the outliers in  $Y^m(j\omega)$  will be tempered by the solutions of  $X^m(j\omega)$ , which on average results in a better approximation for the TF's.



(a) Amplitudes of the transfer function

(b) Phase angles of the transfer function

Figure 4.11: Transfer-function for run 2, obtained by alternative averaging of the  $\overline{ETFE}$ . For averaging the following settings have been used: an Hamming window,  $w_l = 400$  [-], and 75% overlap,

<sup>2</sup>Despite great efforts, no proof have been found in literature which sustain this explanation nor another explanation has been found.



# 5

## Conclusions and recommendations

The main objective of this research is to increase the accuracy of real-time motion predictions by substituting an estimated transfer-function from measurement into a linear ship motion model, which is successfully achieved. In this Chapter the main- and sub-questions as defined in Chapter 1 will be answered based on literature, synthetic simulations, and sea trial results. Furthermore, in this chapter also recommendations will be given on how the accuracy of real-time ship motions predictions can be further improved using other models as well as an improvement of the currently used model.

### 5.1. Conclusions

In Section 1.2 the two main questions, and their sub-questions, of this research were formulated. As stated in that section, a distinction is made between estimation techniques recommended for the derivation of transfer-functions and the accuracy of motion predictions. In this section those two main questions will be answered separately.

**(A)** Which transfer-function estimation method and smoothing techniques should be used to increase the accuracy of real-time motion prediction?

In this report two methods are discussed on how to estimate transfer-functions from measured data, the (averaged) Empirical Transfer Function Estimation and the (averaged) Cross-Spectral Method. These methods are both linear approximations which hold a close relationship among each-other, but give different results when averaged. While larger variable errors occur with the *ETFE* methods a bias error may arise when the *CSM* methods are used. Deploying the estimation methods onto synthetic generated data showed that the exact transfer-function can be reasonably well estimated, especially with a combined increase of time and window-length, but depends on a number of factors such as: the amount of noise contained in the system. From the analysis based on sea trial data, it is shown that the most smooth/best estimations can be obtained when the  $\overline{CSM}_1$  is used. Comparing these estimated transfer-functions to those pre-calculated showed that they give different solutions. However, the motion response-spectra based on the estimated transfer-functions has a better relation to the response-spectra of the measured motions compared to the response-spectra based on the pre-calculated transfer-functions. With the above said, it can be concluded that the best estimation of the transfer-function can be obtained by the cross-spectral method in combination with Welch-averaging ( $\overline{CSM}_1$ ).

**(B)** How much does the accuracy of real-time ship motion prediction increase when an estimated transfer-function is used in a linear ship motion model, based on a frequency-domain approach, compared to the solutions obtained from pre-calculated transfer-functions?

From the sea-trial data analysis it is shown that estimated transfer-functions, by the  $\overline{CSM}_1$  method, will increase the maximum cross-correlation coefficient (a measurement of similarity between two signals) with  $\sim 1-10\%$ . From the ratio between the standard deviation of the measured motions and the standard deviation

of the predicted motions, it is shown that the amplitudes of the predicted motions are generally underestimated when estimated transfer-functions are used. With the use of a linear scaling factor, this poor ratio of standard deviations can be resolved without affecting the maximum cross-correlation coefficient. Furthermore, the time-window at which reliable transfer-functions can be estimated is within approximately 5 till 7 minutes. With the above said, it can be concluded that the accuracy of real-time ship motion prediction increases with  $\sim 1 - 10\%$  when estimated transfer-functions are used.

## 5.2. Recommendations

Although it is shown that the accuracy of real-time motion prediction increases by using the method described in this report, there are a few recommendations to further improve the accuracy of real-time ship motion prediction.

The first recommendation, an assessment of the quality/ reliability of the linear wave-force signal ( $F_i(t)$ ). In this report it is assumed that the force signal can be taken as a reliable input for estimation of the transfer-functions and eventually for the motion predictions. From the similarity between the motion-response spectra obtained from the calculated- and measured (heave) motions, it was stated in Section 4.3.1 that this assumption has to be true till some extend but cannot be generalized. Furthermore, in Section 4.3.1 it was also noticed that for some cases the amount of wave-components resolved from the radar data analysis is insufficient, especially for the higher frequencies. As a direct consequence, the motions and forces will not be modeled in for those frequencies and will therefore also not be taken into account when estimating the transfer-functions. In either way, a more accurate force prediction will most likely also result in more accurate motion predictions.

The second recommendation, improving the current model by coupling of the DOF's. In this research a so called Single Input Single Output system is used while in reality the ship motions are coupled, resulting in a Multiple Input Single Output system. In Section 4.4 a method is proposed on how these couplings can be taken into account, by an expansion of the current model and an estimation of the transfer-functions comparable to the  $\overline{CSM}_1$  method. A first research showed that by coupling the heave and pitch motion, the cross-correlation coefficient can be increased with an additional  $\sim 0.2-3\%$ . Therefore, it is recommended in future studies to expand the proposed method from Section 4.4 to all the other DOF's and use that model instead.

The third recommendation, system identification via a non-linear ship motion model. It has been shown from the frequency-domain solutions in Section 4.3 that the largest deviations between the calculated- and measured motion response-spectra can be found near the peak frequencies extending to the higher frequencies. In other words, the solutions becomes less correlated in the regions where large amplitudes and/ or velocities occur. This uncorrelated behaviour comes from non-linear effects which cannot be taken into account using the currently used (linear) motion model. Therefore, a non-linear ship motion model is recommended for future studies. A suggestion where one can start, a time-domain model based on Cummins equation with a quadratic damping term for the viscous damping. This representation of the ship motions is recommended because it is a commonly used method for non-linear ship motions modeling, for example by Conell et al. [3]. In mathematical terms this representation yields:

$$\vec{F}_w(t) = (I + A_\infty)\ddot{\vec{\xi}}(t) + \int_0^t K(t-t')\dot{\vec{\xi}}(t')dt' + \vec{b}_{vis}|\dot{\vec{\xi}}(t)|\dot{\vec{\xi}}(t) + C\ddot{\vec{\xi}}(t) \quad (5.1)$$

where:

$F_w(t)$	=Wave forces and moments
$I$	=Mass and inertia matrix
$A_\infty$	=Added mass matrix at $\omega = \infty$
$C$	=Spring forces matrix
$K$	=Retardation function
$b_{vis}$	=Viscous damping term

Furthermore, the recommended modelling technique is a space state model. This is recommended because, it has already be shown that the Cummins equation can be represented in such a model [19][20][23]

and also quadratic terms can be included. Also, an advantage of parametric modeling is that uncertainties can be estimated from measured data while certain values can be kept fixed values. Under the assumption that the wave-forces can accurately be determined, for an initial starting point it is recommended to take the additional viscous damping coefficient ( $b_{visc}$ ), terms related to inertia ( $I_{xx}, I_{yy}, I_{zz}$ ) and the spring terms related to the metacentric height as unknown variables. This is recommended because these variables are depending on the loading conditions of the ship while the other variables are related to the geometry of the vessel, which are quantities which can be quite accurately determined using BEM software.

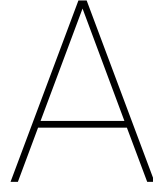
The final recommendation, a comparative study of different motion prediction models. As mentioned in Section 1.1.2 there are several models developed with the aim of motion prediction[5][13][1][3]. Since the sea trial results presented in these works are conducted under different circumstances, that is sea state and vessel, a comparative study is recommended to evaluate which model performs best.



# Bibliography

- [1] Laura K Alford, Robert F Beck, Joel T Johnson, David Lyzenga, Okey Nwogu, and Alan Zundel. Design , Implementation , and Evaluation of a System for Environmental and Ship Motion Forecasting. In *30th Symposium on Naval Hydrodynamics*, pages 2–7, Australia, 2014.
- [2] Julius S. Bendat and Allan G. Piersol. *Random data: Analysis and measurement Procedures*. John Wiley & Sons, Inc., 4th edition, 2010.
- [3] Benjamin S H Connell, Jason P Rudzinsky, Christopher S Brundick, William M Milewski, John G Kusters, and Gordon Farquharson. Development of an environmental ship and ship motion forecasting. *ASME 2015 34th International Conference on Ocean, Offshore and Arctic Engineering*, 11:1–11, 2015.
- [4] L. Cornejo-Bueno, J.C. Nieto Borge, Enrique Alexandre, K. Hessner, and S. Salcedo-Sanz. Accurate estimation of significant wave height with Support Vector Regression algorithms and marine radar images. *Coastal Engineering*, 114:233–243, 2016.
- [5] Jens Dannenberg, Katrin Hessner, Peter Naaijen, Henk van den Boom, and Konstanze Reichert. The On board Wave and Motion Estimator OWME. *Proceedings of the International Offshore and Polar Engineering Conference*, 3:424–431, 2010.
- [6] Yoshimi Goda. *Random Seas and Design of Maritime Structures*. World Scientific Publishing Co Pte Ltd, 3th edition, 2000.
- [7] Paul M.J. Hof. *System Identification*. Delft University of Technology, 2006.
- [8] Leo H. Holthuijsen. *Waves in Oceanic and Costal Waters*. Cambridge University Press, 2010.
- [9] W. Journée and Johan M.J. Massie. *Offshore Hydrodynamics*. Delft University of Technology, 2001.
- [10] Toru Katayama. Numerical Estimation of Roll Damping. *ITTC - Recommended Procedures*, pages 1–33, 2011.
- [11] Lennart. Ljung. *System identification: theory for the user*. Prentice Hall PTR, 2th edition, 1999.
- [12] P Naaijen and R H M Huijsmans. Real Time Wave Forecasting For Real Time Ship Motion Predictions. *Proceedings of the ASME 2008 27th International Conference on Ocean, Offshore and Arctic Engineering*, 4:607–614, 2008.
- [13] P. Naaijen, D.K. Roozen, and R H M Huijsmans. Reducing operational risk by on-board phase resolved prediction of wave induced ship motions. In *Proceedings of 35th International Conference on Ocean, Offshore and Arctic Engineering*, pages 1–11, 2016.
- [14] Peter Naaijen, Karel Roozen, Kees van Oosten, and Riaan van't (TU Delft) Veer. VALIDATION OF A DETERMINISTIC WAVE AND SHIP MOTION PREDICTION SYSTEM. In *Proceedings of the 37th International Conference on Ocean, Offshore & Arctic Engineering, OMAE2018*, pages 1–8, 2018.
- [15] Ulrik D Nielsen and Toshio Iseki. Prediction of First-Order Vessel Responses with Applications to Decision Support Systems. *Proceedings of the World Maritime Technology Conference. Society of Naval Architects and Marine Engineers.*, pages 1–11, 2015.
- [16] Ulrik D Nielsen and David C Stredulinsky. Onboard Sea State Estimation Based on Measured Ship Motions. *Proceedings of the 12th International Ship Stability Workshop*, pages 61–67, 2011.
- [17] Ulrik Dam Nielsen and Jørgen Juncher Jensen. A novel approach for navigational guidance of ships using onboard monitoring systems. *Ocean Engineering*, 38(2-3):444–455, 2011.

- [18] José Carlos Nieto Borge, Katrin Hessner, and Konstanze Reichert. Estimation of the Significant Wave Height With X-Band Nautical Radars. *Proc. 18th Int. Conf. Offshore Mech.*, (C):1–8, 1999.
- [19] T. Perez and T. I. Fossen. Time domain models of marine surface vessels based on seakeeping computations. *7th Conference on Manoeuvring and Control of Marine Craft MCMC*, 2006.
- [20] Tristan Pérez and Thor I. Fossen. Time-vs. frequency-domain Identification of parametric radiation force models for marine structures at zero speed. *Modeling, Identification and Control*, 29(1):1–19, 2008.
- [21] Rik Pintelon and Johan Schoukens. *System identification a frequency domain approach*. John Wiley & Sons, 2th edition.
- [22] Ed Alexander D Poularikas. *The Handbook of Formulas and Tables for Signal Processing*. CRC Press, 1998.
- [23] Reza Taghipour, Tristan Perez, and Torgeir Moan. Hybrid frequency-time domain models for dynamic response analysis of marine structures. *Ocean Engineering*, 35(7):685–705, 2008.



## (Discrete) Fourier Transform

A Fourier Transform transforms a signal from the time-domain into the frequency-domain. In continuous form this function is defined as [7]:

$$F(j\omega) = \frac{1}{2\pi} \int_{-\infty}^{\infty} f(t) e^{-j\omega t} dt \quad (\text{A.1})$$

The inverse operation, known as the Inverse Fourier Transformation (IFT), transforms the frequency-domain description back into the time-domain and is defined as:

$$f(t) = \int_{-\infty}^{\infty} F(\omega) e^{j\omega t} d\omega \quad (\text{A.2})$$

The combined equations as given above are often referred to as a Fourier transform pair. Since the FT is a complex number it has an amplitude and a phase-angle. The amplitudes can be calculated by taking the square root of the real parts and the imaginary parts squared. I.e.:

$$F_a(\omega) = \sqrt{\text{Re}\{F(\omega)\}^2 + \text{Im}\{F(\omega)\}^2} \quad (\text{A.3})$$

And the phase angles can be calculated by taking the inverse tangent:

$$\epsilon(\omega) = \tan^{-1} \left( \frac{\text{Im}\{F(\omega)\}}{\text{Re}\{F(\omega)\}} \right) \quad (\text{A.4})$$

### Discrete and Fast Fourier Transform

The FT given in Equation A.1 assumes that the signal  $f(t)$  is continuous and infinite, while in practice discrete signals are finite and discrete. Therefore, in the numerical model the discrete version, the DFT, of this equation has been used which is defined as [21]:

$$F(\omega_d) = \sum_{n_s=0}^{N_s-1} f(n_s f_s) e^{-j \frac{2\pi}{N_s} \omega_d n_s} \quad (\text{A.5})$$

and its inverse (IDFT) is given by:

$$f(n_s f_s) = \frac{1}{N_s} \sum_{\omega_d=0}^{N_s-1} F(\omega_d) e^{j \frac{2\pi}{N_s} \omega_d n_s} \quad (\text{A.6})$$

Similar to the FT, the amplitudes for each frequency component  $k_n$  can be calculated by:

$$x_{a_n}(k_n) = \sqrt{\text{Re}\{F(\omega_d)\}^2 + \text{Im}\{F(\omega_d)\}^2} \quad (\text{A.7})$$

and the phase angles by:

$$\epsilon_n(k_n) = \tan^{-1} \left( \frac{\text{Im}\{F(\omega_d)\}}{\text{Re}\{F(\omega_d)\}} \right). \quad (\text{A.8})$$

Furthermore, the frequency step related to the DFT as given in the equation above is defined as:

$$\Delta\omega = \frac{f_s}{N_s}. \quad (\text{A.9})$$

In order to solve the DFT and IDFT in literature different algorithms can be found. The collective name of these DFT algorithms is the Fast Fourier Transform (FFT) where the most common algorithm is the Cooley algorithm.

# B

## Synthetization of oceanic waves

This appendix describes how synthetic are generated for the synthetic evaluations in Section 3.4 and 4.2. For the synthetization of the the wave-field the method as proposed by Goda [6] is used. For this method first, a 2-D wave-spectrum needs to be defined. Secondly, with the use of a distribution function directional. The wave-spectrum which is used in this report is a JONSWAP spectrum

### Wave-field description

The behaviour of oceanic and coastal waves can be classified a stochastic process [8]. Although it is stochastic, when the surface elevation is recorded with for example a wave-buoy or radar it is possible to reconstruct the surface elevation using a Fourier Series expansion. A 3-D time-domain description of the wave-field using such an expansion can be defined as [8]:

$$\eta(x, y, t) = \mathbb{R} \left\{ \sum_{n=1}^N \eta_{a,n} e^{-i(\omega_n \cdot t - k_{x,n} \cdot x - k_{y,n} \cdot y - \epsilon_n)} \right\} \quad (\text{B.1})$$

where:

$$\begin{aligned} k_{x,n} &= k_n \cdot \cos(\mu_n) \\ k_{y,n} &= k_n \cdot \sin(\mu_n) \end{aligned} \quad (\text{B.2})$$

where the wave number  $k_n$  can be found solving the dispersion relation, i.e.:

$$\omega_n^2 = kg \tanh(kh). \quad (\text{B.3})$$

According to Goda [6] the phase angle  $\epsilon_n$  should be chosen random with a normal distribution between  $0 \leq \epsilon_n \leq 2\pi$ . Before the wave amplitudes,  $\eta_{a,n}$ , and wave directions,  $\mu_n$ , can be determined a wave energy spectrum and a directional function have to be defined.

### JOHNSWAP wave spectrum

A wave energy spectrum contains information about how energy is distributed among the frequency components. In literature different wave energy spectra can be found like the Pierson-Moskowitz, JOHNSWAP and Bretschneider spectra. These spectra are developed for certain geological positions on earth. For the generation of the synthetic data the JOHNSWAP spectrum has been adopted into the model, developed around 1970 and is defined as [8]:

$$S_\eta(\omega) = \frac{320 \cdot H_{1/3}^2}{T_p^4} \cdot \omega^{-5} \exp\left(\frac{-1950}{T_p^4} \omega^{-4}\right) \gamma^A \quad (\text{B.4})$$

where:

$$\gamma = 3.3 \quad (\text{B.5})$$

$$A = \exp \left[ - \left( \frac{\omega - \omega_p}{\sigma \sqrt{2}} \right)^2 \right] \quad (\text{B.6})$$

$$\sigma = \begin{cases} 0.07 & \omega \leq \omega_p \\ 0.09 & \omega > \omega_p \end{cases} \quad (\text{B.7})$$

where  $\omega_p$  is the peak frequency. Figure B.1a shows an example of the JOHNSWAP spectrum with  $T_p = 8$ [s] and  $H_{1/3} = 2$  [m].

### Distribution functions

The spectrum defined in the previous section does not contain any directional information. In practice this is added by applying a distribution functions. This function distributes the wave-energy among different wave directions and in general expressed as:

$$S_\eta(\omega, \mu^*) = S(\omega)_\eta D(\mu^* | \omega) \quad (\text{B.8})$$

where:

$$\mu^* = \mu + \bar{\mu}. \quad (\text{B.9})$$

$\bar{\mu}$  is defined as the mean wave direction. Although many distribution functions can be found in literature they all have to satisfy the condition:

$$\int_{-\pi}^{\pi} D(\mu^* | f) d\mu^* = 1 \quad (\text{B.10})$$

which ensures that energy is preserved. In this thesis the distribution function is defined as [6] :

$$D(\mu^*) = \frac{1}{\sqrt{\pi}} \frac{\Gamma(1+s)^2}{\Gamma(2s+1)} \cos^{2s} \left( \frac{\mu^*}{2} \right) \quad \text{with: } -\pi/2 \leq \mu^* \leq \pi/2 \quad (\text{B.11})$$

where  $\Gamma$  is the gamma function and  $s = 5$ . Figure B.1b shows an example of the directional function as described above.

### Wave amplitudes and directions

For the selection of the individual wave-height components from Equation B.1 the most robust method, the single summation method, as proposed by Goda [6] has been used. Here a single wave height component can be calculated by:

$$\eta_n = \sqrt{2S_\zeta(\omega_n) \Delta\omega_n} \quad (\text{B.12})$$

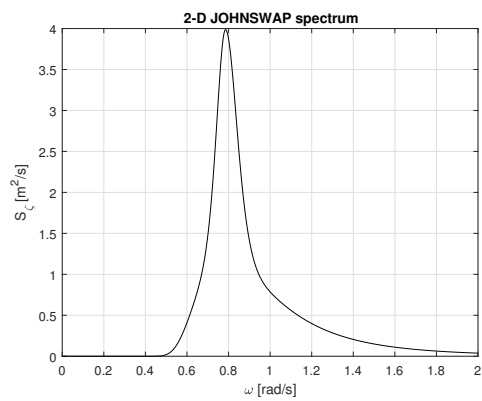
which takes the wave spectra from Equation B.4 into account. When this equation is substituted in Equation B.1 the wave-field can be calculated by:

$$\eta(x, y, t) = \Re \left[ \sum_{n=1}^N \sqrt{2S_\zeta(\omega_n) \Delta\omega_n} e^{-i(\omega_n \cdot t - k_{x,n} \cdot x - k_{y,n} \cdot y - \epsilon_n)} \right] \quad (\text{B.13})$$

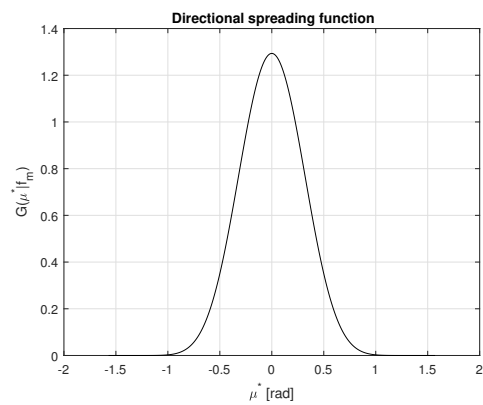
The last thing remaining is to define a wave-direction,  $\mu_n$ . This has been accomplished by solving:

$$\mu_n = F^{-1}(R_n) - \bar{\mu} \quad : \quad F(\mu^* | \omega_n) = \int_0^{2\pi} D(\mu^* | \omega_n) d\mu, \quad (\text{B.14})$$

where  $F(\mu^* | \omega_n)$  is the cumulative distribution function and  $R_n$  is a random number normally distributed between 0 and 1. I.e.,  $\mu_n$  is the solution of the inverse cumulative distribution function for a random number  $R_n$ .



(a) JOHNSWAP wave spectrum



(b) Directional spreading function

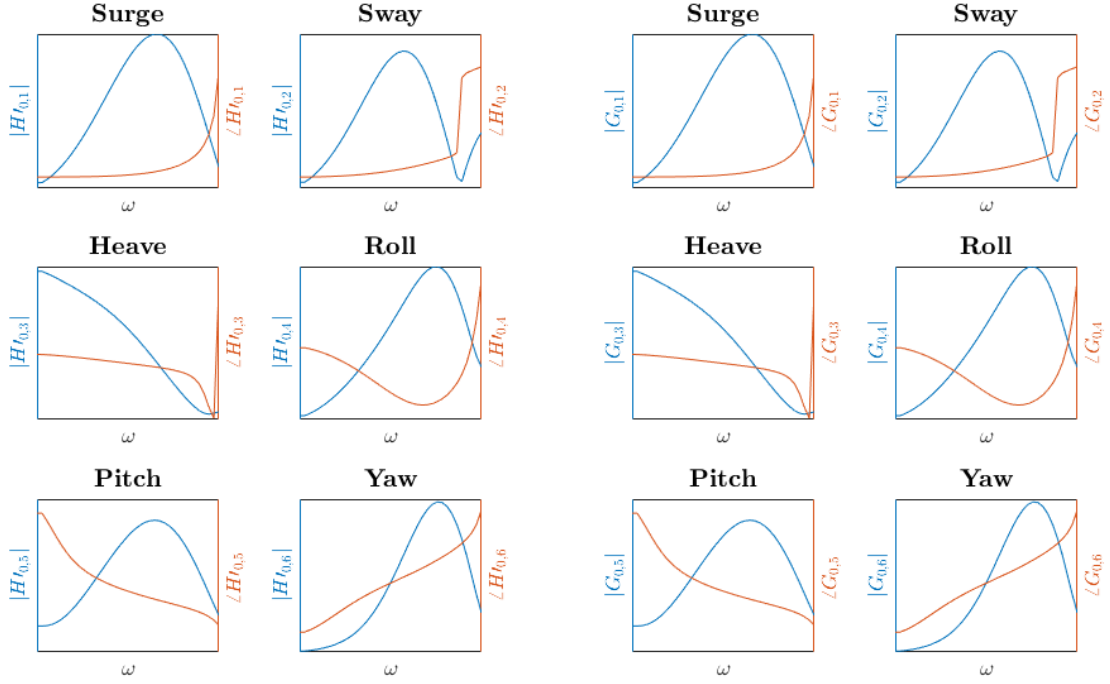
Figure B.1: JOHNSWAP spectrum and directional spreading function



# C

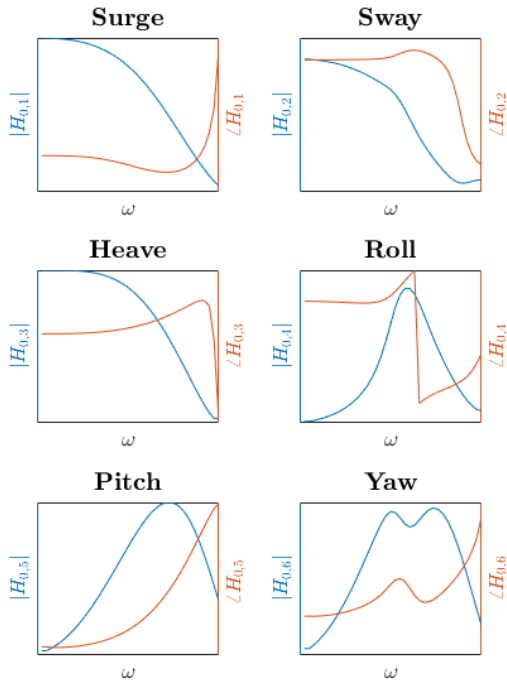
## Response Amplitude Operators

In this Appendix the TF's corresponding to the SPA-4207 are shown, for illustrative purposes. Due to confidential reasons the numbers on the axis are not shown. Figure C.1a shows the wave-to-force TF's ( $H'_{0,i}(j\omega)$ ). Figure C.1b shows the force-to-motion TF's ( $G_{0,i}(j\omega)$ ). Figure C.1c shows the wave-to-motion TF ( $H'_{0,i}(j\omega)$ ) or RAO's



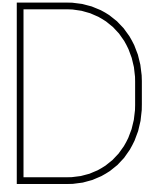
(a) Pre-calculated wave-to-force TF's

(b) Pre-calculated force-to-motion TF's



(c) Pre-calculated wave-to-motion TF's

Figure C.1: Illustrative example of the amplitudes and phase angles of the pre-calculated TF's. Figure C.1a shows the wave-to-force TF's ( $H'_{0,i}(j\omega)$ ). Figure C.1b shows the force-to-motion TF's ( $G_{0,i}(j\omega)$ ). Figure C.1c shows the wave-to-motion TF ( $H'_{0,i}(j\omega)$ ) or RAO's



## Sea trial results

In this Appendix the figures equivalent to those shown for run 2 in Section 4.3.1 for all the runs are given. To recall, the transfer-functions have been estimated by the  $\overline{CSM}_1$  method with a Hamming window, a window-length of  $w_l = 400$  [-], and an overlap of 75%. The figures which will be shown for each run are:

- A time-domain description of the measured and calculated motions
- The cross-correlation coefficients
- An estimation of the TF's ( $\check{G}_i(j\omega)$ ) and the pre-calculated TF's ( $G_{0,i}(j\omega)$ )
- The motion response-spectra -or auto-spectra- of the measured and calculated motions
- The Coherence function

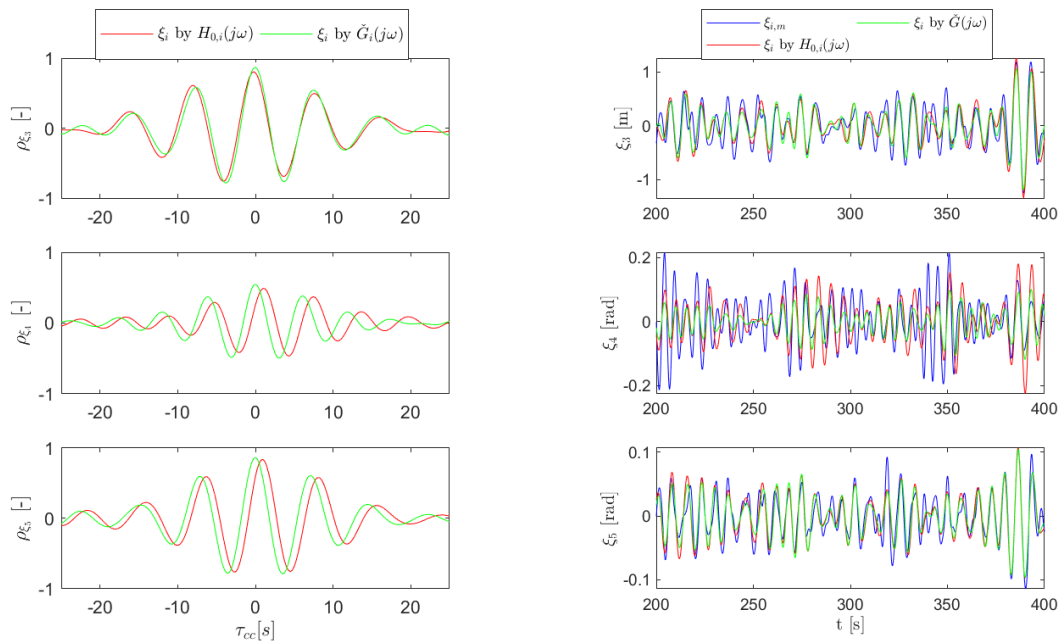
The conditions at which the sea-trials were conducted are re-summarized in the table below.

Table D.1: Sea trial conditions

Run no.	Name	SOG [m/s]	$\mu$ [deg]	Duration [s]	$T_p$ [s]	$H_{1/3}$ [m]
1	Bow-quartering seas	0.52	161	736	7.6	2.2
2	Head seas	2.32	174	1306	7.5	2.2
3	Stern-quartering seas	4.10	307	1392	7.7	2.2
4	Following seas	2.72	346	1256	7.6	2.2
5	Bow-quartering seas	0.71	129	884	7.4	2.2
6	Beam seas	3.17	84	936	7.5	2.2

## Run 1

### Time-domain solutions

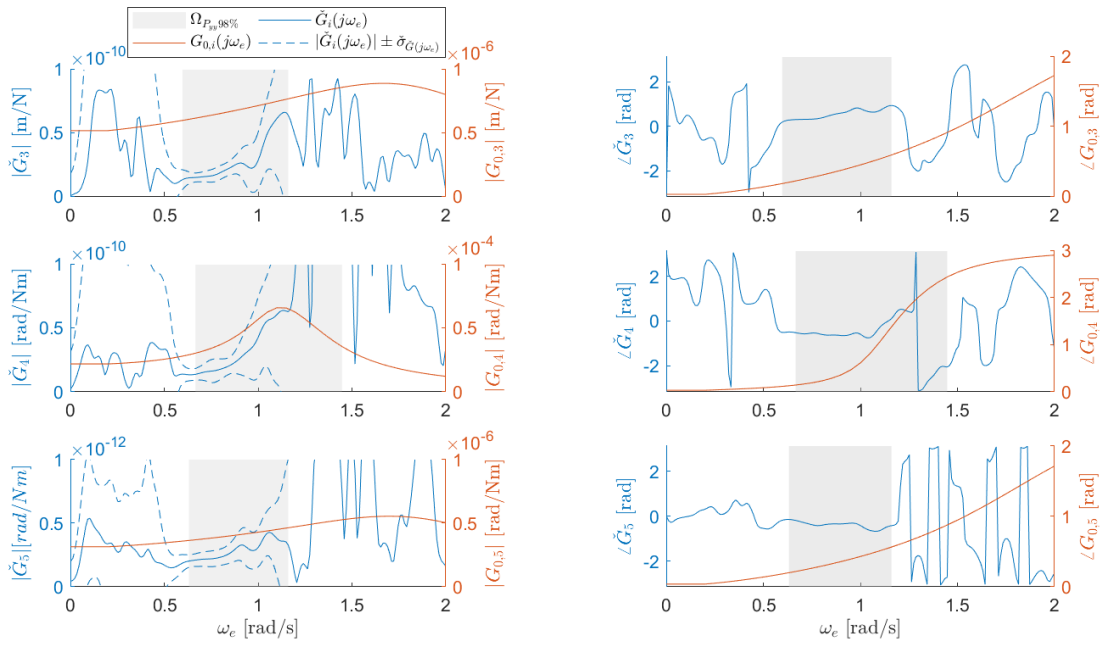


(a) Pierson cross-correlation coefficient

(b) Time domain solution

Figure D.1: Run 1: The left figure shows the cross-correlation coefficients between the measured- and predicted motions for. In the right figure the time-domain solutions of the measured motions are shown by the blue line. The green lines in both figures represents that the motions are predicted by using estimated TF's ( $\tilde{G}_i(j\omega)$ ) while the red lines show the solutions of the pre-calculated TF's ( $H_{0,i}(j\omega)$ ). Furthermore,  $\tilde{G}_i(j\omega)$  has been estimated by the  $\overline{CSM}_1$  with: a Hamming window, a window-length of  $w_l = 400$  [-], and an overlap of 75%.

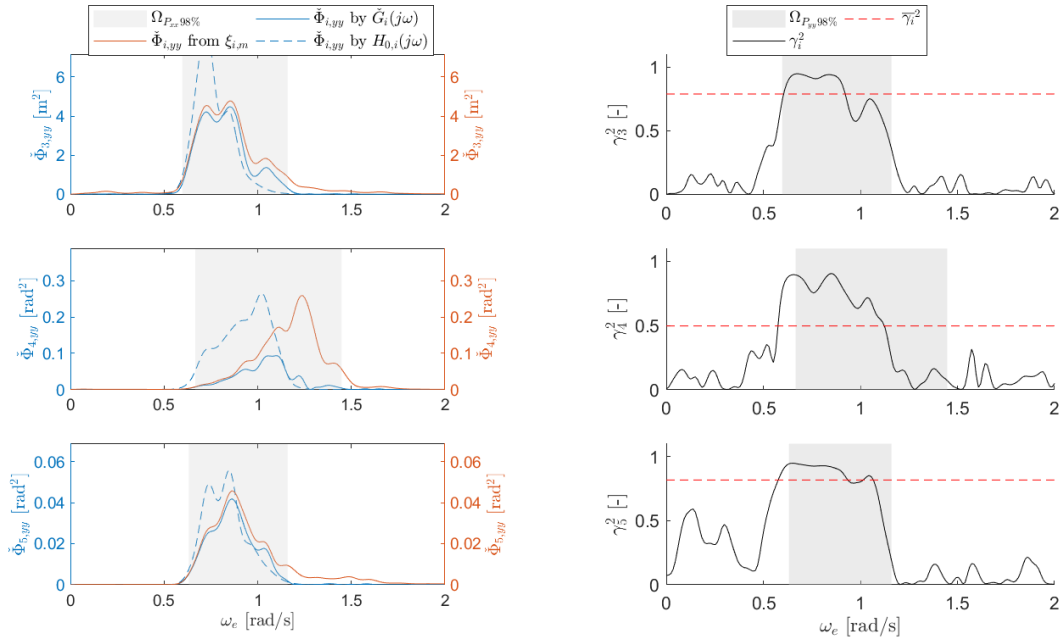
## Frequency domain solutions



(a) Amplitudes of the transfer function

(b) Phase angles of the transfer function

Figure D.2: Run 1: The amplitudes and phase angles for of the pre-calculated TF's (solid red) and estimated TF's (solid blue). The blue dashed line represents the estimated TF plus or minus the estimated standard deviation. The grey area represents the domain which contains 98% of the energy of the motion response-spectra.  $\hat{G}_i(j\omega)$  has been estimated by  $\overline{\text{CSM}}_1$  with: a Hamming window, a window-length of  $w_l = 400$  [-], and an overlap of 75%.



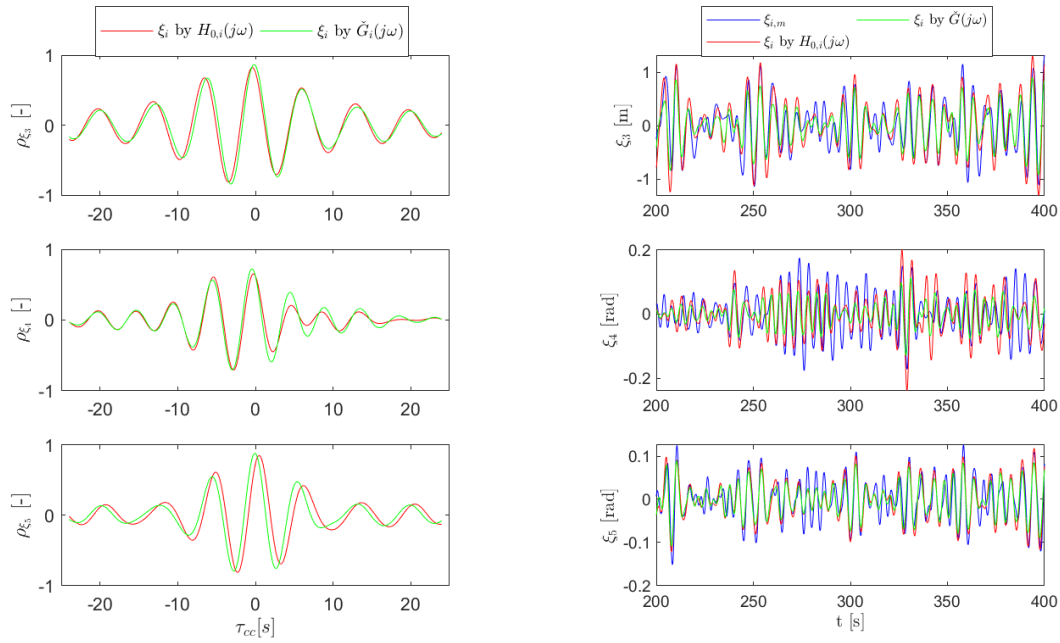
(a) Motion response-spectra

(b) Coherence function

Figure D.3: Run 1: The motion response-spectra (left) and the Coherence function (right). The blue dashed line in the left figure represents the motion response-spectra of the predicted motions obtained from pre-calculated TF's ( $H_{0,i}(j\omega)$ ). The solid blue line shows the motion response-spectra in the case that estimated TF's ( $\hat{G}_i(j\omega)$ ) are used. In the right figure, the red-dashed line is the mean coherence of the grey domain.  $\hat{G}_i(j\omega)$  has been estimated by  $\overline{\text{CSM}}_1$  with: a Hamming window, a window-length of  $w_l = 400$  [-], and an overlap of 75%.

## Run 2

### Time-domain solutions

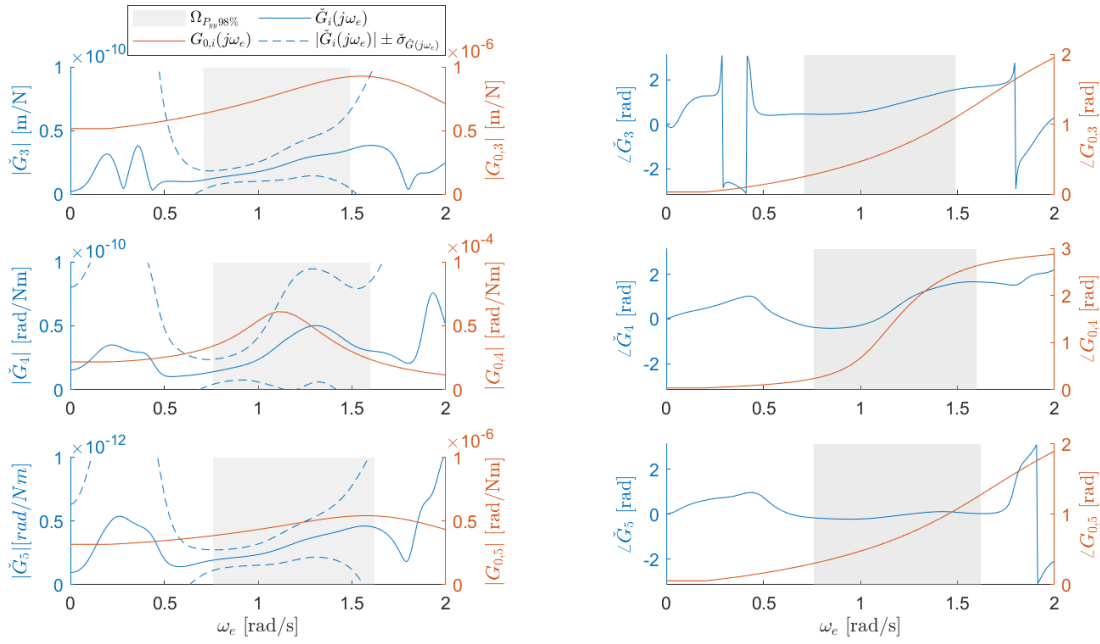


(a) Pierson correlation-coefficient

(b) Time domain solution

Figure D.4: Run 2: The left figure shows the cross-correlation coefficients between the measured- and predicted motions for. In the right figure the time-domain solutions of the measured motions are shown by the blue line. The green lines in both figures represents that the motions are predicted by using estimated TF's ( $\tilde{G}_i(j\omega)$ ) while the red lines show the solutions of the pre-calculated TF's ( $H_{0,i}(j\omega)$ ). Furthermore,  $\tilde{G}_i(j\omega)$  has been estimated by the  $\overline{CSM}_1$  with: a Hamming window, a window-length of  $w_l = 400$  [-], and an overlap of 75%.

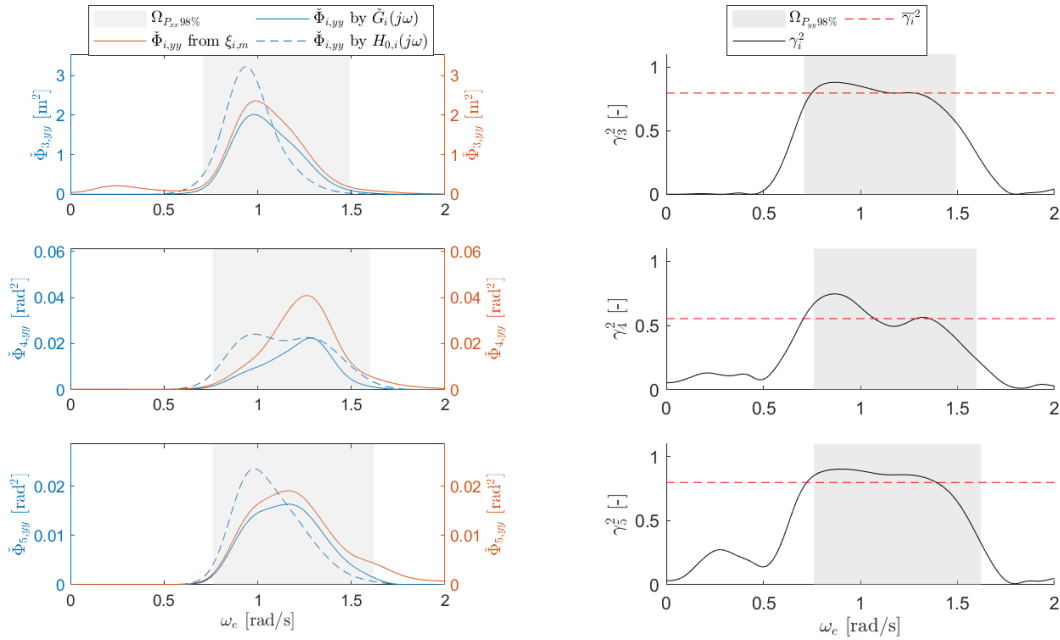
## Frequency-domain solutions



(a) Amplitudes of the transfer function

(b) Phase angles of the transfer function

Figure D.5: Run 2: The amplitudes and phase angles for of the pre-calculated TF's (solid red) and estimated TF's (solid blue). The blue dashed line represents the estimated TF plus or minus the estimated standard deviation. The grey area represents the domain which contains 98% of the energy of the motion response-spectra.  $\hat{G}_i(j\omega)$  has been estimated by  $\overline{CSM}_1$  with: a Hamming window, a window-length of  $w_l = 400$  [-], and an overlap of 75%.



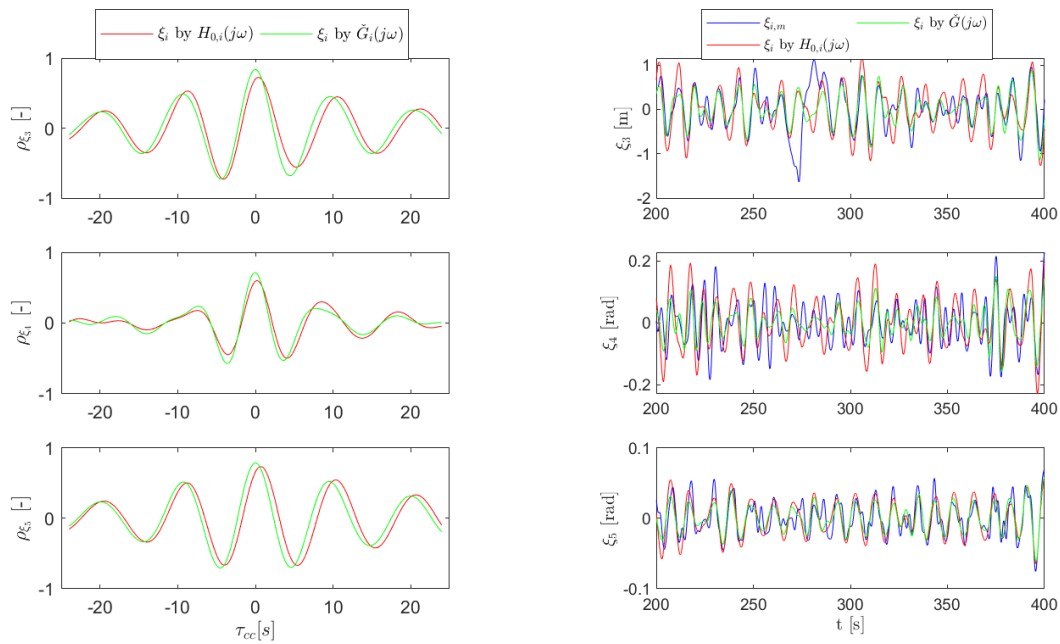
(a) Motion response-spectra

(b) Coherence function

Figure D.6: Run 2: The motion response-spectra (left) and the Coherence function (right). The blue dashed line in the left figure represents the motion response-spectra of the predicted motions obtained from pre-calculated TF's ( $H_{0,i}(j\omega)$ ). The solid blue line shows the motion response-spectra in the case that estimated TF's ( $\hat{G}_i(j\omega)$ ) are used. In the right figure, the red-dashed line is the mean coherence of the grey domain.  $\hat{G}_i(j\omega)$  has been estimated by  $\overline{CSM}_1$  with: a Hamming window, a window-length of  $w_l = 400$  [-], and an overlap of 75%.

### Run 3

#### Time-domain solutions



(a) Pierson correlation-coefficient

(b) Time domain solution

Figure D.7: Run 3: The left figure shows the cross-correlation coefficients between the measured- and predicted motions for. In the right figure the time-domain solutions of the measured motions are shown by the blue line. The green lines in both figures represents that the motions are predicted by using estimated TF's ( $\check{G}_i(j\omega)$ ) while the red lines show the solutions of the pre-calculated TF's ( $H_{0,i}(j\omega)$ ). Furthermore,  $\check{G}_i(j\omega)$  has been estimated by the  $\overline{CSM}_1$  with: a Hamming window, a window-length of  $w_l = 400$  [-], and an overlap of 75%.

## Frequency-domain solutions

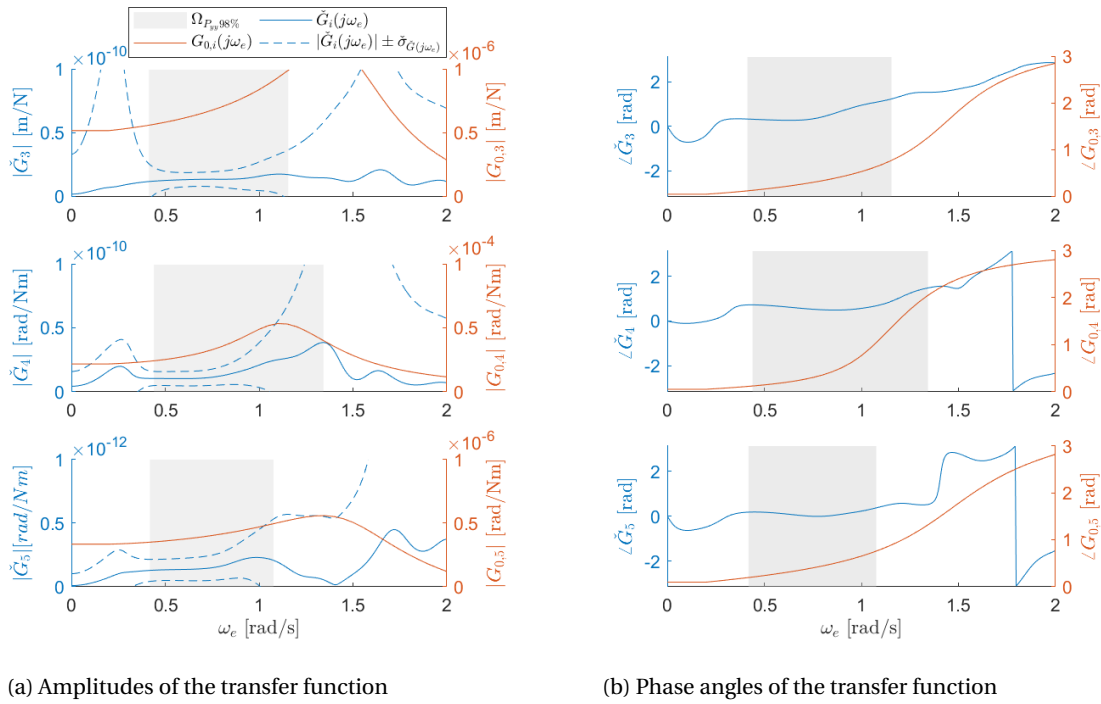


Figure D.8: Run 3: The amplitudes and phase angles for the pre-calculated TF's (solid red) and estimated TF's (solid blue). The blue dashed line represents the estimated TF plus or minus the estimated standard deviation. The grey area represents the domain which contains 98% of the energy of the motion response-spectra.  $\hat{G}_i(j\omega)$  has been estimated by  $\overline{CSM}_1$  with: a Hamming window, a window-length of  $w_l = 400$  [-], and an overlap of 75%.

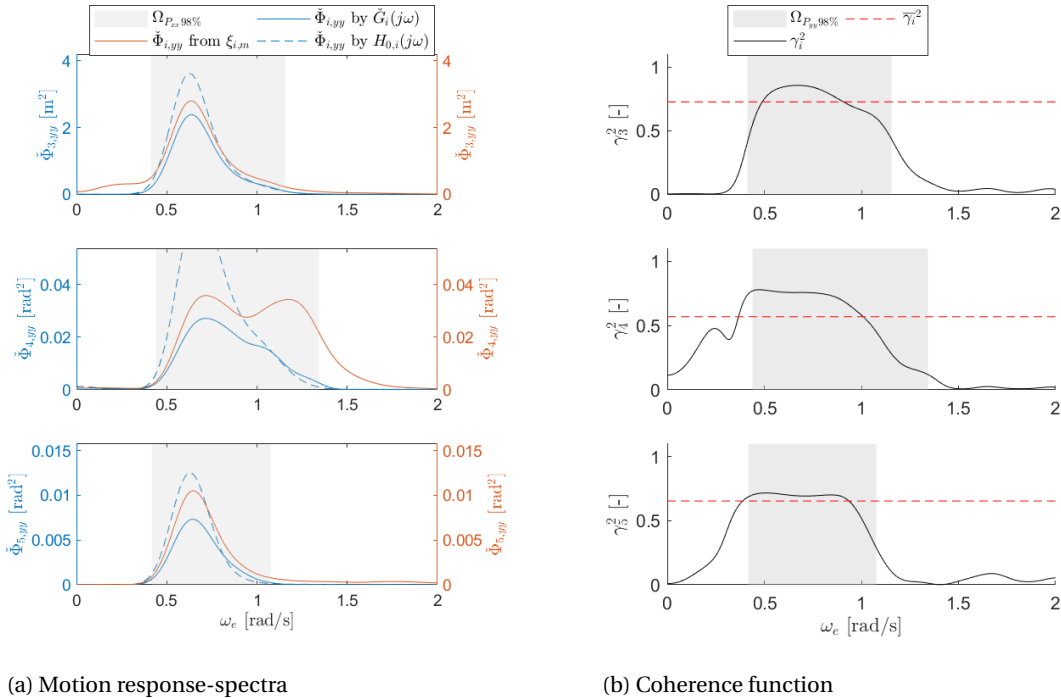
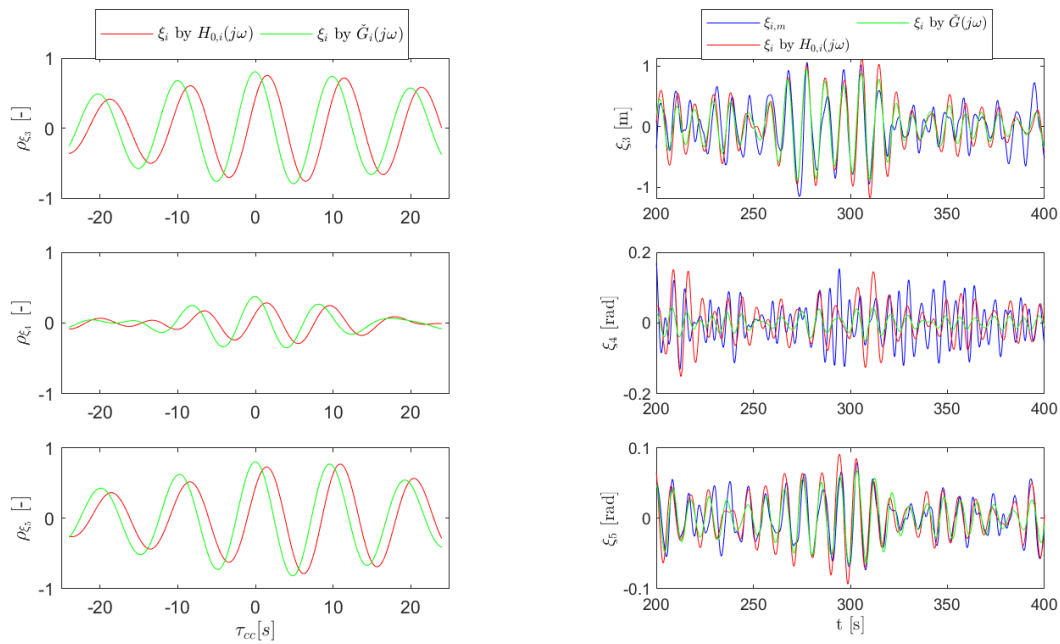


Figure D.9: Run 3: The motion response-spectra (left) and the Coherence function (right). The blue dashed line in the left figure represents the motion response-spectra of the predicted motions obtained from pre-calculated TF's ( $H_{0,i}(j\omega)$ ). The solid blue line shows the motion response-spectra in the case that estimated TF's ( $\hat{G}_i(j\omega)$ ) are used. In the right figure, the red-dashed line is the mean coherence of the grey domain.  $\hat{G}_i(j\omega)$  has been estimated by  $\overline{CSM}_1$  with: a Hamming window, a window-length of  $w_l = 400$  [-], and an overlap of 75%.

## Run 4

## Time-domain solutions

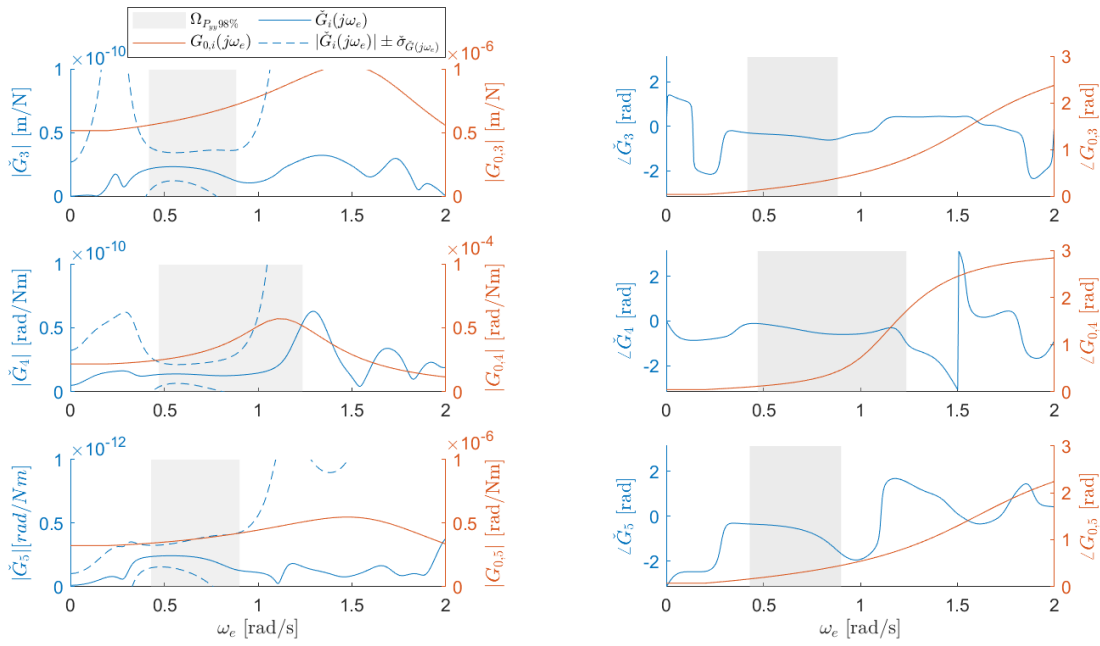


(a) Pierson correlation-coefficient

(b) Time domain solution

Figure D.10: Run 4: The left figure shows the cross-correlation coefficients between the measured- and predicted motions for. In the right figure the time-domain solutions of the measured motions are shown by the blue line. The green lines in both figures represents that the motions are predicted by using estimated TF's ( $\check{G}_i(j\omega)$ ) while the red lines show the solutions of the pre-calculated TF's ( $H_{0,i}(j\omega)$ ). Furthermore,  $\check{G}_i(j\omega)$  has been estimated by the  $\overline{CSM}_1$  with: a Hamming window, a window-length of  $w_l = 400$  [-], and an overlap of 75%.

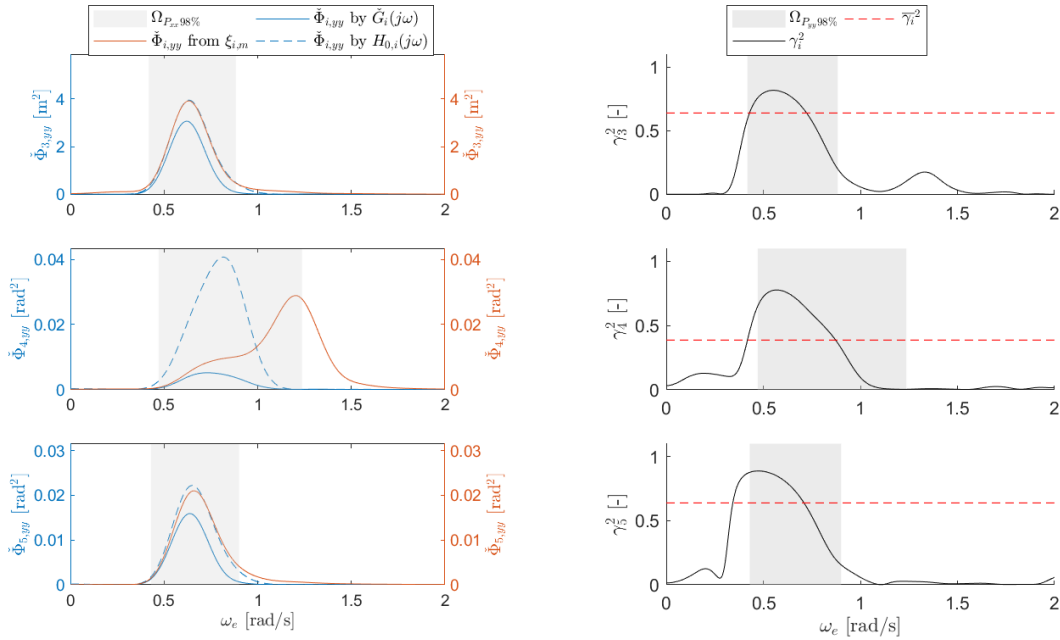
## Frequency-domain solutions



(a) Amplitudes of the transfer function

(b) Phase angles of the transfer function

Figure D.11: Run 4: The amplitudes and phase angles for of the pre-calculated TF's (solid red) and estimated TF's (solid blue). The blue dashed line represents the estimated TF plus or minus the estimated standard deviation. The grey area represents the domain which contains 98% of the energy of the motion response-spectra.  $\hat{G}_i(j\omega)$  has been estimated by  $\overline{CSM}_1$  with: a Hamming window, a window-length of  $\omega_l = 400$  [-], and an overlap of 75%.



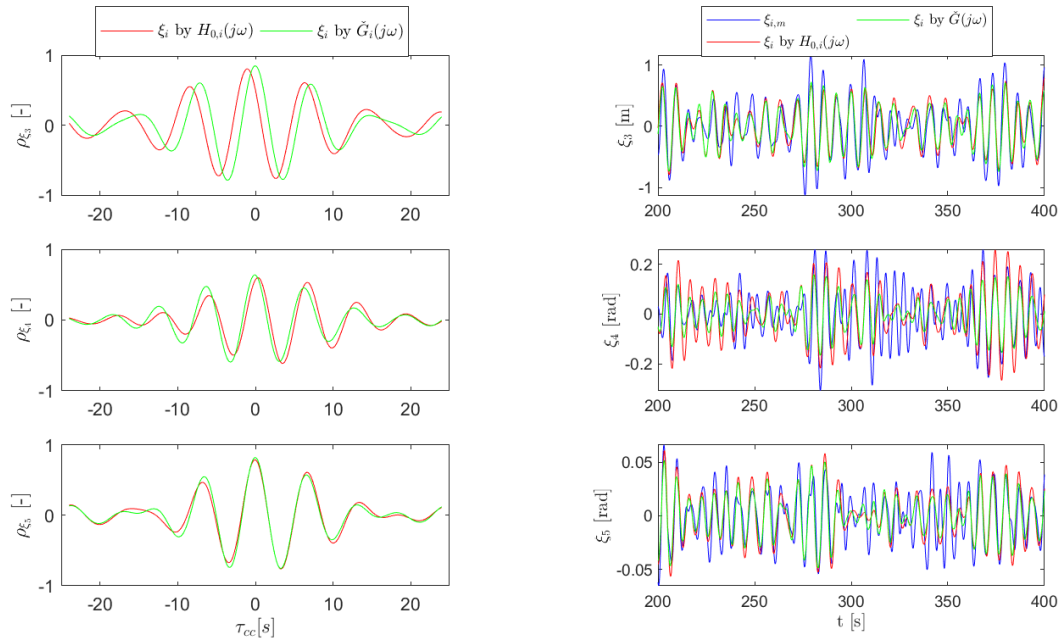
(a) Motion response-spectra

(b) Coherence function

Figure D.12: Run 4: The motion response-spectra (left) and the Coherence function (right). The blue dashed line in the left figure represents the motion response-spectra of the predicted motions obtained from pre-calculated TF's ( $H_{0,i}(j\omega)$ ). The solid blue line shows the motion response-spectra in the case that estimated TF's ( $\hat{G}_i(j\omega)$ ) are used. In the right figure, the red-dashed line is the mean coherence of the grey domain.  $\hat{G}_i(j\omega)$  has been estimated by  $\overline{CSM}_1$  with: a Hamming window, a window-length of  $\omega_l = 400$  [-], and an overlap of 75%.

## Run 5

## Time-domain solutions

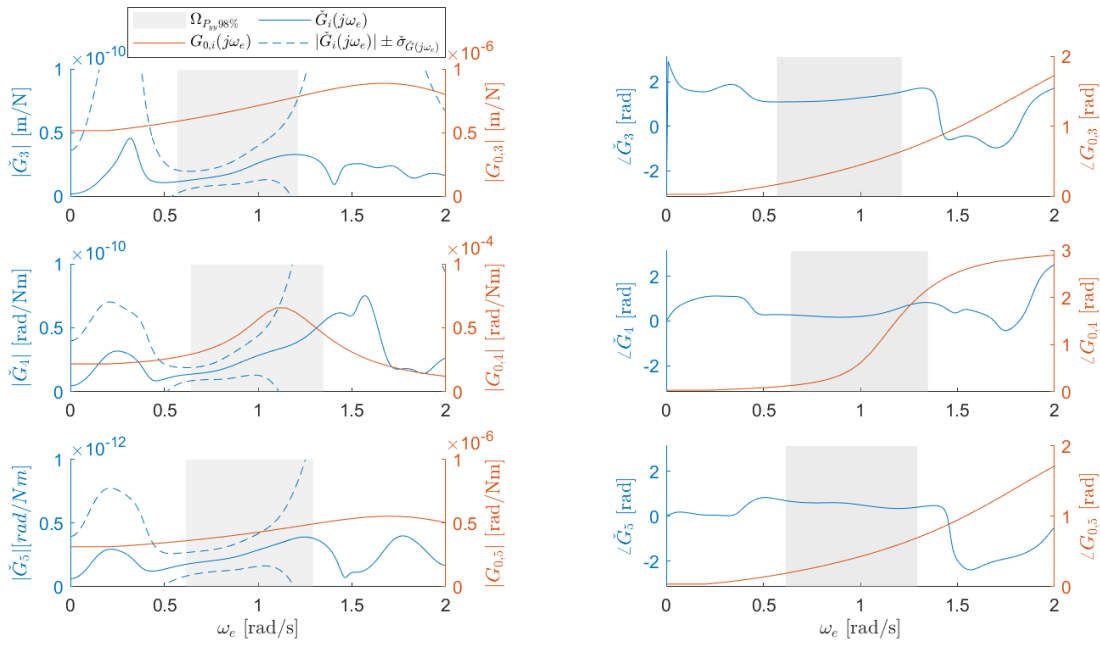


(a) correlation-coefficient

(b) Time domain solution

Figure D.13: Run 5: The left figure shows the cross-correlation coefficients between the measured- and predicted motions for. In the right figure the time-domain solutions of the measured motions are shown by the blue line. The green lines in both figures represents that the motions are predicted by using estimated TF's ( $\check{G}_i(j\omega)$ ) while the red lines show the solutions of the pre-calculated TF's ( $H_{0,i}(j\omega)$ ). Furthermore,  $\check{G}_i(j\omega)$  has been estimated by the  $\overline{CSM}_1$  with: a Hamming window, a window-length of  $w_l = 400$  [-], and an overlap of 75%.

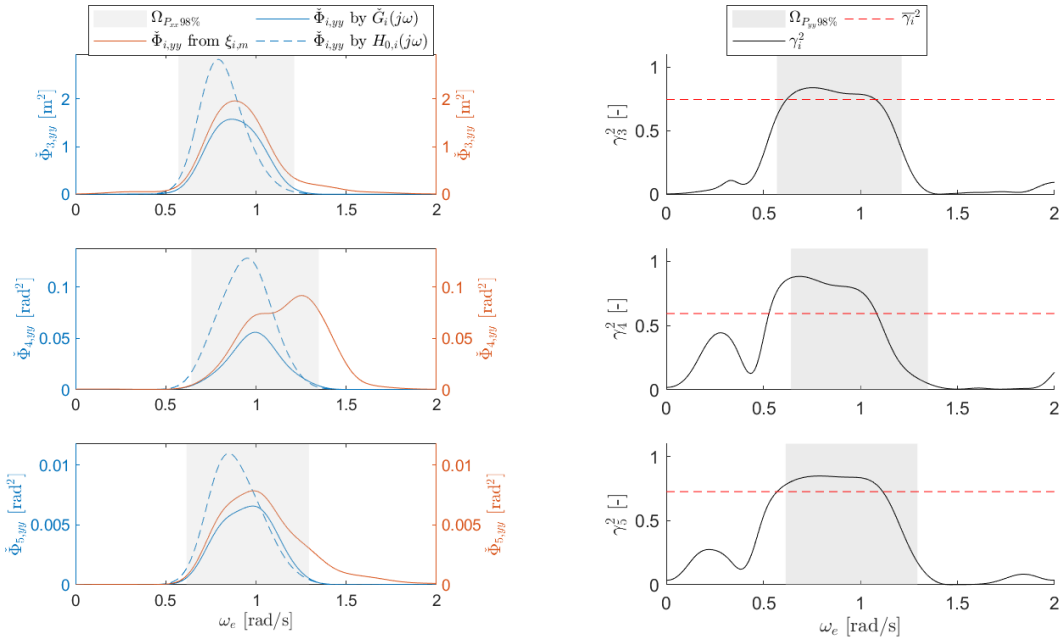
## Frequency-domain solutions



(a) Amplitudes of the transfer function

(b) Phase angles of the transfer function

Figure D.14: Run 5: The amplitudes and phase angles for of the pre-calculated TF's (solid red) and estimated TF's (solid blue). The blue dashed line represents the estimated TF plus or minus the estimated standard deviation. The grey area represents the domain which contains 98% of the energy of the motion response-spectra.  $\hat{G}_i(j\omega)$  has been estimated by  $\overline{CSM}_1$  with: a Hamming window, a window-length of  $\omega_l = 400$  [-], and an overlap of 75%.



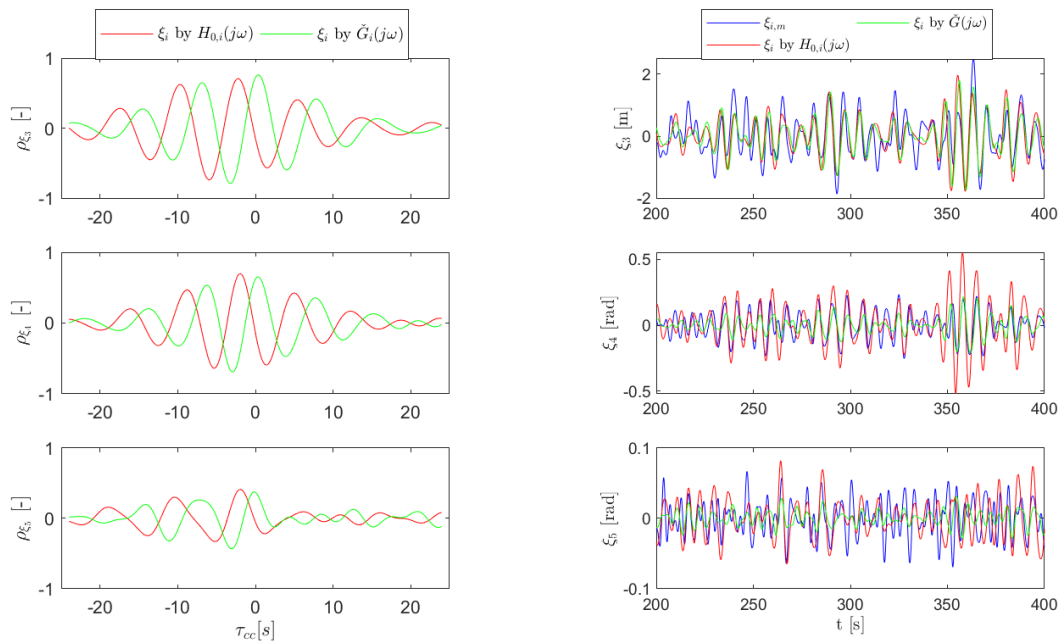
(a) Motion response-spectra

(b) Coherence function

Figure D.15: Run 5: The motion response-spectra (left) and the Coherence function (right). The blue dashed line in the left figure represents the motion response-spectra of the predicted motions obtained from pre-calculated TF's ( $H_{0,i}(j\omega)$ ). The solid blue line shows the motion response-spectra in the case that estimated TF's ( $\hat{G}_i(j\omega)$ ) are used. In the right figure, the red-dashed line is the mean coherence of the grey domain.  $\hat{G}_i(j\omega)$  has been estimated by  $\overline{CSM}_1$  with: a Hamming window, a window-length of  $\omega_l = 400$  [-], and an overlap of 75%.

## Run 6

## Time-domain solutions

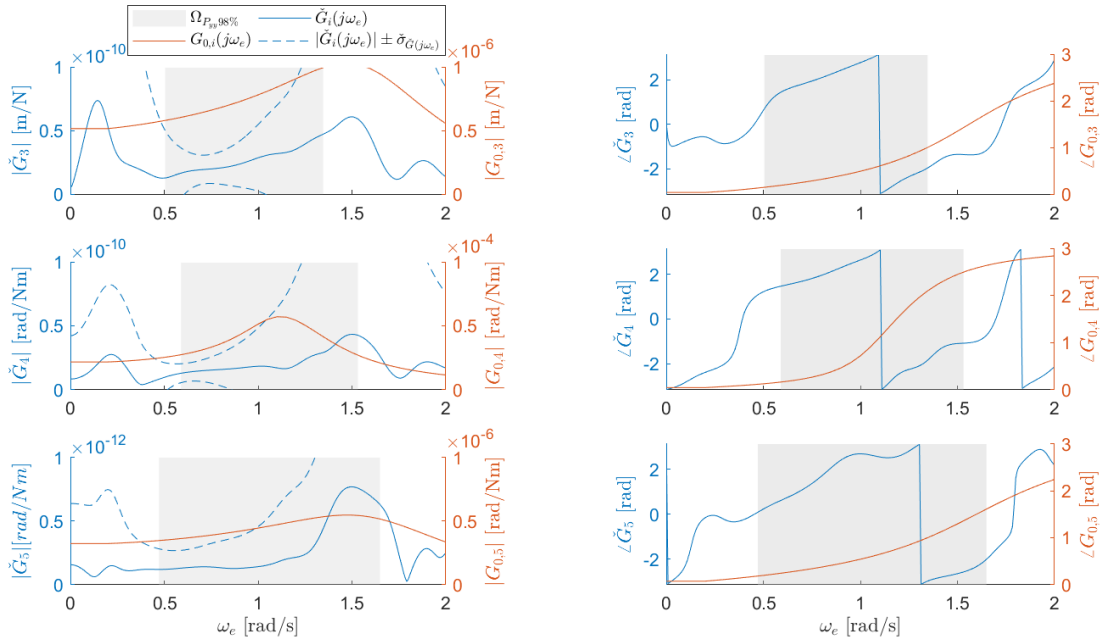


(a) Pierson correlation-coefficient

(b) Time domain solution

Figure D.16: Run 6: The left figure shows the cross-correlation coefficients between the measured- and predicted motions for. In the right figure the time-domain solutions of the measured motions are shown by the blue line. The green lines in both figures represents that the motions are predicted by using estimated TF's ( $\check{G}_i(j\omega)$ ) while the red lines show the solutions of the pre-calculated TF's ( $H_{0,i}(j\omega)$ ). Furthermore,  $\check{G}_i(j\omega)$  has been estimated by the  $\overline{CSM}_1$  with: a Hamming window, a window-length of  $w_l = 400$  [-], and an overlap of 75%.

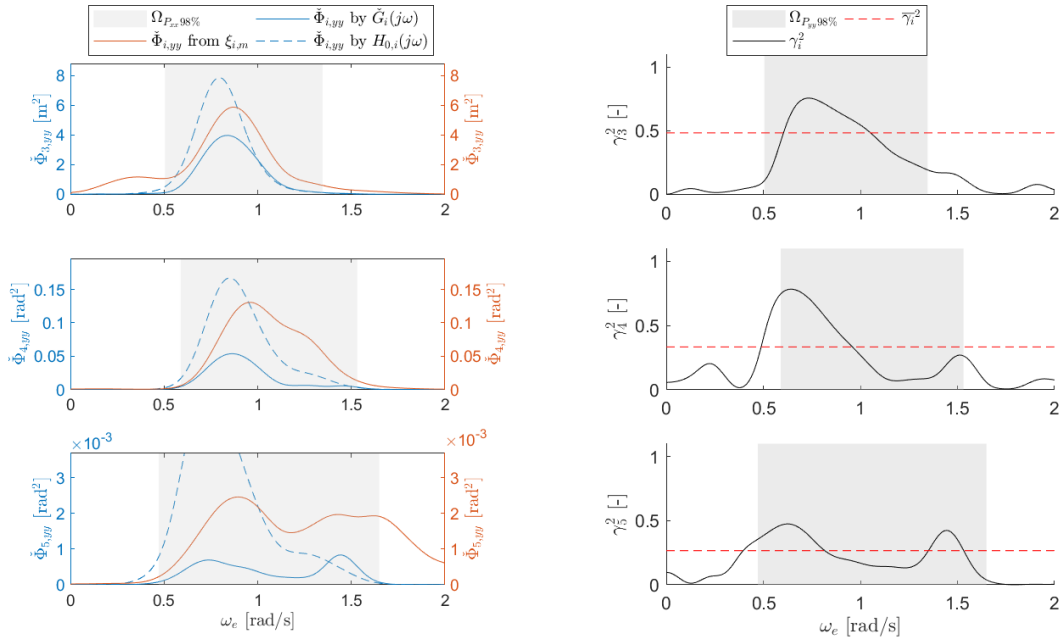
## Frequency-domain solutions



(a) Amplitudes of the transfer function

(b) Phase angles of the transfer function

Figure D.17: Run 6: The amplitudes and phase angles for of the pre-calculated TF's (solid red) and estimated TF's (solid blue). The blue dashed line represents the estimated TF plus or minus the estimated standard deviation. The grey area represents the domain which contains 98% of the energy of the motion response-spectra.  $\hat{G}_i(j\omega)$  has been estimated by  $\overline{CSM}_1$  with: a Hamming window, a window-length of  $w_l = 400$  [-], and an overlap of 75%.



(a) Motion response-spectra

(b) Coherence function

Figure D.18: Run 6: The motion response-spectra (left) and the Coherence function (right). The blue dashed line in the left figure represents the motion response-spectra of the predicted motions obtained from pre-calculated TF's ( $H_{0,i}(j\omega)$ ). The solid blue line shows the motion response-spectra in the case that estimated TF's  $\hat{G}_i(j\omega)$  are used. In the right figure, the red-dashed line is the mean coherence of the grey domain.  $\hat{G}_i(j\omega)$  has been estimated by  $\overline{CSM}_1$  with: a Hamming window, a window-length of  $w_l = 400$  [-], and an overlap of 75%.